

## ABSTRACT

### APPLICATION OF ELECTRORHEOLOGICAL FLUID FOR CONVEYING REALISTIC HAPTIC FEEDBACK IN TOUCH INTERFACES

by Alex James Mazursky

Realistic haptic feedback is necessary to provide meaningful touch information to users of numerous technologies, such as virtual reality, mobile devices and robotics. For a device to convey realistic haptic feedback, two touch sensations must be present: tactile feedback and kinesthetic feedback. Tactile feedback is felt at the surface of one's skin and displays textures and vibrations, whereas kinesthetic feedback is felt in one's joints and muscles and transmits position and movement information. While many devices today display tactile feedback through vibrations, most neglect to incorporate kinesthetic feedback due to size constraints. To provide comprehensive feedback, this study investigates a new haptic device based on an unconventional actuation method: electrorheological (ER) fluid, a smart fluid with tunable yield stress under the application of electric field. The device's control electronics and structural components are integrated into a compact printed circuit board, resulting in a slim device suitable for mobile applications. By controlling the ER fluid flow via applied electric fields, the device can generate a wide and distinct range of both tactile and kinesthetic sensations. These sensations were derived analytically from ER fluid's governing equations as well as experimentally. The device may be used as a haptic interface between a user and virtual environment.

APPLICATION OF ELECTRORHEOLOGICAL FLUID FOR CONVEYING  
REALISTIC HAPTIC FEEDBACK IN TOUCH INTERFACES

A Thesis

Submitted to the

Faculty of Miami University

in partial fulfillment of

the requirements for the degree of

Master of Science

by

Alex James Mazursky

Miami University

Oxford, Ohio

2019

Advisor: Dr. Jeong-Hoi Koo

Reader: Dr. Tae-Heon Yang

Reader: Dr. Michael Bailey Van Kuren

This Thesis titled

APPLICATION OF ELECTRORHEOLOGICAL FLUID FOR CONVEYING  
REALISTIC HAPTIC FEEDBACK IN TOUCH INTERFACES

by

Alex James Mazursky

has been approved for publication by

The College of Engineering and Computing

and

Department of Mechanical and Manufacturing Engineering

---

Dr. Jeong-Hoi Koo

---

Dr. Tae-Heon Yang

---

Dr. Michael Bailey Van Kuren

## Table of Contents

<b>List of Tables</b>	<b>v</b>
<b>List of Figures</b>	<b>vi</b>
<b>Dedication</b>	<b>ix</b>
<b>Acknowledgments</b>	<b>x</b>
<b>Declaration</b>	<b>xi</b>
<b>1 Introduction</b>	<b>1</b>
1.1 Motivation and Contributions . . . . .	1
1.2 Objectives . . . . .	4
1.3 Approach . . . . .	4
1.4 Study Outline . . . . .	5
<b>2 Background and Literature Review</b>	<b>6</b>
2.1 Haptic Perception . . . . .	6
2.2 Haptic Technology, Devices, and Applications . . . . .	8
2.3 Electrorheological Fluid: Behavior and Modeling . . . . .	13
2.4 Closing Remarks . . . . .	16
<b>3 Haptic Actuator based on ER Fluid in Flow Mode</b>	<b>17</b>
3.1 Proposed Actuator Design . . . . .	17
3.2 Analytical Modeling of ER Fluid Mechanics . . . . .	22
3.3 Analytical Modeling of Membrane Mechanics . . . . .	29
3.4 Numerical Evaluation of the Proposed Actuator . . . . .	31
3.5 Experimental Evaluation of the Fabricated Actuator . . . . .	34
3.6 Numerical vs. Experimental Performance . . . . .	39
3.7 Parametric Studies . . . . .	41
3.8 Conclusion and Discussion . . . . .	45
<b>4 Haptic Actuator based on ER Fluid in Mixed Mode</b>	<b>46</b>
4.1 Proposed Actuator Design . . . . .	46
4.2 Mathematical Modeling of ERF in Combined Squeeze and Flow Mode . . . . .	49

---

## TABLE OF CONTENTS

---

4.3 Model of Electrode Spring Displacement . . . . .	50
4.4 Numerical Evaluation of the Proposed Actuator . . . . .	52
4.5 Experimental Evaluation . . . . .	54
4.6 Numerical vs. Experimental Performance . . . . .	61
4.7 Performance Comparison: Squeeze-Flow vs. Pure Flow . . . . .	62
4.8 Parametric Study . . . . .	65
4.9 Conclusions and Discussion . . . . .	66
<b>5 Combined Sensor and ER Fluid-based Actuator</b>	<b>68</b>
5.1 Proposed Sensor Designs . . . . .	68
5.2 Control and Applications . . . . .	75
5.3 Conceptual Designs . . . . .	79
5.4 Conclusion and Discussion . . . . .	82
<b>6 Conclusions and Future Work</b>	<b>83</b>
6.1 Summary . . . . .	83
6.2 Contributions . . . . .	84
6.3 Future Outlooks . . . . .	85
<b>References</b>	<b>86</b>

## **List of Tables**

3.1	Material properties of GER fluid at 25°C. . . . .	21
3.2	Parameters of the proposed haptic actuator. . . . .	31
3.3	Parameters of the membrane model. . . . .	32
4.1	Mechanical properties of Type 304 Stainless Steel (SUS 304) used in the FEM simulation. . . . .	51
4.2	Parameters of the squeeze-flow simulation. . . . .	53

## List of Figures

1.1	Commercial electronic devices that make use of vibrotactile feedback. . . . .	1
1.2	Visualizing trends in mobile technology: Over time, mechanical buttons have been replaced by smooth touch screens. . . . .	3
2.1	Receptors in the glabrous skin. . . . .	7
2.2	<i>TouchEngine</i> : Bending motor, piezoelectric layers and haptic display. . . . .	9
2.3	External appearance of <i>MimicTile</i> . . . . .	10
2.4	<i>Mudpad</i> operating as a tactile memory game. . . . .	11
2.5	Haptic actuator based on MR fluids and its components. . . . .	12
2.6	ER fluid suspended in an electric field between electrodes. . . . .	13
2.7	Operational modes for ER fluids . . . . .	14
2.8	Images of nanoparticles in GER suspensions. . . . .	14
3.1	Working principle of the proposed flow mode haptic actuator . . . . .	18
3.2	Exploded view drawing of the preliminary, 3D printed flow mode haptic actuator. .	19
3.3	Exploded view drawing of the proposed PCB flow mode haptic actuator. . . . .	20
3.4	Construction and assembly of the prototype PCB-based flow mode actuator. . . .	21
3.5	Velocity profile of ER fluid in the activation region associated with a fixed electrode configuration. . . . .	23
3.6	Control volume element for a fixed electrode form. . . . .	25
3.7	Schematic diagram of the dimensions used in the membrane load-deflection analysis.	29
3.8	Yield stress plotted as a function of applied electric field for the purchased GER fluid. . . . .	32
3.9	Simulation results for the force produced by indenting the superposed membrane in the (a) contact and (b) reciprocating regions. . . . .	33
3.10	Approximation of volumetric flow due to indentation. . . . .	33
3.11	Results of the simulated flow mode actuator: force (N) vs. depth (mm) along its stroke. . . . .	34
3.12	Experimental setup to measure the force generated by the prototype actuator with respect to indentation depth for applied voltage signals. . . . .	35
3.13	Comparison between the membrane's experimental performance from dry testing and the analytical response for the (a) contact membrane and (b) reciprocating membrane. . . . .	36
3.14	Experimental kinesthetic results: force (N) vs. depth (mm). . . . .	37

## LIST OF FIGURES

---

3.15 Experimental kinesthetic results: force rate (%) vs. indentation depth (mm) . . . . .	38
3.16 Experimental tactile results: force rate vs. indentation depth (mm) . . . . .	39
3.17 Comparison of kinesthetic feedback between the measured and simulated forces . .	40
3.18 Comparison of vibrotactile feedback strictly due to the ER effect at 3 Hz excitation between the measured force and simulated force. . . . .	40
3.19 Effect of flow mode electrode gap size $d$ on actuator response. . . . .	42
3.20 Effect of outer flow mode electrode radius $r_0$ on actuator response. . . . .	44
4.1 Working principle of the proposed squeeze-flow haptic actuator . . . . .	47
4.2 Exploded view drawing of the squeeze-flow haptic actuator. . . . .	48
4.3 Fabricated components and mixed mode actuator assembly. . . . .	48
4.4 Fabricated deformable spring electrode. . . . .	49
4.5 Conventional squeeze mode model schematic. . . . .	50
4.6 Steps in the finite element analysis process for characterizing the electrode spring. .	51
4.7 FEM results for the force produced by displacing the spring electrode. . . . .	52
4.8 Results of the simulated mixed mode actuator: force (N) vs. depth (mm) along its stroke. . . . .	53
4.9 Experimental setup for evaluating the mixed mode device's kinesthetic and vibro- tactile feedback. . . . .	55
4.10 Comparison between the electrode spring's experimental response from dry testing and the FEM simulation response for the superposed 0.2 mm and 0.3 mm spring responses. . . . .	55
4.11 Experimental mixed mode kinesthetic results: force (N) vs. depth (mm). . . . .	56
4.12 Experimental mixed mode kinesthetic results: force rate (%) vs. indentation depth (mm). . . . .	57
4.13 Experimental tactile results: force rate vs. indentation depth (mm). . . . .	58
4.14 Acceleration (g) vs. Time (s) for 50 Hz square wave input. . . . .	59
4.15 Measured acceleration signals and FFT spectrum under 50 Hz square wave input. .	60
4.16 Measured acceleration signals and FFT spectrum under 100 Hz square wave input.	60
4.17 Measured acceleration signals and FFT spectrum under 200 Hz square wave input.	60
4.18 Measured acceleration signals and FFT spectrum under 300 Hz square wave input.	60
4.19 Comparison of kinesthetic feedback between the measured and simulated force for mixed mode. . . . .	61
4.20 Comparison of vibrotactile feedback between the measured and simulated force for mixed mode. . . . .	62

## LIST OF FIGURES

---

4.21 Comparison of the off-state response for the squeeze flow and pure flow mode actuator. . . . .	63
4.22 Comparison of kinesthetic feedback among squeeze-flow and pure flow actuators under applied voltages. . . . .	64
4.23 Comparison of vibrotactile feedback among squeeze-flow and pure flow actuators under applied voltages. . . . .	65
4.24 Effect of spring electrode radius $R$ on actuator response. . . . .	66
5.1 Fabricated triple point pressure sensor. . . . .	69
5.2 Resistance-Force coupling curve for pressure-sensitive resistive material. . . . .	69
5.3 Off-state plot for the actuator and TPP sensor response under indentation. . . . .	70
5.4 Force profiles with the TPP sensor installed. . . . .	71
5.5 Fabricated single point pressure sensor. . . . .	72
5.6 Off-state plot for the actuator and SPP sensor response under indentation. . . . .	72
5.7 Assembled actuator with embedded bending sensor. . . . .	73
5.8 Off-state plot for the actuator and sensor response under indentation. . . . .	74
5.9 Actuator and bending sensor response under 4 kV 100 Hz square waves. . . . .	74
5.10 Actuator and bending sensor response under 4 kV 3 Hz sine waves. . . . .	75
5.11 Proposed flow of haptic interaction between user and computer. . . . .	76
5.12 Proposed block diagram for haptic control. . . . .	77
5.13 Fabricated circuit for controlling high voltage at compact scale. . . . .	77
5.14 Function Generator App: Controls the frequency of 5 kV square waves in real-time. . . . .	78
5.15 Frequency Mapping App: Plots displacement in real-time and maps the supplied frequency to the displacement. . . . .	79

## **Dedication**

*Dedicated to my family.*

## Acknowledgments

First and foremost, I would like to thank my advisor and mentor, Dr. Jeong-Hoi Koo, for his patience and guidance. From my five years at Miami, I feel that Dr. Koo taught me most of what I know about research, problem solving, discipline and dedication. I am incredibly grateful that I was able to work with him early in my academic career; I will take the lessons and advice he gave me and continue to apply them in both my professional and personal life. Thank you for exposing me to such captivating problems and always looking out for opportunities for your students.

I would like to thank Dr. Tae-Heon Yang. I owe much to both Dr. Yang's practical design talents and analytical modeling intuition. While during my defense we are, in your words, "enemies," I am very grateful to be *friends* at all other times.

I would like to thank Dr. Bailey Van Kuren, whose HRI class and creative outlook inspired both the applications of this research and my future career plans.

A very special thank you to my dear friend, colleague and housemate, Paul Goetze. Paul's manufacturing expertise catapulted this project's prototyping to new heights that would otherwise have been a struggle. I'm grateful to have worked together for the past five years on research, coursework, side projects, bouncing ideas off each other, exploring the countryside by bike, the list goes on...

Among Dr. Koo's lab, I must thank Adam Coon and Sae-Hyun Sone. Working—and exploring—together in Korea for the entire summer has been the highlight of my college years.

Along a similar vein, I must thank Dr. Jae-Hung Han for inviting us to his lab at KAIST last summer, where much of the results presented in this thesis originated. Thank you to Dr. Sam-Yong Woo for his help with sensor design. Thank you to Mr. Yang for his assistance with circuit design.

Thank you to everyone with whom I've had the pleasure of sharing a graduate office space. Cramming research, courses, grading responsibilities and PhD/job searching into two brief years (or a 4+1) makes the Master's degree a particularly brutal endeavor and I am grateful to have been able to spend this time within such a supportive community. Thank you to Miami MME for providing such a space.

Furthermore, this research could not have been completed without the generous financial support of the Ohio Space Grant Consortium, which granted the freedom to pursue exciting research directions.

My thanks goes out to my family for their continued support throughout my education. I am incredibly privileged to have had you looking out for me, especially when I blew a tire on I-65 three hours from home and three hours from school not long before this document was due.

Finally, my deepest thanks to my loving and supportive girlfriend, Natalie Marie Funes, who provides unending inspiration.

## **Declaration**

This thesis is the result of my own work and collaborations in which I was always the scientific lead. This dissertation has not been previously submitted, in part or whole, to any university or institution for any degree, diploma, or other qualification. The ideas herein have appeared in the following published papers as of May 2019:

1. Design, Modeling, and Test of a Thin Haptic Actuator based on Electrorheological Fluids. Alex J. Mazursky, Jeong-Hoi Koo, Tae-Heon Yang, *Journal of Intelligent Material Systems and Structures*, Special Issue: Selected papers from ICAST 2018 (2019).
2. Application of Electro-Rheological Fluids for Conveying Realistic Haptic Feedback. Alex J. Mazursky, Jeong-Hoi Koo, Tae-Heon Yang, *Proc. ICAST 2018* (2018).
3. Experimental Evaluation of a Miniature Haptic Actuator based on Electrorheological Fluids. Alex J. Mazursky, Jeong-Hoi Koo, Tae-Heon Yang, *Proc. SPIE Smart Structures and Nondestructive Evaluation* (2018).

# 1 | Introduction

This chapter discusses the motivation and significance of this study. The need and importance of realistic haptic feedback is emphasized. The study's primary objectives are presented along with the proposed approach necessary to achieve these overarching goals.

## 1.1 Motivation and Contributions

In recent years, mobile devices have experienced a shift from mechanical buttons to smooth, touch screen surfaces. However, the benefit of larger and more versatile screens comes at a cost to the physical feedback associated with indenting buttons. The information conveyed to the user through these touch sensations is referred to as haptic feedback. Humans perceive touch through two primary sensations: (1) tactile feedback and (2) kinesthetic feedback. Kinesthetic feedback provides information about position and movement of joints and muscles. Tactile feedback consists of the sensations felt at the surface of one's skin and just underneath it. When examining an object, humans may rub it to feel its texture and roughness (tactile sensation) and press it to feel its resistance and elasticity (kinesthetic sensation). Therefore, both sensations must be present to completely observe an object through touch [1].

While tactile feedback is quite common in devices today due to the ease of miniaturization of tactile actuators, such as smart phones and gaming controllers capable of producing vibration (see Figure 1.1), the inclusion of kinesthetic feedback has lagged behind. While tactile feedback is suitable for conveying textures, it is not sufficient to produce comprehensive haptic sensations for other applications, such as those dominated by kinesthetic feedback (i.e. button clicking or pushing on compliant surfaces). Therefore, an entire aspect of touch feedback is absent in modern devices.



(a) Nintendo's "N64 Rumble Pak."



(b) A smart phone producing vibration signals.

**Figure 1.1.** Commercial electronic devices that make use of vibrotactile feedback.

Hence, the motivation for this study is based upon the need for *both* tactile and kinesthetic feedback in mobile devices. Current small touchscreen devices often incorporate vibrotactile feedback through voice coils, eccentric rotating mass vibration motors (ERMs) or linear resonant actuators (LRAs). However, current methods for producing kinesthetic feedback are insufficient for mobile applications due to size, power and stability constraints [2, 3]. Therefore, this work aims to develop a new type of actuator for conveying *both* tactile and kinesthetic feedback and miniaturize it into a compact and standalone design. The inclusion of kinesthetic feedback in mobile devices, in addition to vibrotactile, audio, and visual feedback, will enhance user experience and sense of immersion.

Many efforts have been made to develop small-scale kinesthetic actuators, such as those based on alternating current/direct current (AC/DC) motors [4–6]. These face a number of challenges regarding power consumption, size and stability, as further detailed in Chapter 2. This study takes a unique approach to the problem by applying a smart fluid to actuate the kinesthetic and vibrotactile sensations. Smart materials are materials with variable properties dependent upon external stimuli. In particular, this study investigates the use of electrorheological (ER) fluid, a smart fluid with a viscosity dependent upon an applied electric field, to convey haptic feedback. The proposed actuator's design uses ER fluid's controllable yield stress to translate electrical signals into mechanical signals; this mechanism is responsible for providing a range of kinesthetic feedbacks. Additionally, because of ER fluid's simple electrical control, the actuator's thickness may be reduced for mobile applications.

The contributions of this study are rooted in its novel basis of actuation. The dynamic viscosity of ER fluid can produce large forces at high rates of actuation, allowing for a wide range of distinct kinesthetic and tactile sensations. These sensations may be studied using mechanical analysis or through human subject testing. By introducing sensing in addition to actuation, control of the device can be implemented and used toward data-driven haptic rendering of compliant materials. The working principle of the design unit can also be scaled into a haptic array with localized sensations. Furthermore, the proposed design is slimmer than traditional haptic actuators and others based on smart materials, making it an ideal candidate for mobile applications.

A wide range of applications for this technology can be recognized. Current trends show a shift in how we interact with our devices. Represented in Figure 1.2, the development of touch screens as input/output (I/O) devices has led to replacement of traditional methods, such as button inputs [7]. As devices continue to transition from being controlled by physical buttons and knobs to smooth touch screens, a significant degree of touch feedback is lost despite added display versatility. By restoring haptic feedback to touch applications, the usability, interactivity, and realism of the device is greatly enhanced. In addition to visual and auditory sensations, being able to touch, feel and manipulate objects in an environment, whether real or virtual, offers the user a

greater sense of immersion [1]. Therefore, haptic feedback is desired for numerous applications including simulators, teleoperation, entertainment and more [8–10]. To emulate and restore physical feedback in electronics, haptic technologies are being investigated and applied to bridge the gap between the user and the virtual world.

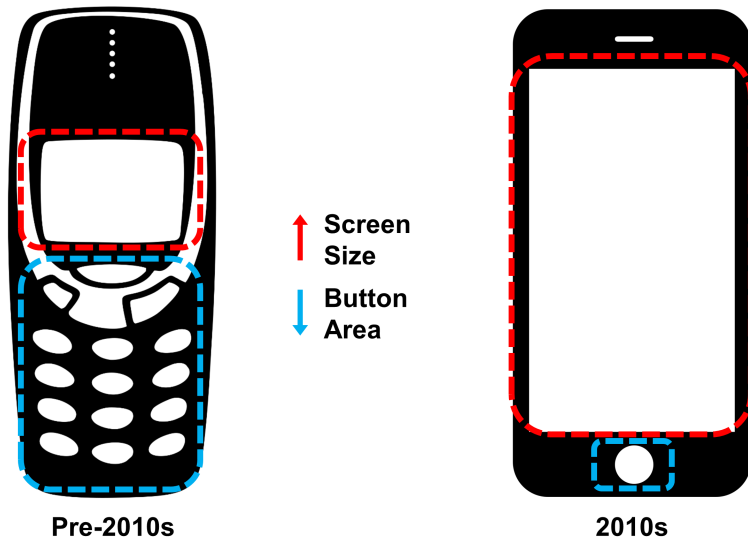


**Figure 1.2.** Visualizing trends in mobile technology: Over time, mechanical buttons have been replaced by smooth touch screens.

In addition to the experimental approaches outlined, a mathematical model of the actuator's behavior is of great contribution to this study. To best understand the influences of design and control parameters on the actuator's behavior, an analytical model was developed based on ER fluid's electro-responsive viscosity. This model is dependent upon the actuator's geometry, fluid properties, electrical excitation, and rate of interaction. Parametric studies are performed using the model to predict actuator behavior and contribute to future design iterations.

Traditional kinesthetic actuators cannot be integrated into mobile systems in their present form. The proposed ER fluid-based miniature actuator addresses the current constraints of size, power and stability. This study intends to design a stand-alone, miniature haptic actuator and accompanying control system. The significance of this study is presented below:

- The proposed actuator can produce both tactile and kinesthetic sensations at mobile scale.
- Closing the actuation loop by including real-time sensing and control allows for haptic rendering of compliant materials.
- The analytical model can be used to identify key design parameters for future generations of ER fluid-based haptic actuators.

## 1.2 Objectives

The overarching goal of this project is to design and test a miniature haptic device based on ER fluids that can convey both vibrotactile and kinesthetic sensations. To achieve this goal, the research specifically aims to address:

- **Prototype development and testing:** Design and fabricate initial prototypes to demonstrate the feasibility of using ER fluid to produce haptic feedback in a small package.
- **Mathematical modeling and simulation:** Derive an analytical solution specific to the actuator's behavior from previous models of ER fluid flow. Compare the model's response to the experimental results and tune the model accordingly. Use the accurate model as a basis for predicting the behavior of future designs.
- **Control and application development:** Embed the design with sensing capabilities and develop control of the system. Demonstrate the ability of the device to act as a haptic interface between the real world and virtual conditions.

## 1.3 Approach

To accomplish the goals listed above, the following process must be followed:

### 1.3.1 Fabrication of Haptic Actuator

To reduce the size of the actuator design from previous work [11], the electrical and structural components are integrated into printed circuit boards (PCB), rather than 3D printing the structure and machining the electrodes from metal stock. The PCB method results in a simpler, modular assembly and a thinner, more mobile device. While previous design iterations have used a large, immobile voltage amplifier, the proposed design reduces this into a compact circuit integrated directly into the device for better portability. The actuator's volume is filled with giant (wide yield bandwidth) ER fluid and a thin, polydimethylsiloxane (PDMS) sheet is compressed against the upper surface of the device. The elastic sheet therefore doubles as a seal and the actuator's contact surface.

### 1.3.2 Evaluation of Haptic Performance

To measure the performance of the prototypical device, a dynamic mechanical analyzer (DMA) is used. The DMA measures the total resistive force with respect to indentation depth over the

actuator's stroke. The actuator's effectiveness is tested under a range of input voltage and frequency conditions. This analysis yields insight into the device's ability to provide both vibrotactile and kinesthetic feedback. Additionally, experimental evaluation acts as a reference when evaluating the results of the modeled behavior.

### 1.3.3 Model Design

To understand the actuator's performance from a mathematical perspective, a model is developed based on the actuator's fundamental behavior. First, an analytical solution to the resistive force produced by the actuator over its stroke as a function of applied electric field is derived from the Navier-Stokes equation and the coupling between the applied electric field and the fluid's yield stress. A numerical approach is taken to simulate the actuator's resistive force output and is compared to the experimental results. Parametric analysis is performed to determine the influence of actuator geometry on haptic performance and recommendations are made toward future design iterations.

### 1.3.4 Application for Realistic Sensations

To provide real-time control of the actuator module, a sensor is designed around the pressure-sensitive resistance of a new thin film developed at Korea Research Institute of Standards and Science (KRISS). A sensing PCB is incorporated into the existing actuator design. To demonstrate the functionality of the combined actuator-sensor module, basic computer applications were developed to act as a virtual environment. The virtual environment communicates sensations to the actuator through a microcontroller as a function of voltage and frequency. Therefore, the actuator can act as a bridge between the real and virtual world by conveying real-time touch feedback.

## 1.4 Study Outline

This paper is organized into a series of chapters, each detailing the specific steps taken toward the overarching goals. The chapters are listed below and begin immediately following this section.

**Chapter 2:** Background and Literature Review

**Chapter 3:** Haptic Actuator based on ER Fluid in Flow Mode

**Chapter 4:** Haptic Actuator based on ER Fluid in Mixed Mode

**Chapter 5:** Combined Sensor and ER Fluid-based Actuator

**Chapter 6:** Conclusions and Future Work

# 2 | Background and Literature Review

This chapter presents an overview of human haptic perception, the current state of haptic technology, the application of smart materials to haptics, and smart fluid modeling. The mechanisms through which humans perceive touch is outlined. Published studies detailing the importance of haptic feedback and relevant technologies are investigated and summarized. Specific case studies of smart material approaches to convey haptic feedback are then examined. Finally, a review of the governing equations behind modeling ER fluid's behavior is performed to form the basis of this study's design principles.

## 2.1 Haptic Perception

Haptics, stemming from the Greek word *haptikos*, means “pertaining to the sense of touch.” In contrast to the other four human senses (sight, hearing, smell, and taste), the sense of touch is not a localized phenomenon within the body. Rather, it is spread throughout the skin, joints, muscles, and tendons. Two components may be used to define haptic feedback: (1) kinesthetic feedback and (2) tactile feedback [12]. Kinesthetic (force) feedback provides information about position and movement through forces and torques perceived by the muscles, tendons, and joints. Tactile (cutaneous) sensations provide information pertaining to surface roughness and vibration sensed by mechanoreceptors in the skin. Mechanoreceptors in the skin are sensitive to pressure, distortion, and vibration and can be categorized by receptance to different stimuli [13].

### 2.1.1 Tactile Sensing

Tactile perception is a component of the human somatosensory system. Mechanoreceptors, shown in Figure 2.1, can be differentiated by their morphology, perceived sensation, size of their receptive fields, and rate of adaptation. Rapid Adapting (RA) mechanoreceptors perceive transient sensations, whereas Slow-Adapting (SA) mechanoreceptors tend to perceive static sensations. The four mechanoreceptors in the skin are presented below:

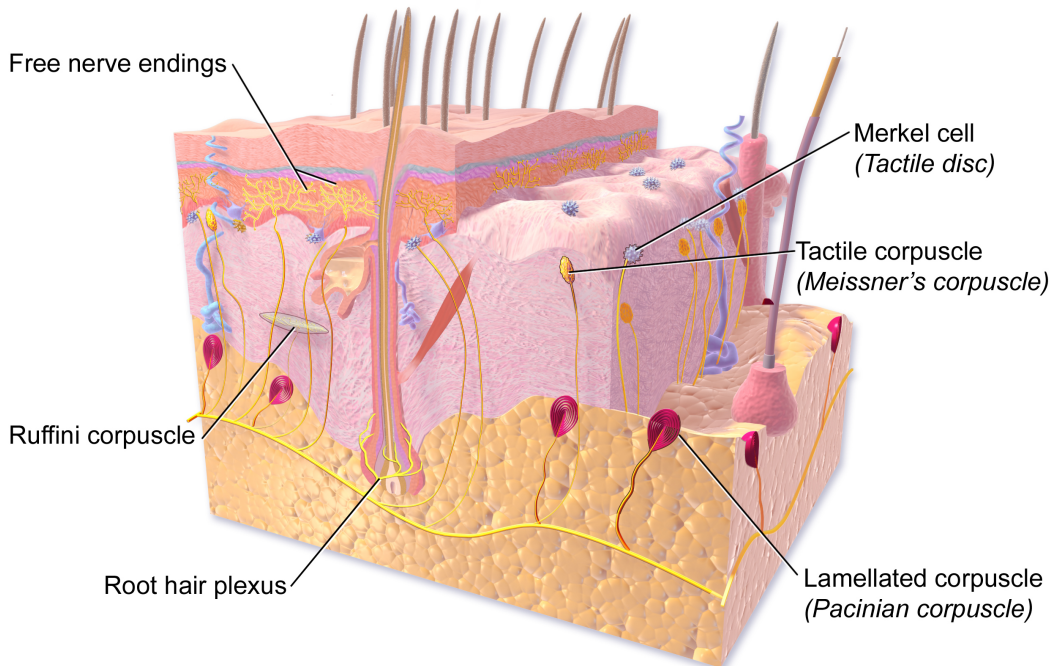


**Figure 2.1.** Receptors in the glaborous skin [14].

1. **Meissner corpuscles (RA1):** Respond to low-frequency vibrations (10-200 Hz) and sense skin deformation (stroking, fluttering) [15, 16].
2. **Pacinian corpuscles (RA2):** Respond to higher-frequency vibrations (40-800 Hz, though most sensitive at 200-300 Hz) and provide information on transient contacts [15, 17].
3. **Merkel disks (SA1):** Respond to low frequency vibrations (<~5 Hz) and perceives texture and pressure [15–17].
4. **Ruffini endings (SA2):** Sensitive to static forces and perceives skin stretching [16].

To produce realistic haptic systems, researchers must understand the mechanisms, and their associated limits, through which humans perceive tactile feedback [18]. Though cutaneous mechanoreceptors are distributed throughout the body's skin, their density is greater in the glabrous (hairless) skin of the hands and feet than in hairy skin [19]. This correlates to greater sensitivity to touch in these regions and has led to most tactile devices interfacing with the hands. Additional limitations of note include the large receptive field size and lack of directional sensitivity of Pacinian corpuscles [17]. Thus, humans have difficulty perceiving the direction and source of individual signals in a field [20].

### 2.1.2 Kinesthetic Sensing

Kinesthetic feedback is characterized by force and displacement perceived by receptors in the muscles, tendons, and joints. Specific receptors of kinesthetic sensations are muscle spindles and Golgi tendon organs. Muscle spindles detect muscle stretch (strain sensing), while Golgi tendon organs sense changes in muscle tension (stress sensing) [21, 22].

A metric for evaluating kinesthetic sensations is the Just-Noticeable-Difference (JND). The JND is a measure of the amount that a kinesthetic force must change for a difference to be distinguished by a human and is commonly employed in psychophysical studies. In the context of kinesthetic analysis, force rates are used to define the thresholds for which humans can consistently detect changes in force. For forces between 0.5 and 200 N, the threshold is found to be about 7-10% [23]. Hence, for a device to be effective at producing distinct kinesthetic sensations, it must be capable of producing force rates greater than the JND threshold values.

## 2.2 Haptic Technology, Devices, and Applications

In recent years, the rising implementation of haptic technology has transformed how we interact with electronic devices and digital information. Haptic technology conveys information to the user through touch sensations, offering a more engaging and realistic user experience. Haptic devices may be divided into three primary categories: (1) graspable, (2) wearable, and (3) touchable. With mobile computing systems in mind, this section of the review focuses on the history and current state of touchable systems, such as handhelds, surfaces, and buttons. Comments on the state of commercial haptic systems are provided, followed by a review of recent research on haptic devices.

### 2.2.1 Haptic Feedback in Consumer Products

In consumer products today, haptic feedback is commonly attributed to tactile feedback produced via vibration, referred to as vibrotactile feedback. Vibration has been popularized in cellphones as a silent notification method. In gaming, it is often used to simulate the roughness of driving offroad or the recoil of a rifle. Additionally, previous studies have shown that enhancing user immersion through vibrotactile feedback results in improved user performance of typical tasks on devices, such as clicking and scrolling [24, 25]. The prevalence of vibrotactile feedback in modern commercial devices can be attributed to the nature of vibrational actuators. Commercial vibrotactile actuators are small, light weight, and inexpensive, making purely tactile systems easy to implement at small scales and appealing for their added information at little cost.

Though many commercial devices today incorporate vibrotactile feedback, most neglect to integrate kinesthetic feedback due to size constraints. Many of the kinesthetic devices proposed

in current research are based upon alternating current/direct current (AC/DC) motors to create force feedback sensations [4–6,26]. Despite developments toward AC/DC motor-based kinesthetic actuators, they cannot be easily implemented into small-scale devices, such as mobile handhelds, due to their size and power requirements. Additionally, active-controlled motors tend to have instability problems, which can be a significant roadblock for certain applications [2,3].

### 2.2.2 Haptic Device Research

In mobile devices, proposed haptic systems generally either apply feedback directly at the touch screen or through actuators attached to the side or back of the device. An early approach to introducing haptic feedback in smooth touch screens was presented in *Active Click* [27]. A small voice coil was fixed to the back of the screen and could produce small displacements when excited at its natural frequency. Hence, a clicking sensation could be observed when a single pulse was produced by the actuator. These design principles were adapted shortly after by *TouchEngine*, shown in Figure 2.2, which instead used a piezoelectric actuator, resulting in more robust vibrotactile capabilities in a slimmer package [25,28]. *TouchEngine* was utilized again in *PreSenseII*, which introduced a pressure sensor based on a force-sensitive polymer film contact surface [29]. With the addition of pressure sensing, “soft” and “hard” button pressing sensations were proposed.

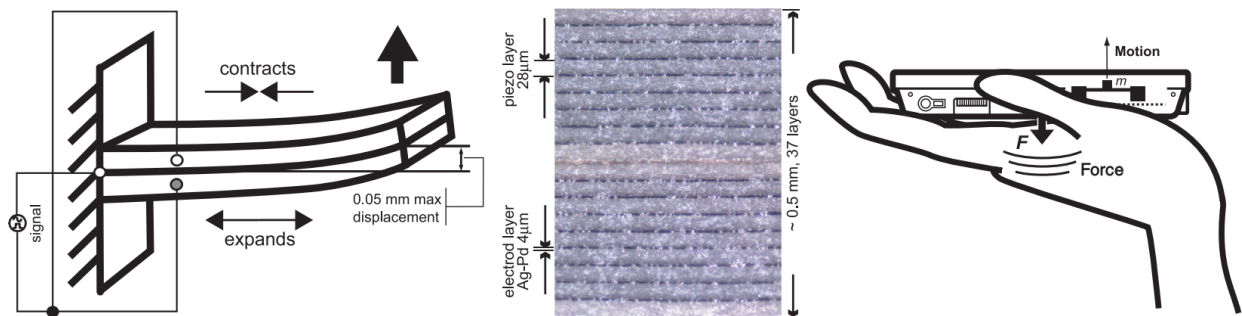


**Figure 2.2.** *TouchEngine*: Bending motor, piezoelectric layers and haptic display [25].

Novel kinesthetic actuation mechanisms have been proposed for mobile devices, as well. *SqueezeBlock* implemented a “spring” (based on a motor linearized via rack and pinion) that changes stiffness based on virtual conditions [26]. Users interacted with the device by squeezing it, similar to a stress ball or grip trainers, and the magnitude of stiffness contained information. For instance, little resistance to squeezing could indicate a low battery level. A similar approach was used in *MimicTile*, shown in Figure 2.3; however, the variable stiffness was based upon shape memory alloy (SMA) wire in a pulley system [30]. A major benefit of the approaches taken in *SqueezeBlock* and *MimicTile* is that both the input and output may be coupled into a single gesture, where the input is the displacement and the output is the kinesthetic feedback associated with the stiffness.

This coupled input and output was incorporated into the current study, as well.



**Figure 2.3.** External appearance of *MimicTile* [30].

To avoid the problems associated with traditional kinesthetic actuators based on AC/DC motors, researchers have proposed using ‘smart materials’ to actuate kinesthetic sensations. Smart materials are designed to have variable properties dependent upon external stimuli, such as temperature, stress, magnetic or electric fields and more. Thus, smart materials may pose a mechanically simpler solution to traditional actuation. For instance, the piezoelectric and SMA wire actuators upon which *TouchEngine* and *MimicTile* were respectively based are classified as smart materials, where piezoelectrics respond to electrical inputs through strain outputs and SMAs respond to thermal inputs with strain outputs [25, 28–30]. However, neither *Touch Engine* nor *MimicTile* are capable of providing *both* tactile and kinesthetic feedback; therefore, they lack comprehensive haptic feedback. This may be attributed to the low force and displacement produced by the piezoelectric actuator (insufficient for kinesthetic feedback) and the slow response of the SMA actuator (<5 Hz, insufficient for vibrotactile feedback). To produce comprehensive haptic feedback, a device must be capable of providing distinguishable forces and displacements, as well as tactile feedback. Under these constraints, a more suitable actuation basis must be realized; a promising step toward this goal may be through the use of smart fluids.

### 2.2.3 Rheology-based Haptic Feedback

In the following subsections, two smart fluids, magneto-rheological (MR) fluid and electro-rheological (ER) fluid, are discussed in the context of haptic feedback. A review of rheology-based haptic feedback is presented and the two modes are compared. A more comprehensive examination of smart fluid mechanics and modeling is presented in the following section, Section 2.3.2.

## **Magnetorheological Fluid-based Haptic Feedback**

Magnetorheological (MR) fluid is a smart fluid; when subjected to a magnetic field, its apparent viscosity increases in proportion. Through this reversible mechanism, the fluid's yield stress may be accurately controlled. Moreover, the fluid responds to changes in the magnetic field within a few milliseconds, allowing for high frequency control. Through MR fluid's tunable yield stress and temporal resolution, researchers have investigated its application in producing kinesthetic and tactile sensations.

An early instance of applying MR fluid as a means of liquid haptics was presented in White's 1998 thesis at MIT [31]. In this work, a bladder of MR fluid was mounted atop an  $8 \times 8$  array of electromagnets. Each electromagnet was capable of controlling the local magnetic field, and therefore the local viscosity of the fluid. This design was capable of producing regions of hardness and softness, as well as emulating textures through cyclic hardening and softening. Jansen et al. improved upon this design in a similar MR fluid array based design, deemed *MudPad* and shown in Figure 2.4, by implementing pressure sensing in addition to actuation [32–34]. The combined sensing and actuation allowed *MudPad* to act as a virtual keyboard, graph visualization tool, and source of eyes-free information on processes running in the background. A similar design was used by Han to provide surgeons with tactile information about biological tissues and organs [35].

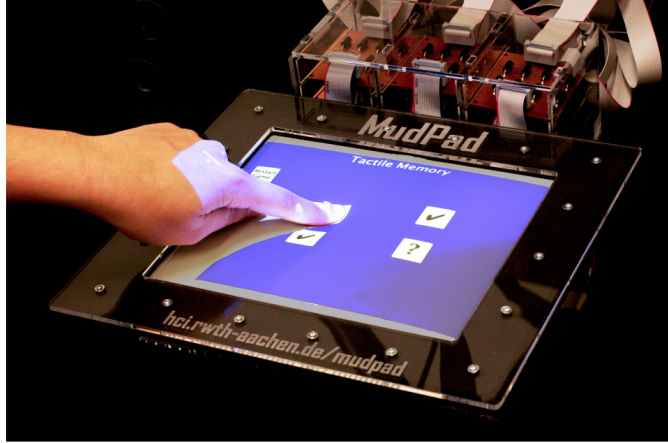


**Figure 2.4.** *MudPad* operating as a tactile memory game [33].

However, reducing the size of MR fluid-based actuators proves difficult due to the size required of electromagnet coils. To investigate the feasibility of miniaturizing MR fluid-based haptic devices, Yang et al. proposed a tunable stiffness display based on a single coil [36]. In subsequent parametric modeling studies, this design was reduced into a miniature button, shown in Figure 2.5, capable of producing a wide range of kinesthetic and vibrotactile feedback [37]. However, basing an actuator around MR fluid requires precise manufacturing and assembly to miniaturize the complex circuitry due to the solenoid coil.

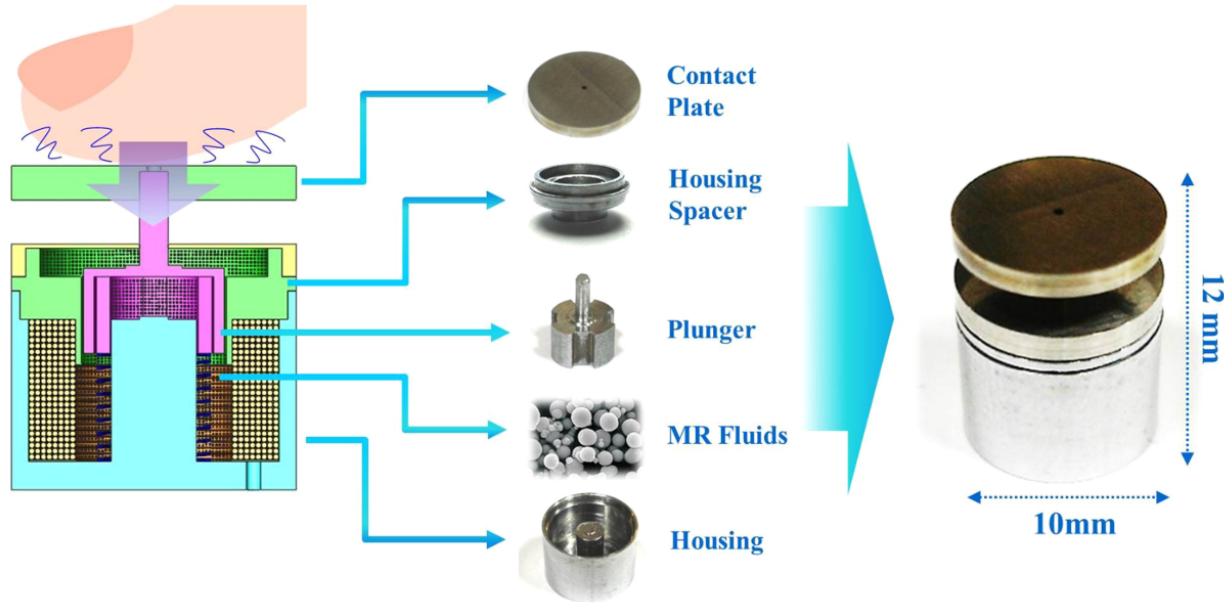


**Figure 2.5.** Haptic actuator based on MR fluids and its components [37].

### **Electrorheological Fluid-based Haptic Feedback**

Electrorheological (ER) fluid, MR fluid's counterpart with a viscosity dependent upon electric field, presents opportunity to address the complications observed when implementing MR fluid in miniature applications [38]. Similar to MR fluid, ER fluid features response times in the order of milliseconds, low power consumption and few issues with stability [39–41]. However, compared to MR fluid, the electrical design for controlling ER fluid is simpler; only two electrodes spaced approximately 1 mm apart are needed, thinner than the equivalent solenoid coil for MR devices. With a goal of actuator mobility, a basis of ER fluid allows for smaller and more portable designs.

While ER fluid has often been applied to exclusively tactile or force feedback devices, research toward comprehensive haptic devices is limited [42–47]. Among these, no designs focus specifically on ER fluid's potential for device miniaturization. Mazursky et al. validated this idea experimentally with a small haptic button (14.5 mm thickness) based on ER fluid in flow mode driven by an elastic contact surface [11]. However, this study left room to further reduce the actuator's size and validate its performance mathematically. In a subsequent study, Mazursky et al. redesigned the actuator into a slimmer profile (5.4 mm thickness) with improved haptic resolution and a complementary mathematical model [48]. The details of these studies are elaborated upon in the following chapters.

## 2.3 Electrorheological Fluid: Behavior and Modeling

The haptic devices presented in this thesis are designed around the field-dependent behavior of ER fluids. To design a device around the dynamic behavior of ER fluid, it is important to understand the fluid's underlying mechanisms. In the following subsections, the properties and mechanics of ER fluid are reviewed and an overview of the state of ER fluid modeling is presented.

### 2.3.1 Properties and Behavior of ER Fluid

ER fluid was first discovered by Willis M. Winslow in the late 1940s [49]. ER fluids are fabricated by dispersing fine, electrically polarizable particles in an insulating carrier fluid and may include chemical additives for enhancement of specific characteristics. Under the application of an electric field, the particles, due to an induced dipole moment, align into fibrous networks parallel to the field lines (sometimes referred to as the Winslow effect) [50, 51]. This change in microstructure correlates to the property changes seen at bulk scale, such as viscosity and yield stress [52]. Under electric field, ER fluid transitions from nearly Newtonian behavior to viscoelastic. As shown in Figure 2.6, activated ER fluid will not flow unless acted upon by a stress greater than the induced yield stress.

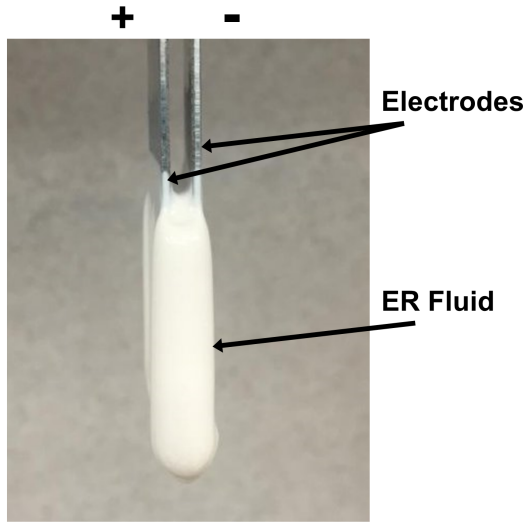


**Figure 2.6.** ER fluid suspended in an electric field between electrodes.

Devices utilizing ER fluids are typically configured in one of the following modes or a combination of the three: flow mode, shear mode and squeeze mode, as illustrated in Figure 2.7. Shown in Figure 2.7a, flow mode consists of flow between stationary electrodes due to pressure gradient. Flow mode is commonly implemented in ER dampers, shock absorbers and actuators [47, 53, 54]. Figure 2.7b shows ERF (electrorheological fluid) in shear mode, in which ER fluids flow between

parallel electrodes, where at least one electrode can translate (or rotate) relative to the other. Shear mode is usually applied to ER brakes, clutches and dampers [41, 55–57]. Lastly, the squeeze mode configuration is shown in Figure 2.7c. In contrast with the flow and shear modes, the electrode gap is varied in squeeze mode and flow is due to a normal force. Squeeze mode is generally less-researched than the former modes, but is mostly used in applications involving small, millimeter-scale displacements but large forces [58–60].

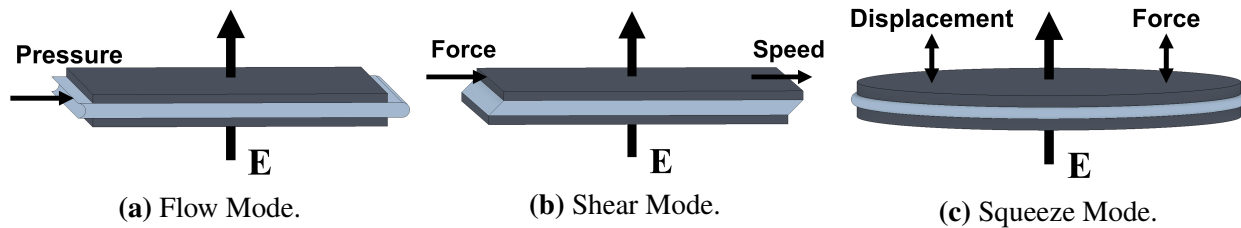


**Figure 2.7.** Operational modes for ER fluids (image adapted from [61]).

For some years, ER fluid was generally considered less applicable than MR fluid. Conventional ER fluid was not capable of producing yield stresses of the same magnitude as MR fluid. In 2003, Wen produced a major advancement in electro-rheology: the invention of giant electrorheological (GER) fluid [62]. Under an applied field strength of  $5 \text{ kV mm}^{-1}$ , Wen's GER fluid realizes a yield strength of 130 kPa, exceeding what was seen to be the upper bound of the theoretical ER fluid yield stress [63, 64]. These high yield stresses were achieved by coating nanoparticle suspensions in urea, shown below in Figure 2.8 [62]. In addition to its high yield strength, GER fluid exhibits response times under 10 ms [62]. This breakthrough has led to a renewed interest in applications of ER fluid in the past decade.

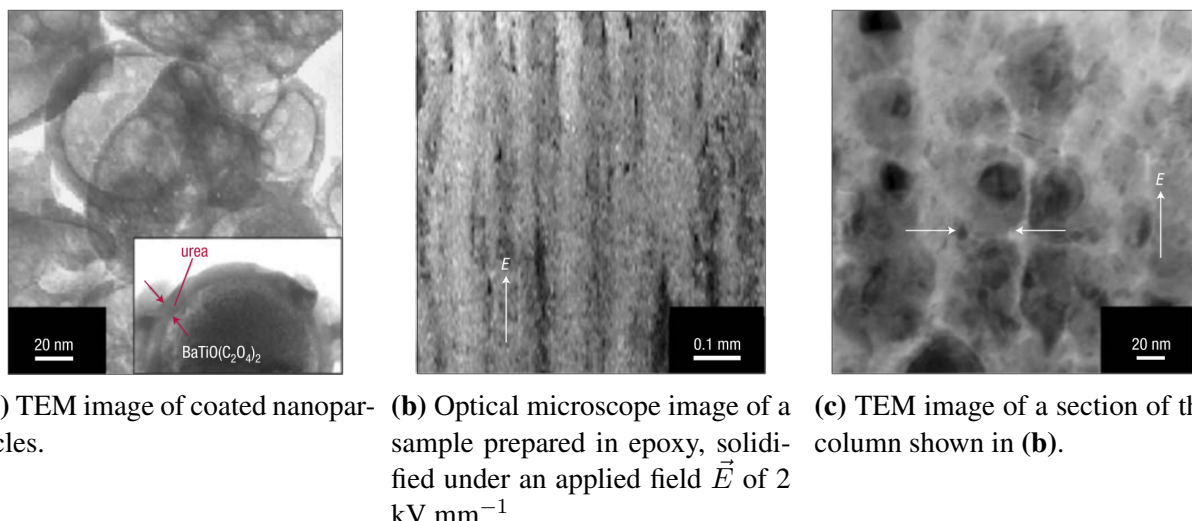


**Figure 2.8.** Images of nanoparticles in GER suspensions (image adapted from [62]).

### 2.3.2 Mathematical Modeling of ER Fluid

Over the years, a number of models have been developed to represent the flow of non-Newtonian fluids, which have shown potential for their application to flow-mode ER devices [65]. The principal models are: Bingham plastic model [66], biviscous material model [59], biplastic Bingham model [67], Herschel-Bulkley model [68, 69], and the Herschel-Bulkley model with biplasticity [70]. Some researchers have focused on using neural networks to nonparameterize fluid behavior, though these are more applicable in system control than design [71, 72].

Of these models, the earliest conceived and most prevalent in application has been the Bingham plastic model developed by Phillips in 1969. In the Bingham plastic model, the fluid's base viscosity  $\mu$  is taken to be constant. For the fluid to flow, the initial shear (or yield) stress  $\tau_0$  must be overcome. This can be represented mathematically [66]:

$$\tau = \tau_0 + \mu \frac{du}{dz} \quad (2.1)$$

where  $du/dz$  is the velocity gradient. The fluid viscosity,  $\mu$ , and the electric field-induced yield stress,  $\tau_0$ , are regarded as the most critical parameters when describing the fluid's behavior and in the design of ER fluid-based devices [65].

The coupling between fluid yield stress and applied electric field is also of great importance when designing ER devices and has been the subject of much experimental and theoretical research. To mitigate inconsistencies across experimental data caused by various material systems and measuring techniques, Choi, in 2001, introduced a generalized scaling function [73]:

$$\tau_y(E_0) = \alpha E_0^2 \left( \frac{\tanh \sqrt{E_0/E_c}}{\sqrt{E_0/E_c}} \right) \quad (2.2)$$

where  $\alpha$  is a measure of polarizability and  $E_0$  is the applied electric field strength. The critical electric field  $E_c$  denotes the transition point from the polarization model to the conduction model, characterized by:

$$\text{ER Fluid exhibits: } \begin{cases} \tau_y \propto E_0^2 & E_0 \ll E_c \quad (\text{polarization relation}) \\ \tau_y \propto E_0^{3/2} & E_0 \gg E_c \quad (\text{conduction relation}) \end{cases}$$

However, Choi's scaling function does not hold true for all GER fluids, where a linear relation

between field strength and yield stress is observed at strong applied fields:

$$\text{GER Fluid exhibits: } \begin{cases} \tau_y \propto E_0^2 & E_0 \ll E_c \\ \tau_y \propto E_0 & E_0 \gg E_c \end{cases}$$

To remedy this, Vemuri introduced a new scaling function specific to GER fluids [74]:

$$\tau_y(E_0) = \frac{\alpha E_0^2 I_1(E_0/E_c)}{(E_0/E_c) I_0(E_0/E_c)} \quad (2.3)$$

where  $I_1$  and  $I_0$  are *modified* Bessel functions of order 1 and 0, respectively. Zhang produced a generalized model that describes both conventional ER and GER fluids by introducing a material parameter  $\beta$  into Equation 2.2 [75]. Sections 3.4 and 4.2 focus on numerical modeling and adopt a Bingham relation and Vemuri's scaling function to represent ER fluid mechanics.

## 2.4 Closing Remarks

Upon reviewing the current state of touchable haptic devices, it is clear that commercial methods fall short of providing comprehensive haptic feedback due to an inability to convey kinesthetic sensations. While research has been performed to try to shrink traditional kinesthetic motors to mobile scale, many researchers have instead turned to smart materials as perhaps a mechanically simpler method. Of the smart materials discussed, smart fluids possess the rapid response times necessary for vibrotactile sensations and the high force outputs required for targeting kinesthetic sensations. The device proposed in this study utilizes ER fluid as a means of producing comprehensive haptic feedback in a compact package. In the following sections, the design, modeling and testing of the proposed actuator will be described in detail with a focus on conveying both components of haptic feedback.

# 3 | Haptic Actuator based on ER Fluid in Flow Mode

This chapter investigates the design, modeling and experimental evaluation of a slim haptic actuator based on ER fluids. The actuator is uniquely based upon pressure-driven flow of ER fluid between charged parallel plates, referred to as “flow mode.” The working principle, structural design, and prototype fabrication are established for two design iterations. The first design was manufactured primarily through 3D printing and was presented at SPIE Smart Structures + NDE 2018 [11]. Lessons were carried from the first design into an improved, printed circuit board (PCB) based design and was presented at ICAST 2018 and published in JIMSS [48, 76]. The final design is notable for its slim profile, which appeals to implementation within mobile electronic devices.

## 3.1 Proposed Actuator Design

To design the proposed haptic actuator, the working principles of using ER fluid in flow mode to produce haptic feedback were established and are first detailed in this section. The structural design of the actuator is then proposed. Finally, the fabricated prototype actuator is presented.

### 3.1.1 Working Principles

Figure 3.1 illustrates the cross-section and the working principle of the proposed haptic actuator. When pressing the actuator’s flexible contact surface, ER fluid flows radially outward through the gap between stationary electrodes, or the activation region. Therefore, it can be said that the actuator operates in pressure-driven flow mode. To compensate for the change in volume due to indentation, radial slots have been included, allowing the membrane inside the slots to expand elastically, creating a reciprocating reservoir (see Figure 3.1b). When pressure on the contact surface is released, the fluid is pushed by the contracting membrane from the reservoir and the device returns to its pre-contact state. When a voltage is applied to the electrodes, the ER fluid in the resultant electric field forms a fibrous network parallel to the field lines. This liquid-solid transition generates a yield stress with magnitude corresponding to the supplied voltage. Therefore, the force felt by the user’s finger when pressing directly corresponds to the yield stress produced by the fluid. For a range of supplied voltage magnitudes and frequencies, a range of feedbacks may be felt by the user.

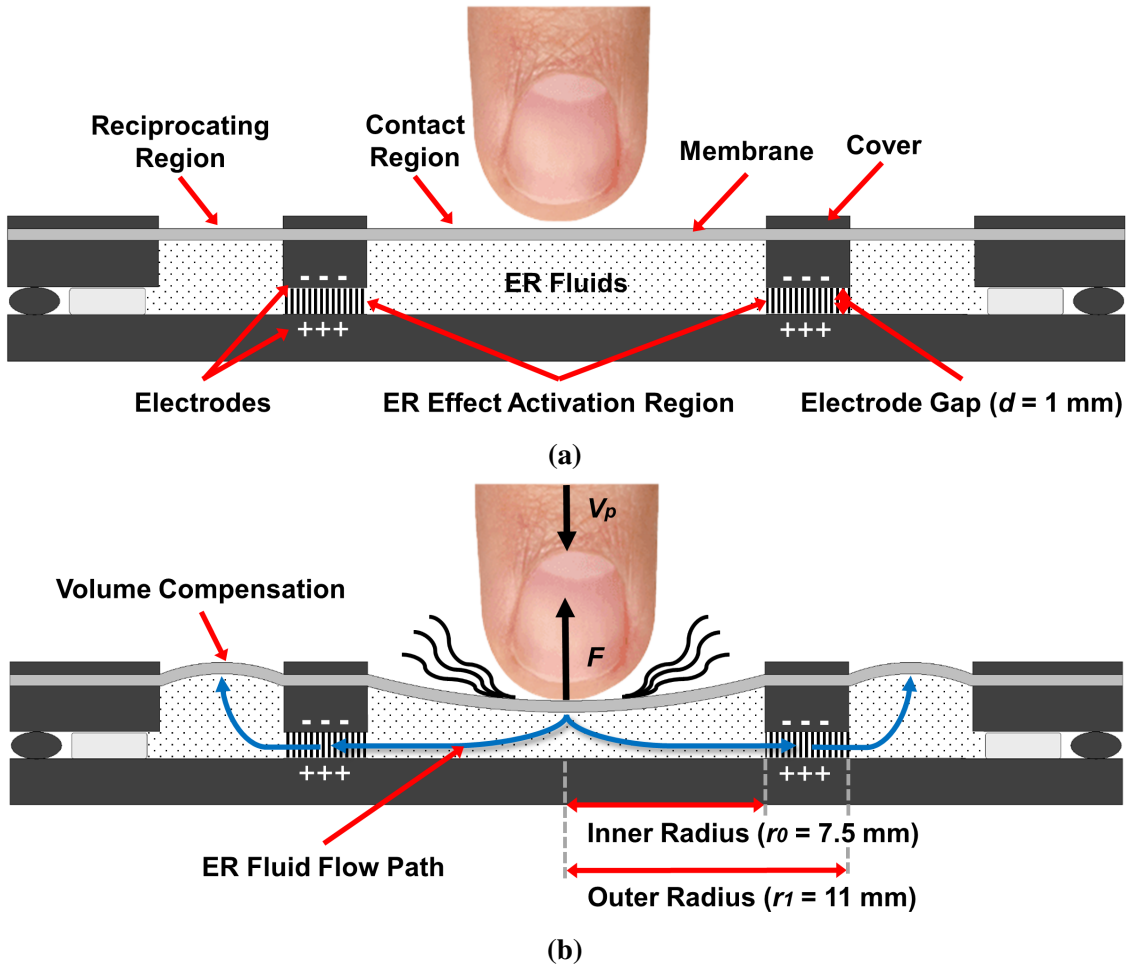


**Figure 3.1.** Working principle of the proposed flow mode haptic actuator **(a)** before contact and **(b)** mid-contact.

### 3.1.2 Structural Design

In this subsection, two design iterations are presented. Both operate on the previously described working principle.

#### 3D Printed Flow Mode Haptic Actuator

The 3D printed flow mode haptic actuator was developed through rapid prototyping and calculated trial-and-error. The objective for this preliminary design was to experimentally test the proposed working principle and evaluate the actuator's ability to produce kinesthetic and vibrotactile sensations. Experimental findings, described in full in the SPIE proceedings [11], were then taken into account in the subsequent design, the primary subject of this thesis.

A schematic view of the 3D printed haptic actuator is shown below in Figure 3.2. The two-

piece, plastic housing contains concentric electrode rings and ER fluid. The lower and upper electrodes are attached to the negative and positive halves of the housing, respectively, and are separated by a fixed, 1 mm gap. Conductive leads connect to the electrodes and are fed out through the side of the device to receive input voltage signals. The two halves of the housing are sealed by a groove fit. The actuator's volume is then filled with ER fluid and a thin silicone rubber membrane is placed over the top half of the device. The membrane is compressed against the upper surface of the positive housing by tightening the cover with nylon screws. The membrane therefore doubles as a seal and the actuator's contact surface. The assembled device measures 42 mm in diameter and 14.5 mm thick.

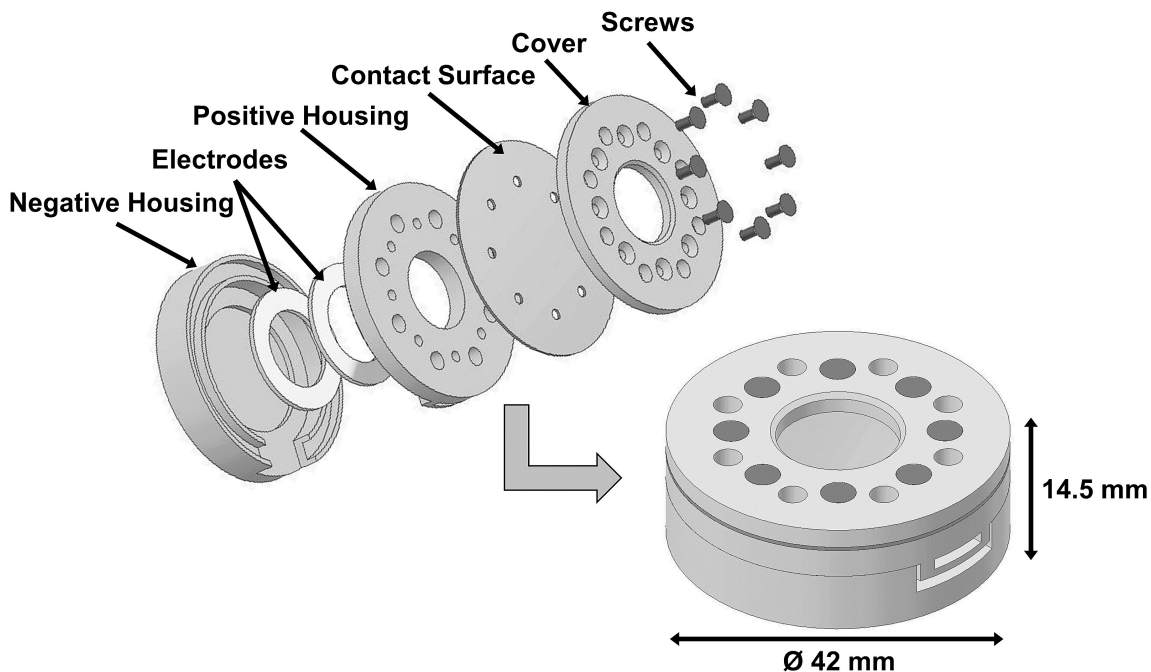


**Figure 3.2.** Exploded view drawing of the preliminary, 3D printed flow mode haptic actuator.

### **PCB Flow Mode Haptic Actuator**

Having validated the working principle through the 3D printed actuator, the next haptic actuator aims to address inefficiencies of the previous design. Specifically, it simplifies the manufacturing process by combining structure and electrical control via printed circuit boards (PCBs). The number of fasteners was reduced and groove fit seal was replaced with an o-ring, eliminating the need for adhesives and yielding a cleaner assembly process. These design changes resulted in a significantly slimmer design.

A schematic view of the proposed PCB flow mode haptic actuator is presented in Figure 3.3. The structure is composed of two PCB electrodes and an elastic membrane contact surface. The

internal volume of the device contains ER fluid. The bottom PCB has an annulus-type electrode and is rated for high voltages (HV PCB). A plastic ring is fitted between the two PCBs, providing rigidity to the O-ring seal and sets the gap distance between the electrodes to 1 mm. The top PCB has identical electrode geometry to the HV PCB and functions as grounding (GND PCB) for the applied electric field. A compliant silicone membrane is sealed by a thin layer of acrylic tape to the top of the GND PCB and functions as the device's contact surface. Nylon nuts and bolts fasten the device and compress the O-ring and membrane seals to secure the ER fluid inside. Two tabs allow for HV and GND leads to be secured to the electrode PCBs for electrical inputs. The assembled device measures 42 mm in diameter and 5.4 mm thick.

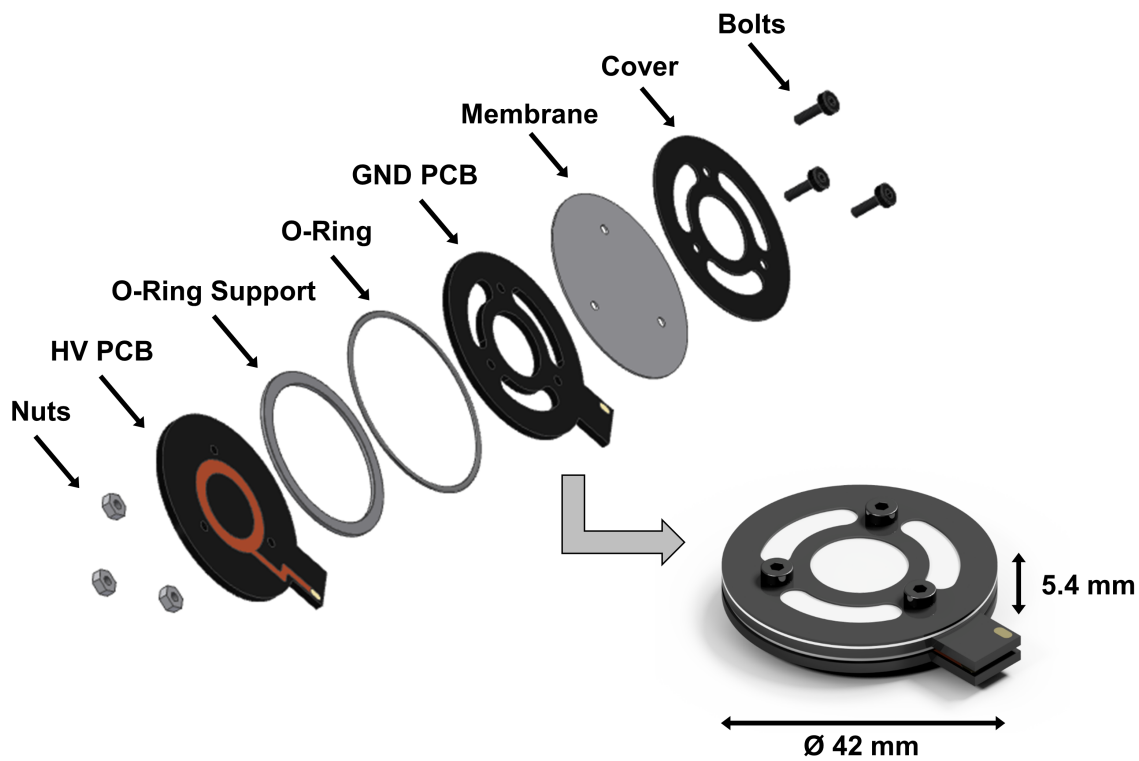


**Figure 3.3.** Exploded view drawing of the proposed PCB flow mode haptic actuator.

### 3.1.3 Fabrication

Figure 3.4 shows the constructed components and assembly of the PCB-based prototype actuator. The button-type actuator is comprised of two electrode PCBs, a plastic spacer and O-ring, a thin film silicone membrane and a plastic cover. The HV PCB was treated with a thin polyimide (PI) film to prevent arcing at high voltages. The electrode's inner and outer radii measure 7.5 and 11 mm, respectively. The internal volume of the actuator is filled with 1.8 mL of GER fluid (Smart

Materials Laboratory Ltd., Hong Kong), thus providing potential for greater yield stresses than conventional ER fluid. Properties of the GER fluid are provided below in Table 3.1. The maximum indentation depth or stroke of the actuator is about 1 mm. The device was designed and manufactured with a goal of minimizing thickness to convey kinesthetic and tactile feedback in miniature applications. The size of the proposed actuator is significantly thinner than (or comparable to) previous designs utilizing smart materials [11, 32, 77, 78]. Additionally, the design is mechanically simple and easily controllable.

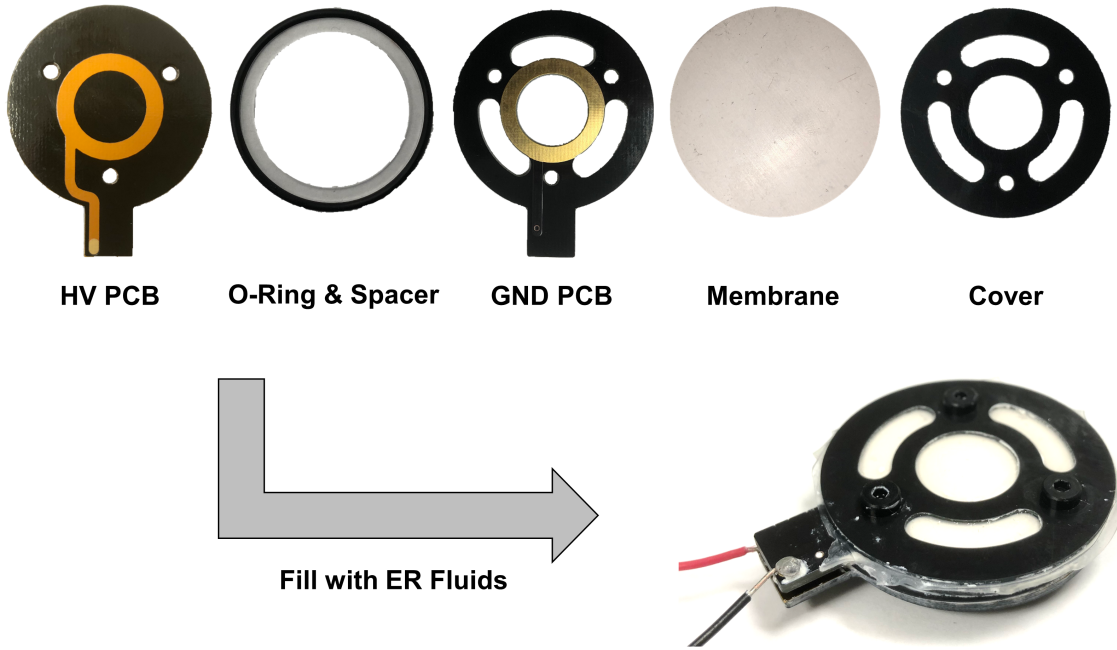


**Figure 3.4.** Construction and assembly of the prototype PCB-based flow mode actuator.

**Table 3.1.** Material properties of GER fluid at 25°C (Smart Materials Laboratory Ltd., Hong Kong).

Parameter	Description
Color	White
Density $\rho$	1.4 kg/l
Solid Content	65 %–Mass
Dynamic Viscosity $\mu$	0.06 Pa·s
Avg. Particle Diameter	0.1 $\mu\text{m}$
Yield Point $\tau$	80 kPa at 5 kV/mm
Stationary Current Density	4 $\mu\text{A}/\text{cm}^2$ at 2 kV/mm
Response Time	< 3 ms

## 3.2 Analytical Modeling of ER Fluid Mechanics

**Actuator Modeling Overview:** To understand the actuator's performance from a mathematical perspective, a model was developed based on the actuator's fundamental behavior. First, an analytical solution to the resistive force produced by the actuator over its stroke as a function of applied electric field was derived and is presented in this section. Modeling of the actuator's contact membrane mechanics is performed in Section 3.3. Next, a numerical approach is taken to simulate the actuator's resistive force output and is presented in Section 3.4. Later, parametric studies are performed on the numerical model to investigate the effect of actuator geometry on force output, discussed in Section 3.7. These insights may be applied to the design of future iterations.

To characterize the behavior of the proposed haptic actuator, an analytical model was developed to determine the resistive force produced by the actuator based on the nondimensional approach taken by Hong [70]. First, boundary conditions are applied to the Navier-Stokes equation (1), resulting in the velocity profile of the fluid flow between the plates (2). Integrating about the electrode area returns the total flow rate (3). From the volume continuity condition, the flow rate between the plates must be equal to the flow rate due to the indenter; therefore, the pressure gradient may be realized (4). The pressure gradient is then used to attain the pressure drop across the plates and the contribution of the ER fluid to the resistive force produced by the actuator (5). Further detail to each of these steps is provided with mathematical representations in the following subsubsections.

### 3.2.1 Navier-Stokes Equation and Assumptions

Upon indenting the contact membrane at a rate of  $V_p$ , ER fluid flow develops between the parallel electrodes. As shown in Figure 3.5, the velocity profile in the activation region is composed of three regions due to the Bingham plastic behavior of ER fluid. Flow near the electrode walls (regions 1 and 3) is where the shear stress is greatest and where yield occurs ( $|\tau| > \tau_y$ ). Near the center of the gap (region 2, also known as the plug or core), unyielded fluid flows with a uniform velocity. A parallel plate approximation is made to estimate the annular electrodes as a rectangular duct [79].

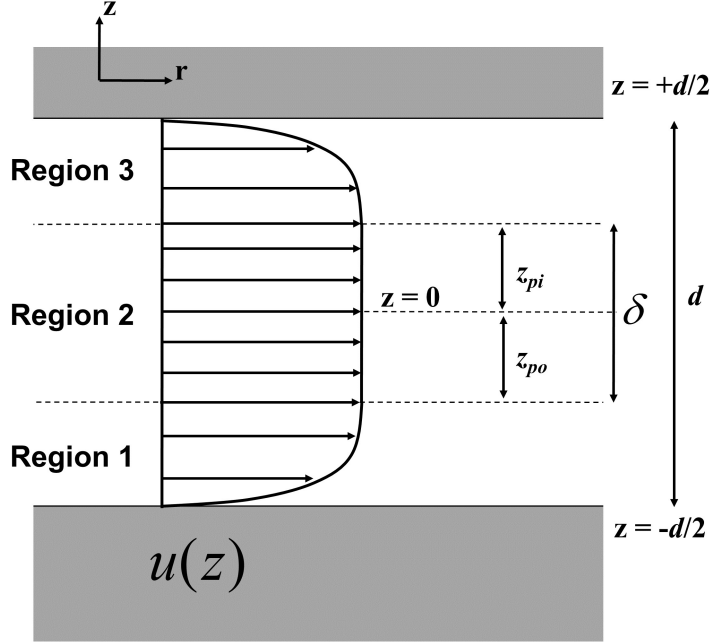


**Figure 3.5.** Velocity profile of ER fluid in the activation region associated with a fixed electrode configuration.

To find the velocity profile  $u(z)$  in flow mode, the Navier-Stokes equation of motion in rectangular coordinates along the x-direction is given:

$$\rho \left( \frac{\partial u}{\partial t} + u \frac{\partial u}{\partial x} + v \frac{\partial u}{\partial y} + w \frac{\partial u}{\partial z} \right) = - \frac{dp}{dx} + \rho g_x + \mu \left( \frac{\partial^2 u}{\partial x^2} + \frac{\partial^2 u}{\partial y^2} + \frac{\partial^2 u}{\partial z^2} \right) \quad (3.1)$$

Equation 3.1 may be simplified by applying the following conditions:

1. Steady Flow:  $\frac{\partial u}{\partial t} = 0$
2. Unidirectional Flow:  $V_x \neq 0, V_y = V_z = 0 \rightarrow v = w = 0$
3. Mass Conservation:  $\frac{\partial u}{\partial x} = 0$
4. Gravity:  $g_x = 0$
5. Velocity in the x-direction,  $u$ , is a function of vertical position  $z$

These conditions yield the simplified relation between pressure gradient and flow profile:

$$\frac{dp}{dx} = \mu \frac{d^2 u}{dz^2} \quad (3.2)$$

To better illustrate the physical relation to the actuator design, the variable  $x$  is renamed to  $r$ .

### 3.2.2 Boundary Conditions and Flow Velocity $u$ in each Region

To find the flow velocity in each region  $u_i$ , where  $i = 1, 2, 3$  and denotes flow region, divide by  $\mu$  and integrate twice with respect to  $z$ :

$$u_i(z) = \frac{1}{2\mu} \frac{dP}{dr} z^2 + C_1 z + C_2 \quad (3.3)$$

where  $C_1$  and  $C_2$  are constants of integration. By applying the boundary conditions in each region of the flow, shown in Figure 3.5, the flow velocity particular to each region is found:

#### **Region 1** ( $-\frac{d}{2} \leq z \leq -z_{po}$ )

Boundary Conditions:

- At electrode wall ( $z = -\frac{d}{2}$ ):  $u_1 = 0$
- At plug boundary ( $z = -z_{po}$ ):  $u'_1 = 0$

Substituting these conditions to solve for the constants of integration yields:

$$C_1 = \frac{1}{\mu} z_{po} \frac{dP}{dr}$$

$$C_2 = \frac{1}{2\mu} dz_{po} \frac{dP}{dr} - \frac{1}{2\mu} \frac{d^2}{4} \frac{dP}{dr}$$

Upon substituting  $C_1$  and  $C_2$  into Equation 3.3 and simplifying gives the flow in Region 1:

$$u_1(z) = \frac{1}{2\mu} \frac{dP}{dr} \left[ (z + z_{po})^2 - \left( \frac{d}{2} - z_{po} \right)^2 \right] \quad (3.4)$$

#### **Region 3** ( $z_{pi} \leq z \leq \frac{d}{2}$ )

Flow in Region 3 is symmetric to that of Region 1.

Boundary Conditions:

- At electrode wall ( $z = \frac{d}{2}$ ):  $u_3 = 0$
- At plug boundary ( $z = z_{pi}$ ):  $u'_3 = 0$

Again, the constants of integration are found:

$$C_1 = -\frac{1}{\mu} z_{pi} \frac{dP}{dr}$$

$$C_2 = \frac{1}{2\mu} dz_{pi} \frac{dP}{dr} - \frac{1}{2\mu} \frac{d^2}{4} \frac{dP}{dr}$$

The flow in Region 3 may be written as:

$$u_3(z) = \frac{1}{2\mu} \frac{dP}{dr} \left[ (z - z_{pi})^2 - \left( \frac{d}{2} - z_{pi} \right)^2 \right] \quad (3.5)$$

## **Region 2 ( $-z_{po} \leq z \leq z_{pi}$ )**

Boundary Conditions:

- At upper plug boundary ( $z = z_{pi}$ ):  $u_2 = u_3(z_{pi})$
- At lower plug boundary ( $z = -z_{po}$ ):  $u_2 = u_1(-z_{po})$

Note that for stationary plates,  $z_{pi} = z_{po}$ .

Substituting yields the equation of flow in the plug region:

$$u_2 = -\frac{1}{2\mu} \frac{dP}{dr} \left( \frac{d}{2} - z_{pi} \right)^2 \quad (3.6)$$

## **Plug Thickness**

Having found the velocity in each region, the plug thickness  $\delta$  must be derived. To do so, the hydrostatic force on an element is considered in Figure 3.6:

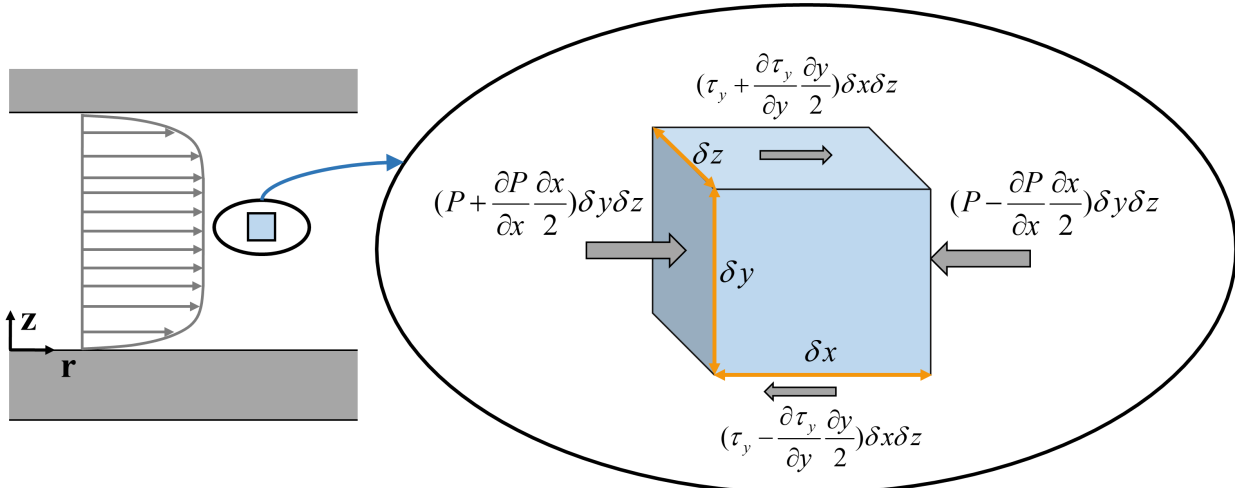


**Figure 3.6.** Control volume element for a fixed electrode form.

Examining the hydrostatic force balance gives:

$$\left( P + \frac{\partial P}{\partial x} \frac{\partial x}{2} \right) \delta y \delta z - \left( P - \frac{\partial P}{\partial x} \frac{\partial x}{2} \right) \delta y \delta z + (\tau_y) \delta x \delta z + (\tau_y) \delta x \delta z = 0 \quad (3.7)$$

Reducing leads to the relation for plug thickness  $\delta$ :

$$\delta = -\frac{2\tau_y}{dP/dx} \quad (3.8)$$

The components of plug thickness,  $z_{pi}$  and  $z_{po}$ , may then be found by considering:

$$u_1(-z_{po}) = u_3(z_{pi})$$

It becomes clear that  $z_{pi} = z_{po}$ . Since  $\delta = z_{pi} + z_{po}$ :

$$z_{pi} = z_{po} = \frac{\delta}{2} \quad (3.9)$$

## Summary of Velocity Profile

In summary, the flow follows the profile defined by the piecewise function:

$$u(z) = \begin{cases} \frac{1}{2\mu} \frac{dP}{dr} \left[ (z + \frac{\delta}{2})^2 - (\frac{d}{2} - \frac{\delta}{2})^2 \right] & -\frac{d}{2} \leq z \leq -\frac{\delta}{2} \\ -\frac{1}{2\mu} \frac{dP}{dr} \left( \frac{d}{2} - \frac{\delta}{2} \right)^2 & -\frac{\delta}{2} \leq z \leq \frac{\delta}{2} \\ \frac{1}{2\mu} \frac{dP}{dr} \left[ (z - \frac{\delta}{2})^2 - (\frac{d}{2} - \frac{\delta}{2})^2 \right] & \frac{\delta}{2} \leq z \leq \frac{d}{2} \end{cases} \quad (3.10)$$

### 3.2.3 Total Flow Rate $Q$

Having found  $u(z)$ , we may find the volumetric flow rate,  $Q$ , by utilizing the definition:

$$Q = \iint_A u \, dA$$

or often:

$$Q = b \int u \, dz$$

where  $b$  is the width of the electrode, in this case, the circumference. However, circumference changes with position along  $r$  radially or  $x$  cardinally. Therefore, the complete double integral

must be evaluated for this case:

$$Q = \int_{2\pi r_0}^{2\pi r_1} \int_{-\frac{d}{2}}^{\frac{d}{2}} u \, dz \, dr$$

where  $r_1$  and  $r_0$  are the outer and inner electrode radii, respectively. separate the integration among each of the regions and sum the components to find the total flow rate  $Q_{total}$ :

$$Q_{total} = Q_1 + Q_2 + Q_3 \quad (3.11)$$

The integrals evaluated in this subsubsection have been completed with the help of MATLAB®'s symbolic toolbox. First,  $Q_1$  is evaluated:

$$\begin{aligned} Q_1 &= \int_{2\pi r_0}^{2\pi r_1} \int_{-\frac{d}{2}}^{-\frac{\delta}{2}} \frac{1}{2\mu} \frac{dP}{dr} \left[ (z + \frac{\delta}{2})^2 - (\frac{d}{2} - \frac{\delta}{2})^2 \right] dz \, dr \\ Q_1 &= \int_{2\pi r_0}^{2\pi r_1} -\frac{1}{24\mu} \frac{dP}{dr} (d - \delta)^3 \, dr \\ Q_1 &= \frac{\pi}{12\mu} \frac{dP}{dr} (d - \delta)^3 (r_0 - r_1) \end{aligned} \quad (3.12)$$

Similarly, solving for  $Q_2$ :

$$\begin{aligned} Q_2 &= \int_{2\pi r_0}^{2\pi r_1} \int_{-\frac{\delta}{2}}^{\frac{\delta}{2}} -\frac{1}{2\mu} \frac{dP}{dr} \left( \frac{d}{2} - \frac{\delta}{2} \right)^2 dz \, dr \\ Q_2 &= \int_{2\pi r_0}^{2\pi r_1} -\frac{\delta}{8\mu} \frac{dP}{dr} (d - \delta)^2 \, dr \\ Q_2 &= \frac{\pi\delta}{4\mu} \frac{dP}{dr} (d - \delta)^2 (r_0 - r_1) \end{aligned} \quad (3.13)$$

Finally,  $Q_3$ :

$$\begin{aligned} Q_3 &= \int_{2\pi r_0}^{2\pi r_1} \int_{\frac{\delta}{2}}^{\frac{d}{2}} \frac{1}{2\mu} \frac{dP}{dr} \left[ (z - \frac{\delta}{2})^2 - (\frac{d}{2} - \frac{\delta}{2})^2 \right] dz \, dr \\ Q_3 &= \int_{2\pi r_0}^{2\pi r_1} -\frac{1}{24\mu} \frac{dP}{dr} (d - \delta)^3 \, dr \\ Q_3 &= \frac{\pi}{12\mu} \frac{dP}{dr} (d - \delta)^3 (r_0 - r_1) \end{aligned} \quad (3.14)$$

$Q_{total}$  is now found using Equation 3.11 and simplifying:

$$Q_{total} = \frac{\pi}{12\mu} \frac{dP}{dr} (d - \delta)^2 (2d + \delta)(r_0 - r_1) \quad (3.15)$$

### 3.2.4 Pressure Gradient $dP/dr$

To solve for the pressure gradient, the conservation of incompressible mass flow rate condition is utilized:

$$Q_{total} = Q_{piston} \quad (3.16)$$

where  $Q_{piston} = V_p A_p(\delta_i)$  is the flow rate due to the membrane's displacement. The area of the piston is a function of the instantaneous pressed depth  $\delta_i$ . Equation 3.16 is expanded below by filling in  $Q_{total}$  with Equation 3.15 with  $\delta$  defined by Equation 3.8:

$$V_p A_p(\delta_i) = \frac{\pi}{12\mu} \frac{dP}{dr} \left( d + \frac{2\tau_y}{dP/dr} \right)^2 \left( 2d - \frac{2\tau_y}{dP/dr} \right) (r_0 - r_1) \quad (3.17)$$

For the given geometry,  $\frac{dP}{dr}$  may be written as:

$$\frac{dP}{dr} = -\frac{\Delta P}{r_1 - r_0} \quad (3.18)$$

Substituting into Equation 3.17 results in the equation of pressure gradient:

$$V_p A_p(\delta_i) = \frac{\Delta P}{12\mu} \left( 2d - \frac{2\tau_y(r_0 - r_1)}{\Delta P} \right) \left( d + \frac{2\tau_y(r_0 - r_1)}{\Delta P} \right)^2 \quad (3.19)$$

A MATLAB® script was used to solve for  $\Delta P$  symbolically. Three solutions were found, but only the first root makes physical sense, as detailed by Phillips in his 1969 dissertation on “Engineering Applications of Fluids with a Variable Yield Stress” [66]. The solution may be simply approximated as the classical result:

$$\Delta P = \frac{12\mu A_p L}{bd^3} \dot{x} + 2 \frac{L}{d} \tau_y \operatorname{sgn}(\dot{x}) \quad (3.20)$$

where  $b$  is the electrode width,  $L$  is the electrode length for an equivalent rectangular duct, and  $x$  refers to the membrane's displacement.

### 3.2.5 Resistive Force $F$

Finally, to determine the resistive force felt by the user due to the flow mode of the ER fluid, the pressure drop across the electrodes is multiplied by the area of the indenter:

$$F = \Delta P A_p \quad (3.21)$$

Using the classical pressure gradient yields:

$$F = \frac{12\mu A_p^2 L}{bd^3} \dot{x} + 2 \frac{LA_p}{d} \tau_y \operatorname{sgn}(\dot{x}) \quad (3.22)$$

Here, the term containing  $\mu$  is associated with the inherent damping force of the fluid, while the term containing  $\tau_y$  is the contribution of the fluid's yield effect. For a membrane-based contact surface, the indenter or finger area varies with depth, resulting in a nonlinear volumetric flow rate. Therefore, the volumetric flow may be approximated:

$$A_p = \pi r_{pf}^2 \frac{\delta_i}{\delta_f} \quad (3.23)$$

where  $r_{pf}$  is the final radius of the indenter. The dimensionless  $\delta_i/\delta_f$  term compares the current indentation depth to the final depth.

### 3.3 Analytical Modeling of Membrane Mechanics

The resistive force represented by Equation 3.21 only accounts for the force due to the ER fluid's performance. When a user interacts with the proposed button-type actuator, additional resistive forces are present due to the elastic force of the membrane. This force is produced through both contact and the resulting reciprocation, as shown in Figure 3.7. An analytical model for the force generated through the membrane's elastic deformation is produced based on derivations by Komaragiri and Vlassak [80, 81]. As described in subsubsection 3.1.2, the membrane consists of two layers: contact and adhesive. The contact layer of the membrane, made of PDMS, is taken to behave as a nonlinear membrane without pre-strain, while the adhesive layer of the membrane, made of acrylic tape (3M™ VHB 4910), is taken to behave as a linear, pre-stretched membrane. By superposing the force-displacement curves produced by each layer, the analytical result may accurately capture the experimental behavior and provide a complete theoretical model of the actuator's performance.

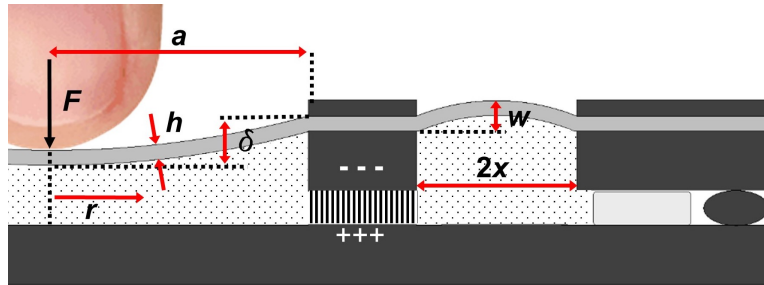


**Figure 3.7.** Schematic diagram of the dimensions used in the membrane load-deflection analysis.

### 3.3.1 Nonlinear PDMS Layer (without pre-strain)

First, the circular contact membrane is examined. An approximate solution to the midpoint deflection of a thin, circular membrane without pre-strain is given [81]:

$$\frac{\delta}{a} = g(\nu) \left( \frac{pa}{Eh} \right)^{1/3} \quad (3.24)$$

where  $\delta$  is the midpoint deflection,  $p$  is the applied pressure,  $a$  is the radial span,  $E$  is the elastic modulus,  $h$  is the thickness of the membrane, and  $g(\nu) \approx 0.7179 - 0.1706\nu - 0.1495\nu^2$ , where  $\nu$  is the film's Poisson's ratio. Since the proposed study describes a strain-controlled model and experiment, the pressure as a result of strain is of interest. Rearranging yields:

$$p = \frac{E\delta^3 h}{a^4 g(\nu)^3} \quad (3.25)$$

The reciprocating membrane is approximated as three rectangular films. The load-deflection relation for high aspect ratio films may be represented as [80]:

$$q = \frac{4Eh}{3x^4(1-\nu^2)} w^3 \quad (3.26)$$

where  $x$  is the membrane width,  $w$  is the deflection at the midpoint of the reciprocating membrane and  $q$  is the pressure on the reciprocating membrane. Deflection at the midpoint of the reciprocating membrane is related to the contact membrane deflection by conservation of fluid volume.

### 3.3.2 Linear VHB Layer (pre-strained)

An approximate solution to the midpoint deflection of a thin, circular membrane with pre-strain is given [81]:

$$\delta = a \int_1^0 \beta(\bar{r}) \, d\bar{r} \quad (3.27)$$

where angle of rotation  $\beta$  is defined:

$$\beta(\bar{r}) = -\frac{6(1-\nu^2)}{\kappa^2} \left( \frac{pa^3}{Eh^3} \right) \left[ \bar{r} - \frac{I_1(k\bar{r})}{I_1(k)} \right] \quad (3.28)$$

where  $I_1$  denotes Bessel's function of the first kind. The terms  $\kappa$ ,  $k$  and  $\bar{r}$  are defined as:

$$\begin{aligned}\kappa^2 &= 12\varepsilon_0(1 + \nu)\left(\frac{a}{h}\right)^2 \\ k &= (1 - \nu)^{-1} \\ \bar{r} &= \frac{a}{r}\end{aligned}\tag{3.29}$$

where  $\varepsilon_0$  is the pre-strain and  $r$  is the radial position. This system of equations is evaluated to find pressure as a result of applied strain.

Similarly, the load-deflection for a pre-stretched rectangular membrane with high aspect ratio is shown to be [80]:

$$q = 2\frac{\sigma_0 h}{x^2}w + \frac{4Eh}{3x^4(1 - \nu^2)}w^3\tag{3.30}$$

where  $\sigma_0$  is the pre-stress.

### 3.4 Numerical Evaluation of the Proposed Actuator

To simulate the actuator's behavior, a MATLAB® script was developed based on the modeling presented in the previous subsections to calculate the forces produced over the actuator's stroke. The model accounts for both the force produced by the elastic contact surface and the ER fluid effect. A coupling between the applied electric field and the giant ER fluid's yield stress was established using properties provided by the manufacturer (Smart Materials Laboratory Ltd., Hong Kong), such as a maximum yield stress of 80 kPa at 5 kV mm<sup>-1</sup>, and was represented with the GER scaling function presented in Equation 2.3 [74]. The yield stress curve is presented in Figure 3.8. The yield stress due to the electric field is used as an input to determine the ER actuator force. Parameters critical to the numerical results of the ER effect and membrane kinematics are provided below in Tables 3.2 and 3.3. Values used reflect the properties of the fabricated prototype actuator and the experimental test setup.

**Table 3.2.** Parameters of the proposed haptic actuator.

Parameter	Symbol	Value
Electrode Gap	$d$	1 mm
Electrode Radius (Inner)	$r_0$	7.5 mm
Electrode Radius (Outer)	$r_1$	11 mm
Viscosity of GER Fluid	$\mu$	0.060 Pa·s
Radius of Indenter	$r_p$	5.9 mm
Velocity of Indentation	$V_p$	1 mm/s

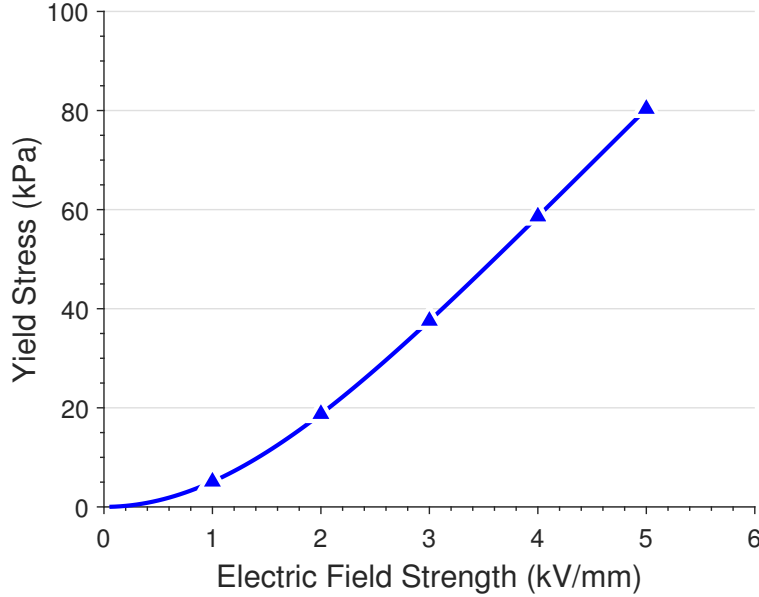


**Figure 3.8.** Yield stress plotted as a function of applied electric field for the purchased GER fluid.

**Table 3.3.** Parameters of the membrane model.

Parameter	Symbol	Value (PDMS)	Value (VHB)
Radial span	$a$	7.5 mm	7.5 mm
Width	$x$	2.34 mm	2.34 mm
Thickness	$h$	0.43 mm	0.08 mm
Pre-strain	$\varepsilon_0$	0	0.065
Pre-stress	$\sigma_0$	0	50 kPa
Elastic modulus	$E$	350 kPa	60 kPa
Poisson's ratio	$\nu$	0.50	0.49

The membrane's force-displacement behavior was simulated by imposing indentation from 0 to 1 mm at the center of the contact membrane and calculating the resulting force, shown in Figure 3.9. As shown, the pre-strained acrylic tape layer (VHB) responds linearly while the relaxed contact layer (PDMS) exhibits nonlinear behavior. Together, the two layers contribute to the total combined membrane response. At the bottom of the stroke, the contact and reciprocating membranes contribute about 0.5 N and 2.1 N, respectively. The combined membrane performance is utilized in the complete numerical simulation of the actuator performance.

The approximation of volumetric flow rate due to the indenter or finger is another critical component of the model. Using the parameters in Table 3.2 and Equation 3.23, Figure 3.10 is produced.

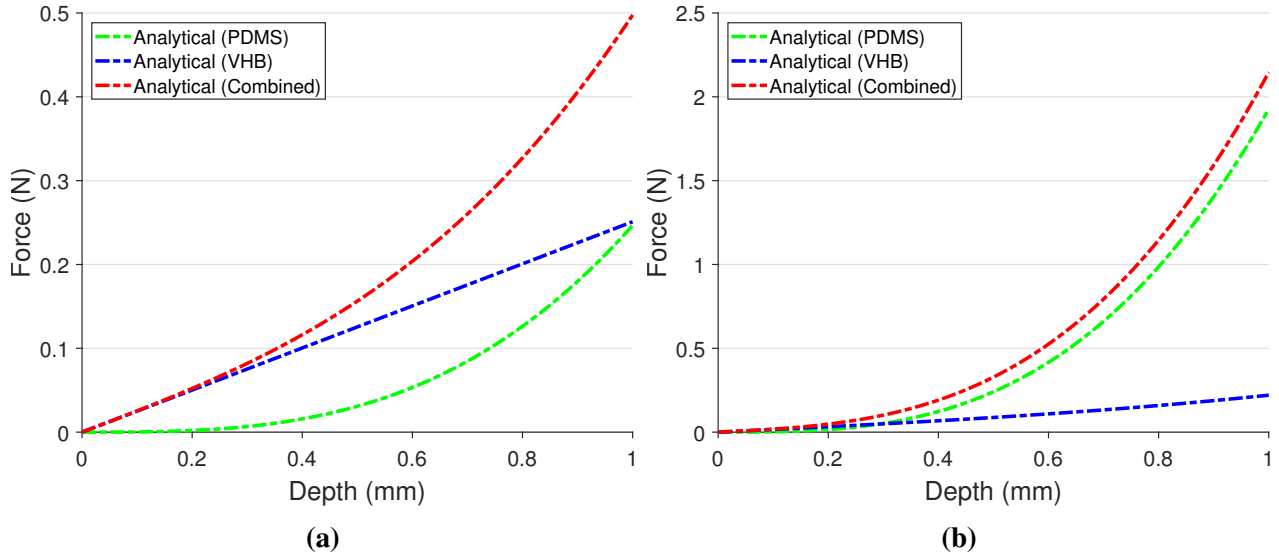
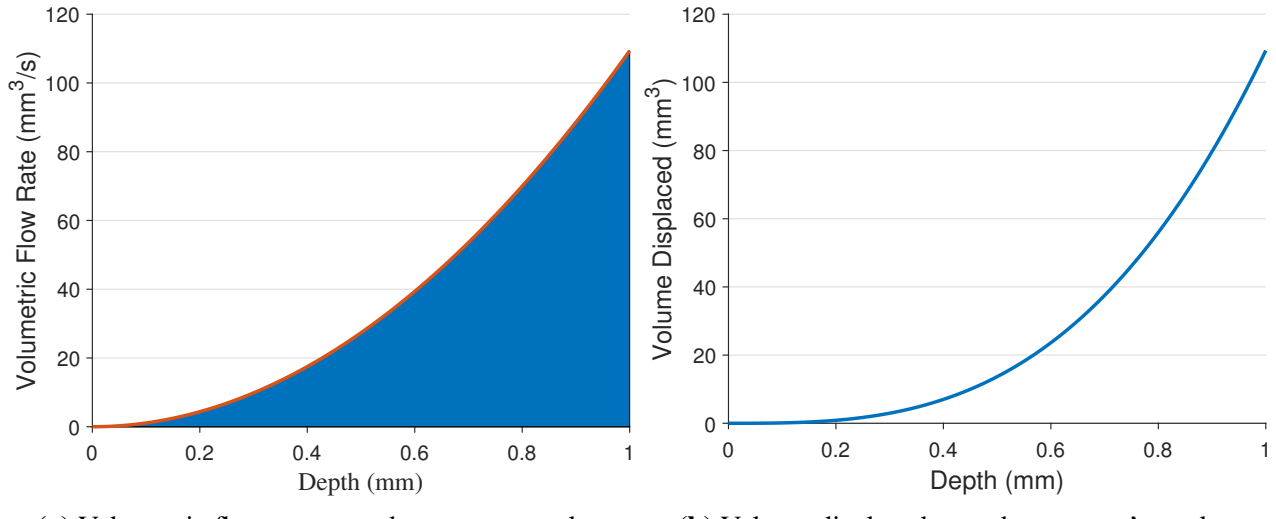


**Figure 3.9.** Simulation results for the force produced by indenting the superposed membrane in the (a) contact and (b) reciprocating regions.



(a) Volumetric flow rate over the actuator stroke. (b) Volume displaced over the actuator's stroke.

**Figure 3.10.** Approximation of volumetric flow due to indentation.

The simulation takes applied voltage and frequency as inputs and produces plots of the force generated by the actuator along its indentation stroke. Figure 3.11a shows the force profiles predicted by the simulation when subjected to DC voltage inputs of 0, 1, 2, 3, and 4 kV. As shown, when no power is supplied to the actuator (0 kV, or off-state), the maximum force produced is about 2.5 N at the bottom of the stroke. When the maximum voltage is supplied (4 kV DC), the maximum force increases to nearly 3.6 N. Figure 3.11b shows the force profiles predicted when the model is subjected to sinusoidal excitation between 0 V and 1, 2, 3, and 4 kV at a frequency of 5 Hz. It is seen that as the magnitude of the voltage increases, the amplitude of vibration in-

creases. Therefore, the simulation implies that the design is capable of providing both kinesthetic and vibrotactile feedback.

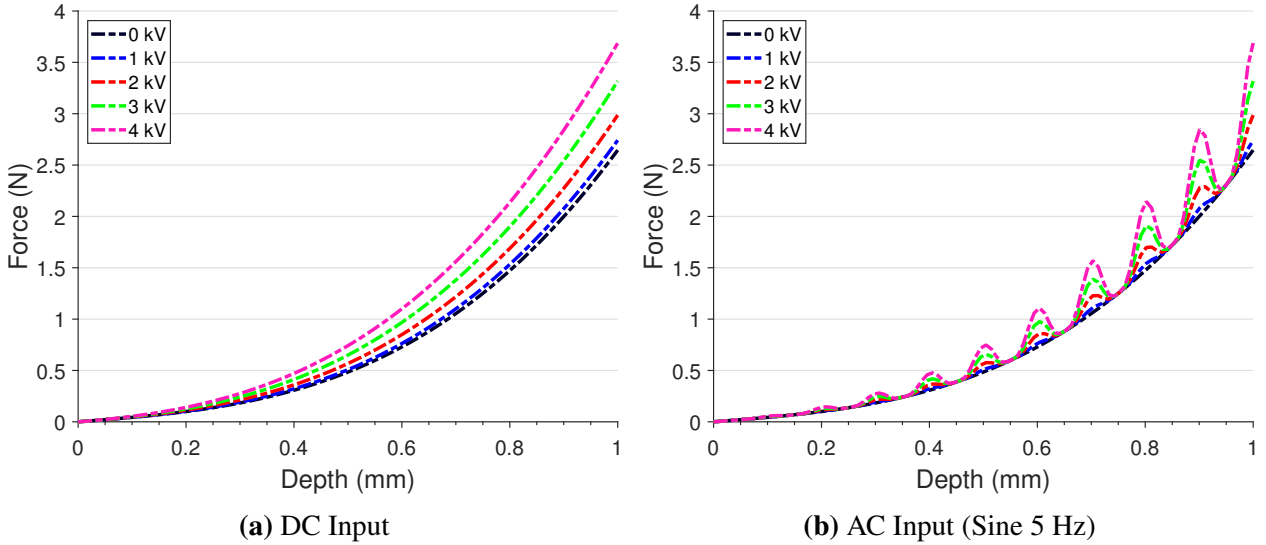


**Figure 3.11.** Results of the simulated flow mode actuator: force (N) vs. depth (mm) along its stroke.

## 3.5 Experimental Evaluation of the Fabricated Actuator

This section presents the experimental methods for testing the fabricated haptic device and analysis of the experimental results. The goal of the experimental analysis is to measure the device's ability to produce a significant range of kinesthetic and vibrotactile sensations. An experimental method of measuring the actuator's output with respect to depth for voltage inputs is described.

### 3.5.1 Experimental Setup

To evaluate the performance of the fabricated haptic actuator, mechanical analysis was conducted using a dynamic mechanical analyzer (RSA3, TA Instruments), function generator, and voltage amplifier (Trek Model 609E-6, 1000 V/V), as shown in Figure 3.12. This experimentation precisely measured the total resistive force with respect to indentation depth over the device's 1 mm stroke. The performance was evaluated under different input voltage and frequency conditions using an indenter similar in size to a human finger. An indentation rate of 1 mm/s was used.

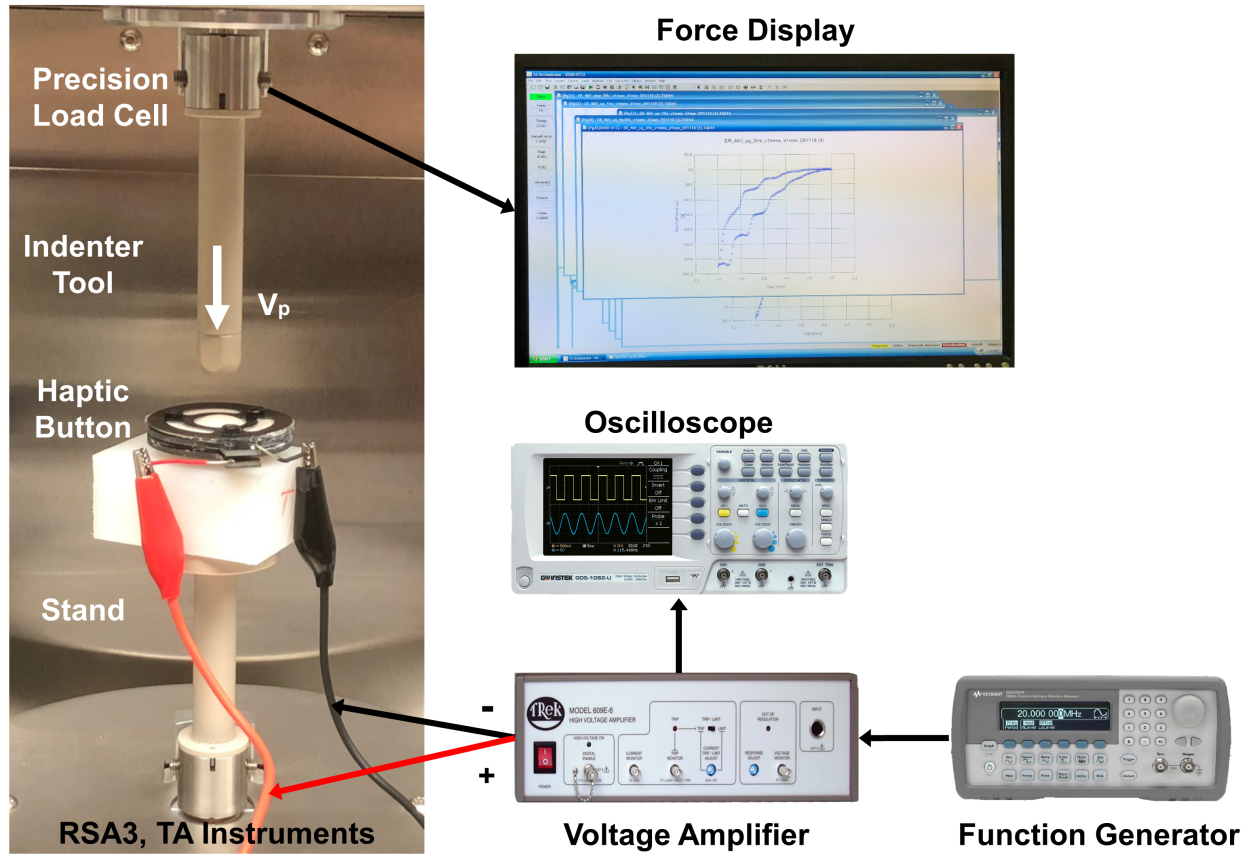


**Figure 3.12.** Experimental setup to measure the force generated by the prototype actuator with respect to indentation depth for applied voltage signals.

### 3.5.2 Membrane Response

To first validate the modeled membrane's response, dry testing was performed with an assembled actuator containing no ER fluid. Figure 3.13 compares the simulated and experimental membrane response. The analytical membrane model is demonstrated to be sufficiently accurate when plotted against the experimental response.

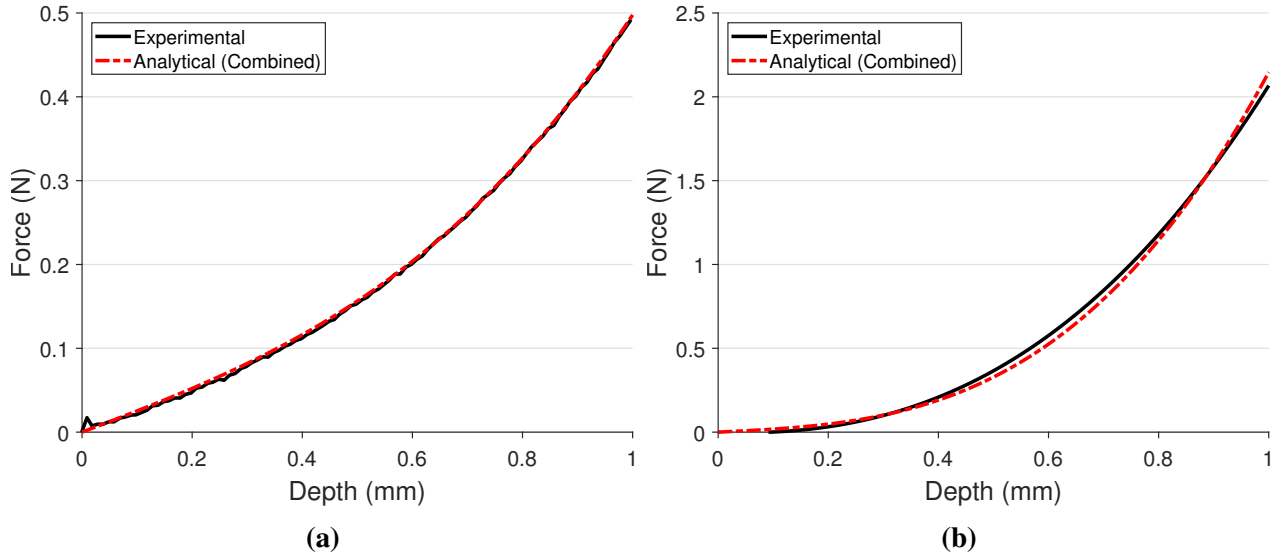


**Figure 3.13.** Comparison between the membrane's experimental performance from dry testing and the analytical response for the (a) contact membrane and (b) reciprocating membrane.

### 3.5.3 Kinesthetic Response

To test the device's ability to generate a range of stiffnesses, a kinesthetic testing procedure was developed and performed. First, the actuator's resistive force was first measured in its off-state. Then, a high frequency square wave was applied between 0 V and peak amplitudes of 1, 2, 3 and 4 kV to emulate a pulsating DC signal. These results are presented below in Figure 3.14. As evidenced in the figure, as the magnitude of the input voltage and pressed depth increase, the resistive force increases. The off-state resistive force was measured to be about 2.5 N at maximum depth. The maximum force produced was about 3.6 N under 4 kV load. While the force profiles formed by voltages up to 3 kV had similar curvature, the force curve produced under the 4 kV input included a steep increase and decrease in force during the 0.3-0.5 mm range of the stroke. This can be attributed to a build-up of pre-yield ER fluids in the activation region, followed by a rapid yielding event.

To further examine the results from a haptic perspective, the just-noticeable difference (JND) must be calculated. The JND is a measure of the amount that the kinesthetic force must change for a difference to be perceived by a human. For kinesthetic feedback, force rate ( $Q_v$ ) is the metric for JND and is defined as the ratio of the difference between the maximum and minimum force ( $P_v$ ) to the maximum force ( $L_v$ ) at said depth:

$$Q_v = \frac{P_v}{L_v} \quad (3.31)$$

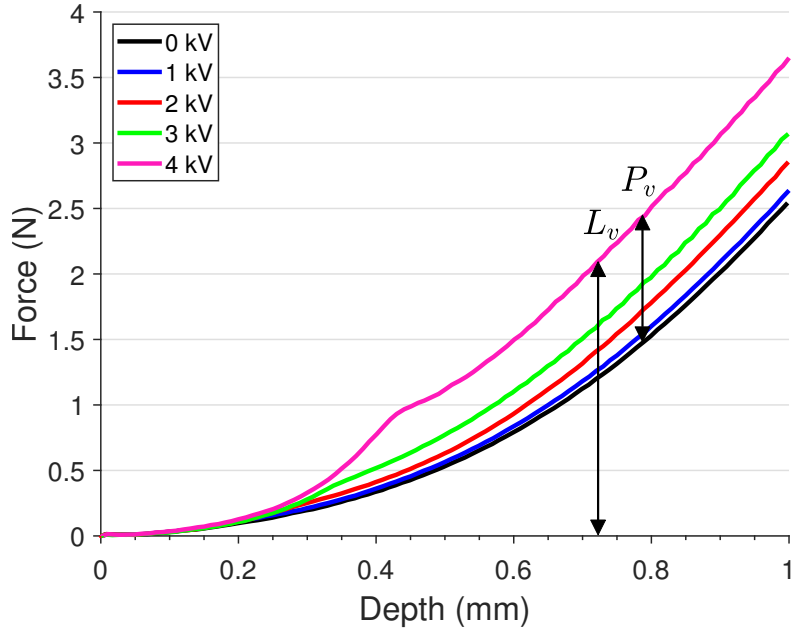


**Figure 3.14.** Experimental kinesthetic results: force (N) vs. depth (mm).

Figure 3.15 is produced by applying the force rate equation across all depths in the actuator's stroke. From an indentation depth of 0 to 0.2 mm, some volatility occurs due to the relatively low magnitudes of the forces, as evidenced in Figure 3.14. From 0.2 mm to 1 mm, the force rates stabilize and follow a similar trend; force rate increases with respect to applied voltage. Beyond 0.2 mm, the lowest force rate is about 3.5% at a depth of 1 mm under 1 kV applied signal. The greatest force rate of 58.5% is produced at maximum voltage and occurs at about 0.4 mm indentation depth, corresponding to the yielding event observed in Figure 3.14. The threshold for which humans can consistently detect changes in force is about 7-10% for forces between 0.5 and 200 N [23]. As indicated by the plot in Figure 3.15, the proposed actuator is capable of conveying distinct kinesthetic feedback above the threshold for supplied voltages greater than 1 kV.

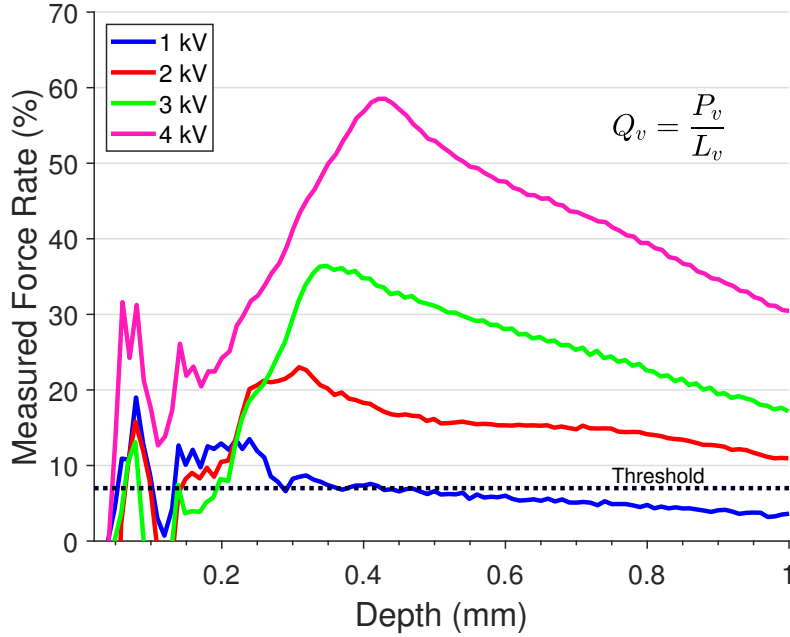


**Figure 3.15.** Experimental kinesthetic results: force rate (%) vs. indentation depth (mm).

### 3.5.4 Tactile Response

To demonstrate a vibrotactile response, sinusoidal voltage inputs were applied between 0 V and peak amplitudes of 1, 2, 3, and 4 kV and at frequencies of 1, 3, 5, and 10 Hz. Figure 3.16 presents the resultant force profiles for each set of frequencies and voltages. As seen in the figure, the force feedback responds harmonically when subjected to sinusoidal voltages. As the magnitude of the applied voltage increases, the amplitude of vibration increases as well. These results show that the actuator can convey controllable resistive forces over a range of frequencies. Therefore, the actuator is capable of communicating vibrotactile feedback.

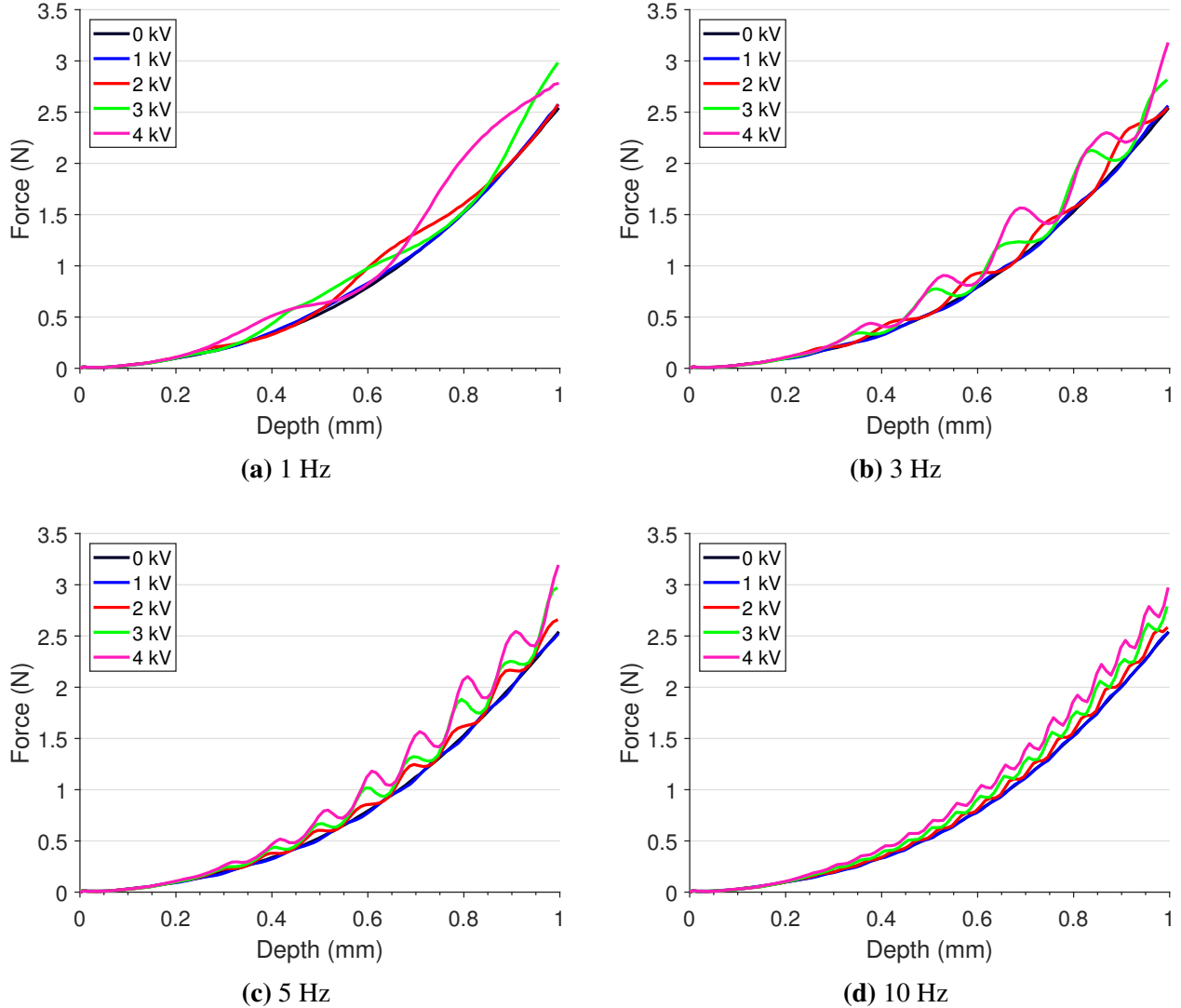


**Figure 3.16.** Experimental tactile results: force rate vs. indentation depth (mm).

### 3.6 Numerical vs. Experimental Performance

Figure 3.17 compares the kinesthetic experimental results (opaque, smooth lines) from subsection 3.5.3 with the results of the kinesthetic numerical simulation (transparent, dashed lines). The simulation and experimental results agree acceptably well. The off-state, 1 kV, 2 kV, and 3 kV results overlay with little variance. The 4 kV responses differ due to the yielding event observed in experiments not being included in the model. However, the maximum force produced by the actuator was accurately determined by the mathematical model.

To further demonstrate the proposed numerical model's accuracy, its response to a sinusoidal excitation is compared to the measured response for 3 Hz, shown in Figure 3.18. Specifically, emphasis is placed on the force due to the fluid by removing the elastic membrane's response. As

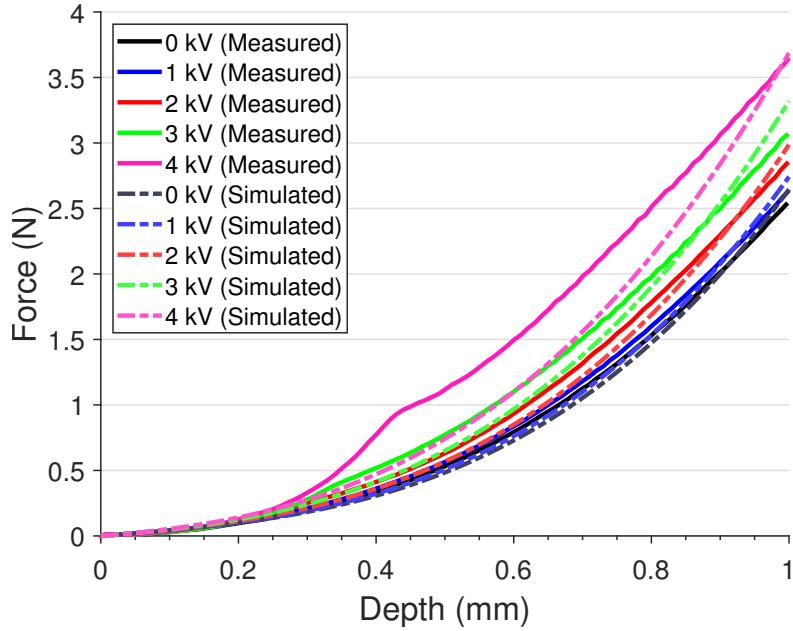


**Figure 3.17.** Comparison of kinesthetic feedback between the measured and simulated forces.

shown in the figure, the predicted vibrotactile response is similar to that measured in experiments. It is seen that at indentation depths greater than 0.7 mm, the model tends to overestimate the force due to the ER effect.

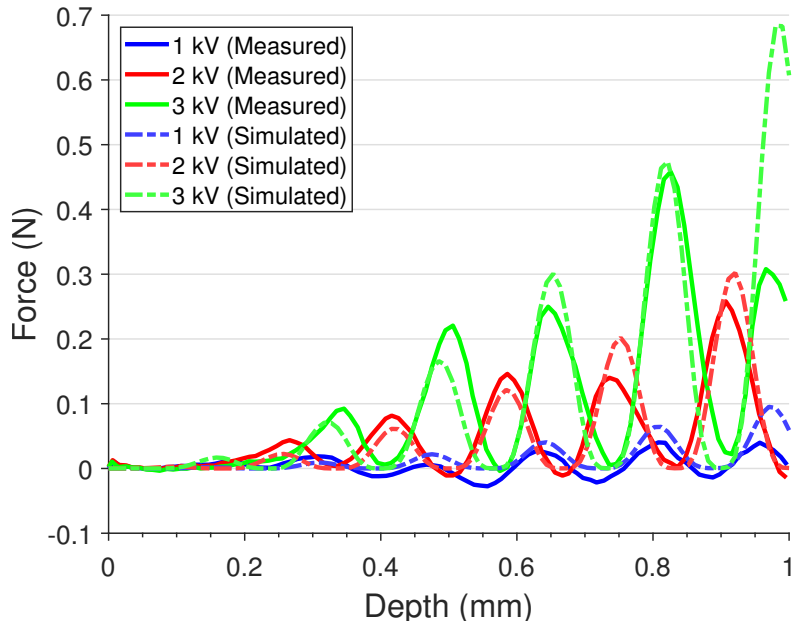


**Figure 3.18.** Comparison of vibrotactile feedback strictly due to the ER effect at 3 Hz excitation between the measured force and simulated force.

## 3.7 Parametric Studies

To improve the design and functionality of future actuators, parametric analysis is of great importance. Having modeled and experimentally validated the system's behavior, the influence of geometric, material, and electrical parameters can be closely examined. Since this study pertains to the design of a physical device operating in a small force range, a dimensional approach is taken. Baseline parameters have been provided in Table 3.2 and hold true unless explicitly varied. Previous findings indicate that for viscous damping to increase, the primary strategies are to increase electrode length or decrease the electrode gap [82]. In the case of designing a mobile actuator, the device size must be minimized while maintaining haptic resolution. In the following subsections, the effect of varying the gap distance between electrodes and outer electrode radius are presented and discussed.

### 3.7.1 Effect of Gap Size

The electrode gap holds significant influence on the pressure drop, evidenced by the cubic inverse and inverse relationships with viscous flow and yield, respectively, as shown in Equation 3.20. It is expected that a decrease in the electrode gap will increase the actuator's force output. Electrode gap  $d$  was varied across 0.5, 0.666, 0.833, 1, 1.25, 2 mm for the off-state and active response (1 kV, 2 kV, 3 kV, 4 kV). The resulting force-depth curves are presented in Figure 3.19.

It can be seen that reducing the electrode gap leads to greater forces, especially at high voltages. However, it should be noted the model does not capture the risk to safety associated with concentrating the electric field. Increasing the electrode gap above 1 mm results in less distinguishable forces with respect to voltage. It is likely best to maintain a 1 mm electrode gap.

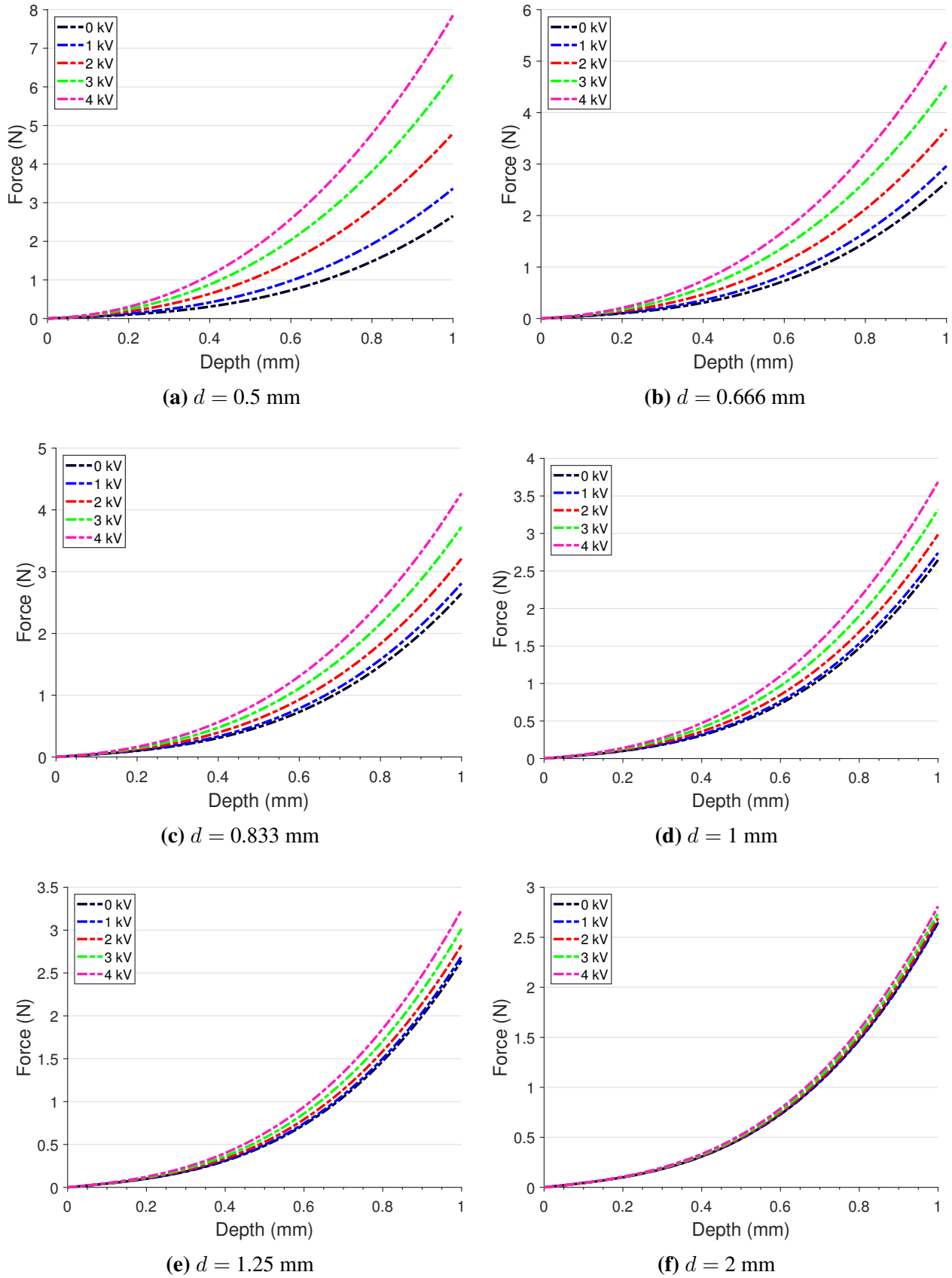


**Figure 3.19.** Effect of flow mode electrode gap size  $d$  on actuator response.

### 3.7.2 Effect of Electrode Length

Similarly, the electrode length affects the force produced by the actuator, as indicated in Equation 3.20. Particularly, the dominant term  $\Delta P_{yield}$  is proportional to the difference between the electrode pair's outer and inner radius. Since the inner electrode radius is constrained by the size of the contact region, the outer electrode radius is varied to determine its influence on actuator performance. It is expected that the output force will increase with the outer electrode radius. Outer electrode radius  $r_0$  was varied from 11→16 mm in 1 mm increments for the off-state and active response (1 kV, 2 kV, 3 kV, 4 kV). The resulting force-displacement profiles are presented in Figure 3.20.

As predicted, increasing the electrode area leads to a larger valve and a greater range of forces. When designing an ERF actuator, it is desirable to maximize the electrode area to potentially generate a wide band of forces. However, electrode size must be balanced with the device's form factor for mobile applications.

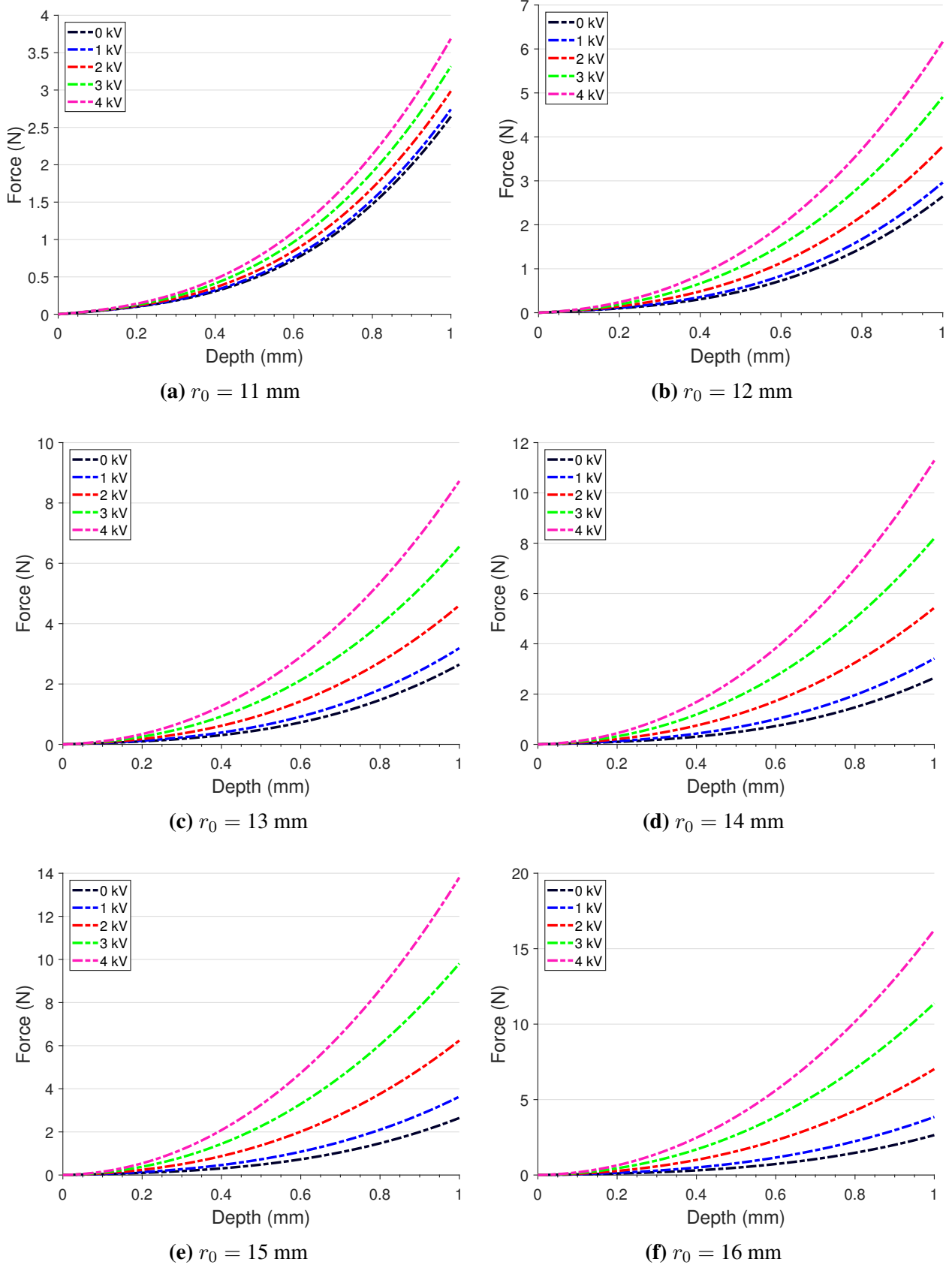


**Figure 3.20.** Effect of outer flow mode electrode radius  $r_0$  on actuator response.

### 3.8 Conclusion and Discussion

This chapter has presented the design, modeling and experimental evaluation of a new design for a compact haptic actuator based on the tunable yield stress of electrorheological fluids. The device was designed to operate in flow mode to minimize actuator thickness and mechanical complexity. An analytical model for the actuator's force output was derived and implemented into a numerical simulation. A prototype actuator was fabricated and tested experimentally using a dynamic mechanical analyzer. The resistive force generated by the actuator along its stroke was measured for both kinesthetic and vibrotactile input voltage signals. The experimental results verified those produced by the model. The results indicated that the actuator's resistive force increases with increased indentation depth and applied voltage. Furthermore, the measured results demonstrate distinct force rates that may be perceived by humans as a range of kinesthetic sensations in application. The vibrotactile performance of the actuator showed significant improvement over previous iterations [11]. Thus, the actuator was confirmed capable of conveying a range of haptic feedback sensations. Future design may incorporate a wider range of forces, as well, and is elaborated upon in the following chapter.

# 4 | Haptic Actuator based on ER Fluid in Mixed Mode

This chapter builds upon the design outlined in the previous chapter with a goal of increasing the actuator's range of force outputs without sacrifice to its small form factor. To do so, a modification to the PCB-based flow mode device is proposed by introducing a "squeeze mode" region into the design. The following sections detail the design and fabrication, mathematical modeling and experimental testing of an ERF haptic actuator with combined squeeze and flow operational modes, referred to as the mixed mode or squeeze-flow design.

## 4.1 Proposed Actuator Design

To increase the range of forces produced by the actuator, an additional mode of fluid flow (squeeze mode) is introduced to the design. The following subsection details the working principle and methodology behind the proposed design. Then, the new structural design components are introduced. Lastly, the fabricated prototype squeeze-flow mixed-mode haptic actuator is presented.

### 4.1.1 Working Principles

Figure 4.1 portrays the cross-section and working principle of the mixed squeeze-flow haptic actuator. The squeeze-flow design features the same flow mode principle as the previous design. However, in contrast with previous design, the squeeze-flow actuator contains an additional grounded "spring" electrode below the contact surface and a larger charged electrode surface. When a user presses upon the membrane contact surface, the additional grounded is displaced vertically, resulting in a change in the local electrode gap distance. Upon relieving pressure at the contact surface, the actuator returns to its pre-pressed state through the elastic nature of the electrode spring and membrane. The fluid between the spring and charged electrodes is compressed or squeezed, hence the naming convention "squeeze mode." Similar to flow mode, the magnitude of the force produced by ER fluid in squeeze mode is dependent upon the strength of the applied field. However, the forces produced in squeeze mode are considered to be less dependent upon the change in apparent viscosity. Instead, the force produced corresponds to the mechanical behavior of the columnar chains formed by the particles in the electrode gap under compressive load [61, 83]. Typically, smart fluids in squeeze mode have been used in high force, low displacement applications [60]. Introducing squeeze mode to the actuator's design may therefore widen the range of forces produced

by the actuator.

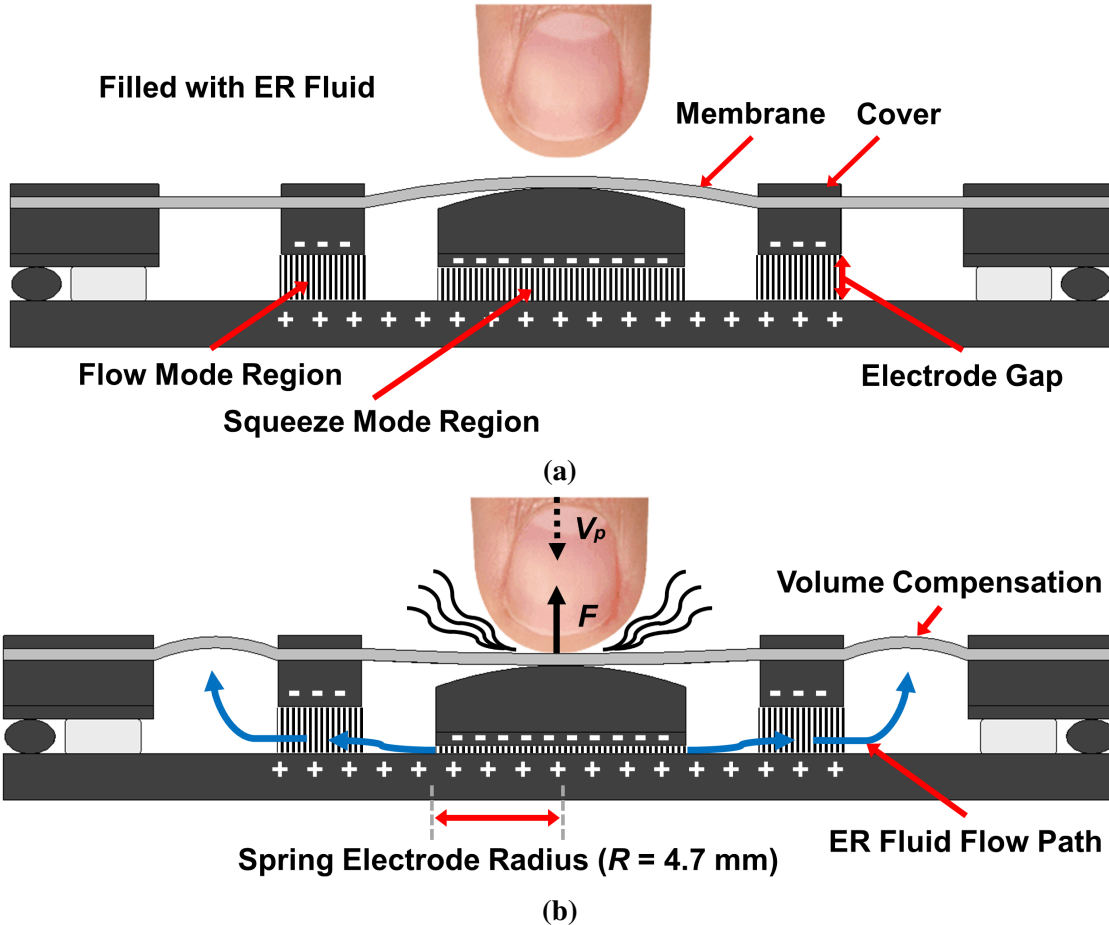


**Figure 4.1.** Working principle of the proposed squeeze-flow haptic actuator **(a)** before contact and **(b)** mid-contact.

### 4.1.2 Structural Design

Figure 4.2 shows a schematic illustration of the squeeze-flow actuator, including the newly designed spring electrode for squeeze mode operation. The spring electrode is manufactured from stainless steel (SUS 304) and the center disc can deform elastically for small displacements. A plastic knob is attached to the top of the spring electrode and contact membrane to couple their displacements. The spring electrode shares a common ground with the GND PCB. To prevent binding between the spring electrode and HV PCB due to electrostatic forces, a small (1 mm diameter, 0.35 mm thick) silicone film is adhered to the spring electrode. The HV PCB has been modified to have a larger, disc-type electrode to add control in the squeeze mode region. The assembled device has a diameter of 42 mm and a thickness of 6.0 mm.

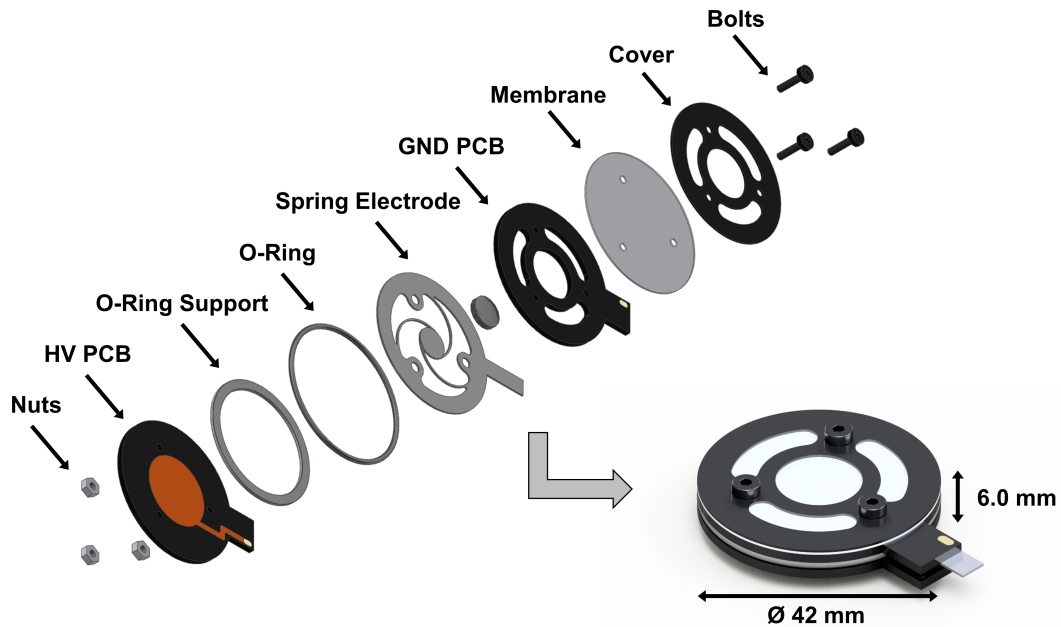


**Figure 4.2.** Exploded view drawing of the squeeze-flow haptic actuator.

### 4.1.3 Fabrication

Figure 4.3 presents the device's fabricated individual components and assembled squeeze-flow prototype actuator. Identical to the previous iteration, the device functions as a button-type actuator and is composed of two electrode PCBs, a plastic spacer and O-ring, a thin-film silicone and VHB membrane, and a plastic cover. The HV electrode radius measures 11 mm.

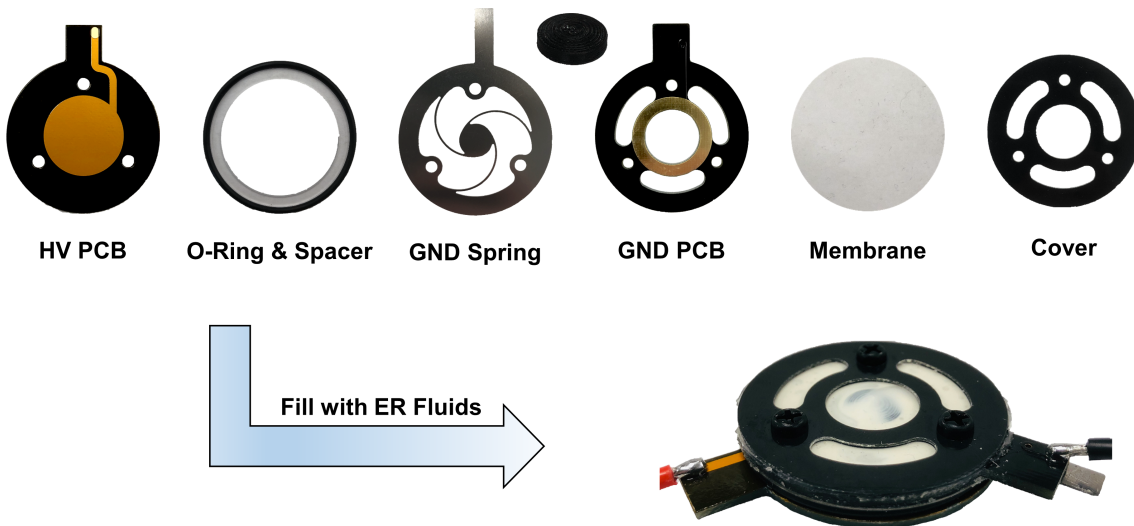


**Figure 4.3.** Fabricated components and mixed mode actuator assembly.

Additionally, a compliant, spring electrode is placed inside the device. Figure 4.4 shows the

fabricated spring electrode. As shown, three thin beams arranged in a spiral pattern allow for small displacements (into the page) at the electrode's center. The radius of the deformable electrode measures 4.7 mm. The thickness of the spring electrode was determined through prototyping and experimentation. A 0.2 mm and a 0.3 mm thick electrode adhered together was determined to offer sufficient returning force without overpowering the resistive force produced by the ER effect.

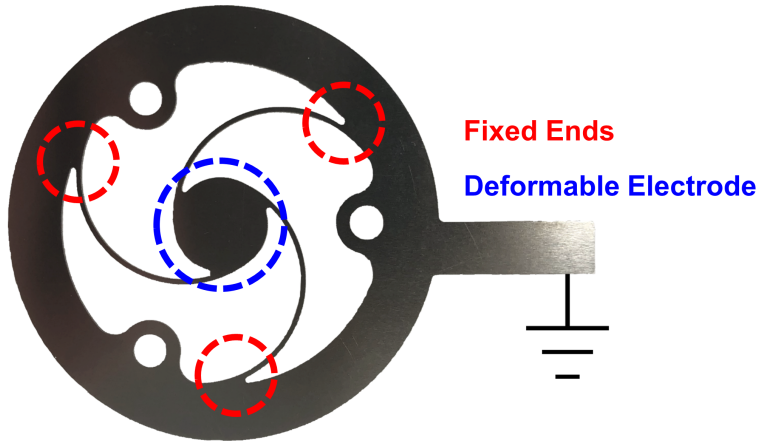


**Figure 4.4.** Fabricated deformable spring electrode.

Again, the maximum indentation depth of the actuator is 1 mm. The device was designed and manufactured with a goal of minimizing thickness to convey a wide range of kinesthetic and tactile sensations in a compact form factor. Introducing a squeeze mode to the actuator comes at little sacrifice to device thickness while adding functionality.

## 4.2 Mathematical Modeling of ERF in Combined Squeeze and Flow Mode

**Actuator Modeling Overview:** To understand the squeeze-flow actuator's behavior from a generalizable standpoint, a mathematical model was developed based on the device's fundamental behavior. The current section presents the literature's established squeeze mode model for relating input voltage to output force. Section 4.3 then presents a numerical approach to modeling the spring electrode's deformation. Next, the squeeze mode model and results from the spring deformation model are implemented into the existing numerical model described in the previous chapter. After validating the model through experiments, parametric studies are performed to investigate the effect of actuator geometry on force output, discussed in Section 4.8.

A schematic of the actuator in squeeze mode is presented in Figure 4.5. The lower PCB electrode is stationary, while the upper, spring electrode deforms vertically under the user's press.

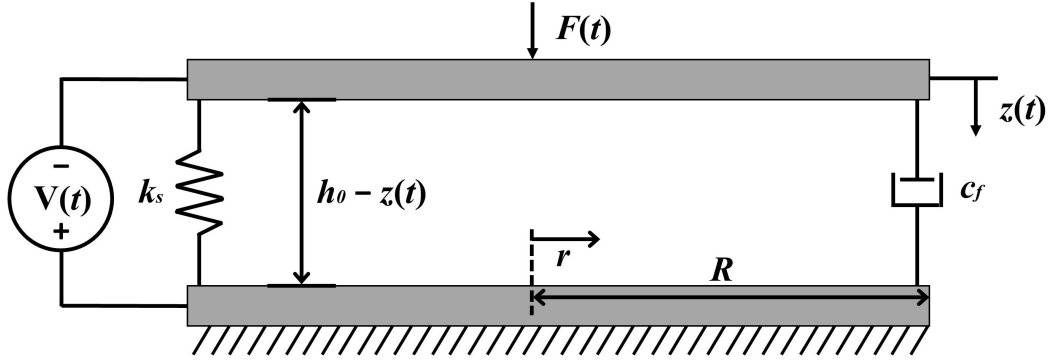


**Figure 4.5.** Conventional squeeze mode model schematic.

The force produced by the squeeze mode assembly is represented by [58, 84]:

$$F(t) = k_s z(t) + c_f(t) \dot{z}(t) + F_{\text{ER squeeze}}(t) \quad (4.1)$$

where

$$\begin{aligned} c_f(t) &= \frac{3}{2} \frac{\pi \mu R^4}{(h_0 - z(t))^3} \\ F_{\text{ER squeeze}}(t) &= \frac{4}{3} \frac{\pi R^3}{h_0 - z(t)} \tau_y(E) \operatorname{sgn}(\dot{z}(t)) \end{aligned} \quad (4.2)$$

In this formulation,  $k_s$  is the stiffness constant of the spring,  $c_f(t)$  is the damping coefficient of ER fluid due to viscous flow in the off-state,  $F_{\text{ER}}(t)$  is the damping force associated with the fluid's active response,  $z(t)$  is the displacement of the user's finger,  $h_0$  is the initial electrode gap, and  $R$  is the radius of the spring electrode. Alternative to the conventional squeeze mode model, a derivation from the Navier-Stokes equation may be performed as well.

Therefore, including the flow mode and relevant membrane models defined in Equation 3.20 and subsections 3.3.1-3.3.2, the total force produced by the mixed squeeze-flow actuator felt by the user may be written:

$$F_{\text{total}} = F_{\text{squeeze}} + F_{\text{flow}} + c_{\text{squeeze}} \dot{z} + c_{\text{flow}} \dot{z} + k_s z + F_{\text{Membrane}} \quad (4.3)$$

### 4.3 Model of Electrode Spring Displacement

A finite element method (FEM) model was developed to determine the force produced by the electrode spring with respect to its displacement. Figure 4.6 shows the modeling process. First, the geometry was drawn in Autodesk Inventor™ software. The model was assigned Stainless Steel (SUS 304) as its material to match the fabricated electrode. Mechanical properties of SUS 304 are

provided below in Table 4.1. The fixed ends and compressed sections of the electrode spring were prescribed fixed boundary conditions. An applied force was assigned perpendicular to the center of the deformable electrode.

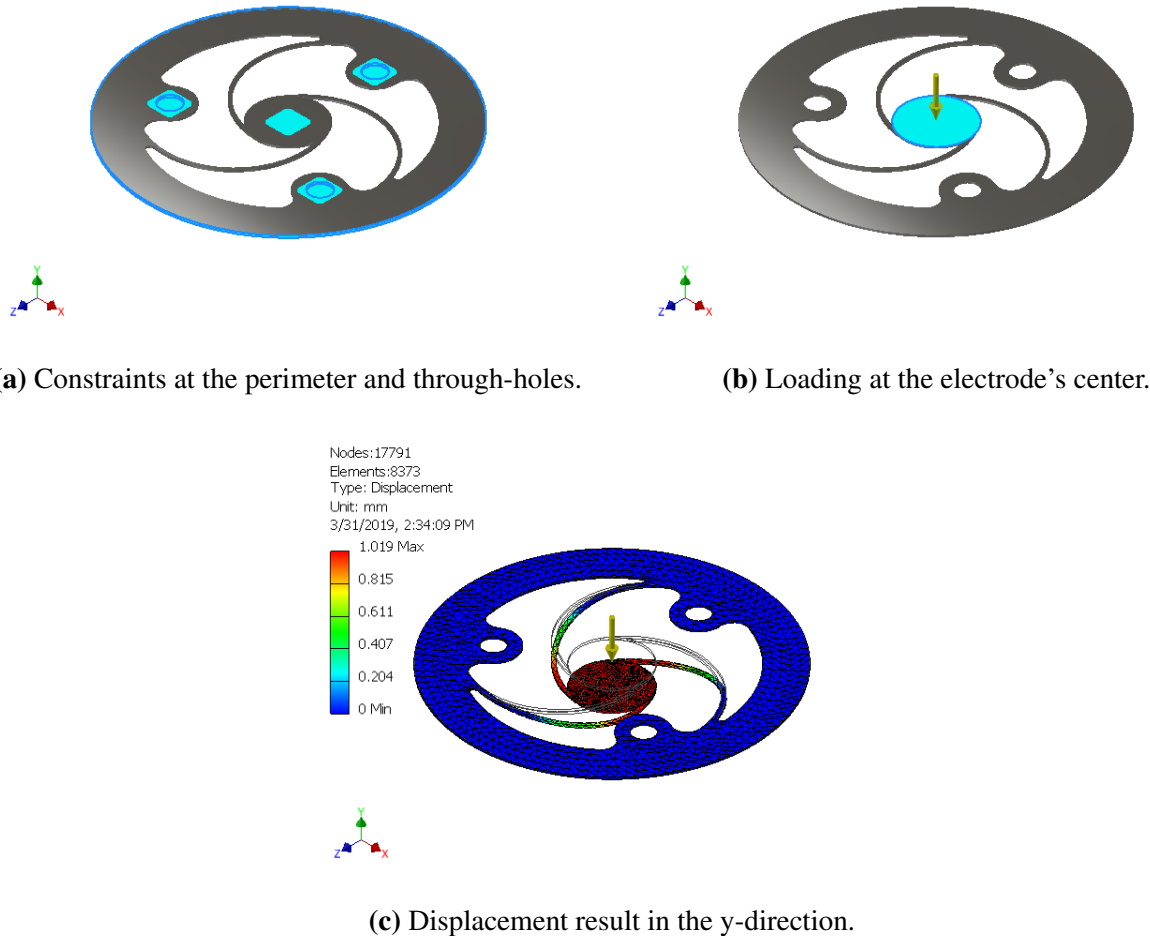


**Figure 4.6.** Steps in the finite element analysis process for characterizing the electrode spring.

**Table 4.1.** Mechanical properties of Type 304 Stainless Steel (SUS 304) used in the FEM simulation.

Parameter	Value
Behavior	Isotropic
Young's Modulus	193 GPa
Poisson's Ratio	0.29
Shear Modulus	86 GPa
Density	8000 kg/m <sup>3</sup>

To determine the force-displacement relation for the spring electrode, a parametric range of applied force was prescribed and the resultant displacement was found (Inventor™ software doesn't allow for the inverse method). This was performed for spring electrode thicknesses of both 2 and 3 mm and the data points were fit with linear curves, as shown in Figure 4.7. To estimate the force produced by the fabricated electrode spring (0.2 mm and 0.3 mm thick electrodes adhered together), the individual 0.2 mm and 0.3 mm thick curves were added together.

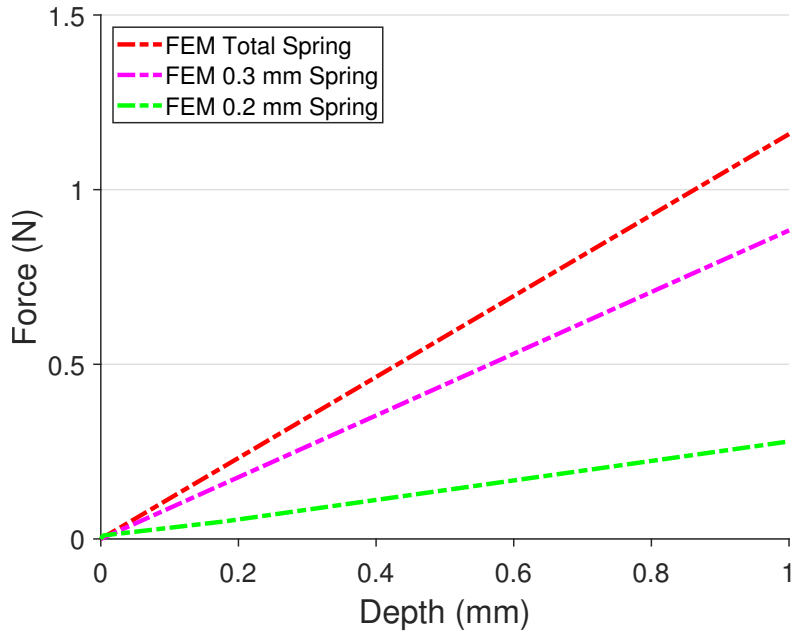


**Figure 4.7.** FEM results for the force produced by displacing the spring electrode.

## 4.4 Numerical Evaluation of the Proposed Actuator

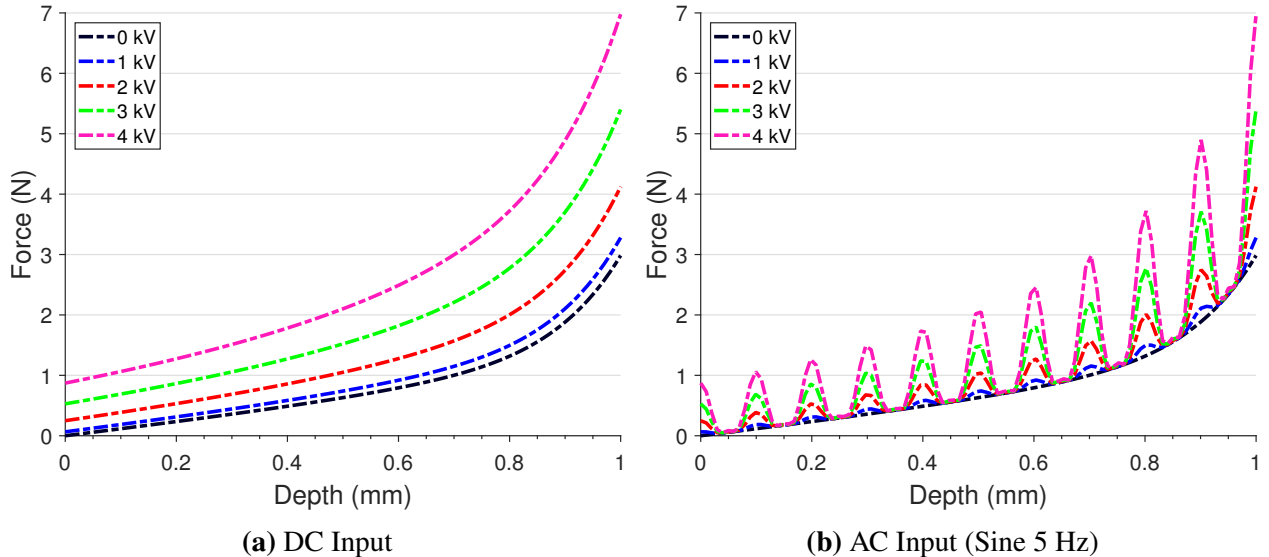
To simulate the squeeze-flow actuator's behavior, the MATLAB® script described in subsection 3.4 for a flow mode actuator is modified to incorporate both the squeeze and flow mode forces as a function of depth, as described by Equation 4.3. The model uses the same field-stress coupling model as described in the previous chapter. Critical model parameters are provided in Table 3.3 and below in Table 4.2. Values used reflect the properties of the fabricated prototype actuator and the experimental test setup.

The computational model is supplied with voltage and frequency inputs and generates force-displacement plots, similar to experimental testing. Figure 4.8a shows the force curves produced by the model when subjected to DC voltage inputs of 0, 1, 2, 3, and 4 kV. As shown, when no power is supplied to the simulated actuator, the greatest force produced is about 3 N at maximum indentation. When the maximum voltage is applied (4 kV DC), the greatest output force increases

**Table 4.2.** Parameters of the squeeze-flow simulation.

Parameter	Symbol	Value
Static Electrode Gap (Flow)	$d$	1.8 mm
Electrode Radius (Inner)	$r_0$	7.5 mm
Electrode Radius (Outer)	$r_1$	11 mm
Initial Electrode Gap (Squeeze)	$h_0$	1.3 mm
Electrode Radius (Spring)	$R$	4.7 mm
Viscosity of GER Fluid	$\mu$	0.060 Pa·s
Radius of Indenter	$r_p$	5.9 mm
Velocity of Indentation	$V_p$	1 mm/s
Final Indentation Depth	$\delta_f$	1 mm

to nearly 7 N. This result is notable compared to results demonstrated in the previous chapter. Figure 4.8b shows the predicted force profiles when the model is supplied with the same voltage range, pulsated at a sinusoidal frequency of 5 Hz. As shown, as the magnitude of the voltage increases, the amplitude of vibration increases as expected. The vibrotactile profiles are bounded by the off-state and corresponding applied voltage curves shown in the kinesthetic result. The simulation results imply that the actuator is capable of providing both kinesthetic and vibrotactile feedback.

**Figure 4.8.** Results of the simulated mixed mode actuator: force (N) vs. depth (mm) along its stroke.

## 4.5 Experimental Evaluation

This section details the experimental methods used to evaluate the fabricated squeeze-flow haptic actuator. The goal of these experimental studies is to characterize the device's ability to produce a distinct range of kinesthetic and vibrotactile feedbacks. Experimental methods include compression testing with a dynamic mechanical analyzer (DMA) and vibration testing using an accelerometer.

### 4.5.1 Experimental Setup

Again, compression testing was performed upon the fabricated actuator using a DMA (RSA3, TA Instruments). The applied electric field was controlled by a function generator and voltage amplifier (Trek Model 609E-6, 1000 V/V), as shown in Figure 4.9. This setup allowed for accurate force vs. depth plots up to 10 Hz frequency. However, the Pacinian corpuscles are sensitive to vibrations up to 300 Hz [15, 17]. To measure the actuator's performance at higher frequencies within the limits of human perception, an accelerometer (PCB Piezotronics 356A22) and a vibration isolating rubber were fitted between the DMA indenter and the contact surface of the device (see Figure 4.9). With the addition of the accelerometer, the setup can accurately characterize the high frequency vibration response of the actuator. A data acquisition board (NI cDAQ9172) connected to a host computer is used to collect and process the data from the accelerometer. A 5 kHz sampling frequency was used, which is sufficiently greater than the frequencies rendered by the device to avoid aliasing. The performance was evaluated under different input voltage and frequency conditions using an indenter similar in size to a human finger. An indentation rate of 1 mm/s was used for all testing.

### 4.5.2 Electrode Spring Response

Dry testing was performed with an assembled actuator without adding fluid into the device to compare the force-depth response with the electrode spring model described in subsection 4.3. Figure 4.10 plots the FEM simulation and experimental electrode spring responses. The nearly linear experimental response indicates that the actuator's dry response is mostly dependent upon the electrode spring's linear elastic behavior. The FEM electrode spring model is demonstrated to be sufficiently accurate when plotted against the experimental response.

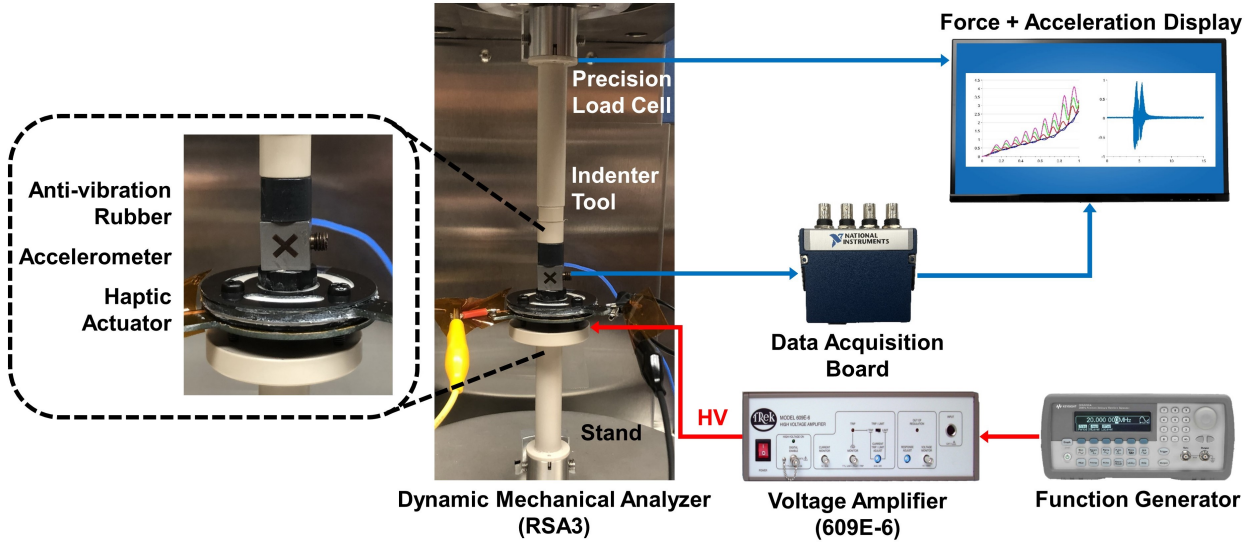


**Figure 4.9.** Experimental setup for evaluating the mixed mode device's kinesthetic and vibrotactile feedback.

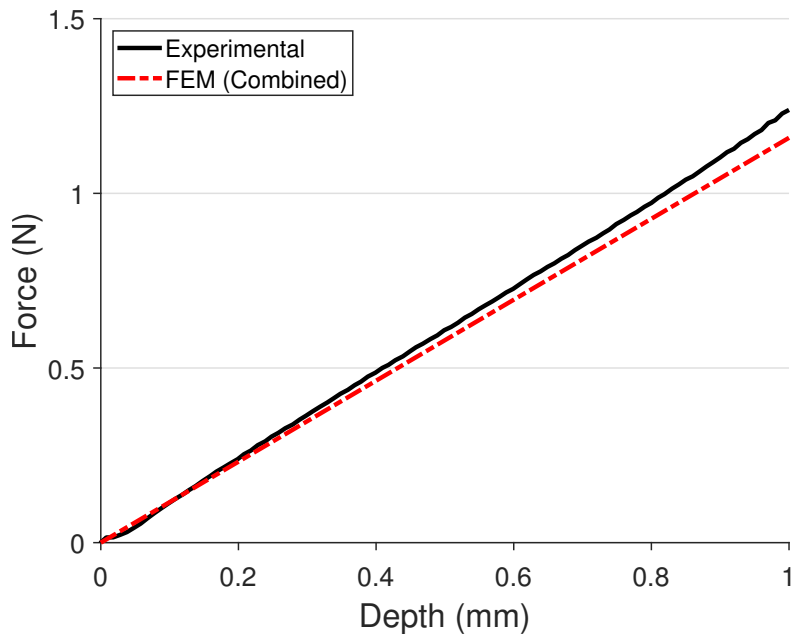


**Figure 4.10.** Comparison between the electrode spring's experimental response from dry testing and the FEM simulation response for the superposed 0.2 mm and 0.3 mm spring responses.

### 4.5.3 Kinesthetic Response

To test the device's ability to generate a wide range of stiffnesses, the kinesthetic testing procedure described in subsection 3.5.3 is followed. The actuator's passive force was measured without applied voltage. The actuator was then subjected to high frequency (100 Hz) square waves to emulate a pulsating DC signal. The actuator's active response was measured for applied voltages

between 0 V and peak amplitudes of 1, 2, 3 and 4 kV. These results are presented below in Figure 4.11. As seen in the figure, the resistive force produced increases with the applied voltage and pressed depth. The passive resistive force was measured to be about 2.7 N at maximum depth. The maximum force produced was about 6.2 N under 4 kV load. Compared to higher voltages, the effect of applying 1 kV on the force profile is minimal. Of additional note, within the first 0.1 mm of the stroke, the profiles follow a similar curve independent of applied voltage. It should be noted that future trials indicated that this may have been caused due to a gap where fluid had filled between the contact membrane and the plastic spacer on the squeeze electrode. To eliminate this lag, careful attention should be given during assembly to ensuring a secure bond between the plastic spacer and acrylic tape. This prevents fluid from causing separation and ensures a coupled response.

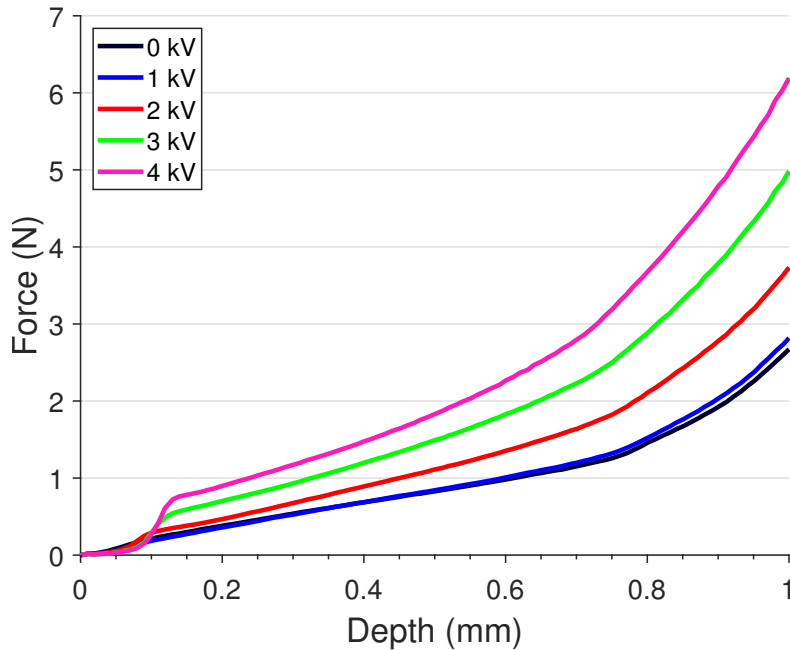


**Figure 4.11.** Experimental mixed mode kinesthetic results: force (N) vs. depth (mm).

To further examine the kinesthetic results from a haptic perspective, the just-noticeable difference (JND) must be calculated, as described in subsection 3.5.3 and Equation 3.31. Figure 4.12 is produced by applying the force rate equation across all depths in the actuator's stroke. Beyond a depth of 0.1 mm, the force rates stabilize and follow a similar flat profile. The greatest force rate is produced by the 4 kV curve, which averages about 57%. The lowest force rate is generated by the 1 kV signal, which fell below the off-state curve for the first 0.35 mm of the stroke, resulting in a negative force rate. As previously noted, the threshold for which humans can consistently detect changes in force is about 7-10% for forces between 0.5 and 200 N [23]. As indicated by the plot in Figure 4.12, the proposed actuator is capable of conveying distinct and consistent kinesthetic

feedback above the threshold for supplied voltages greater than 1 kV.

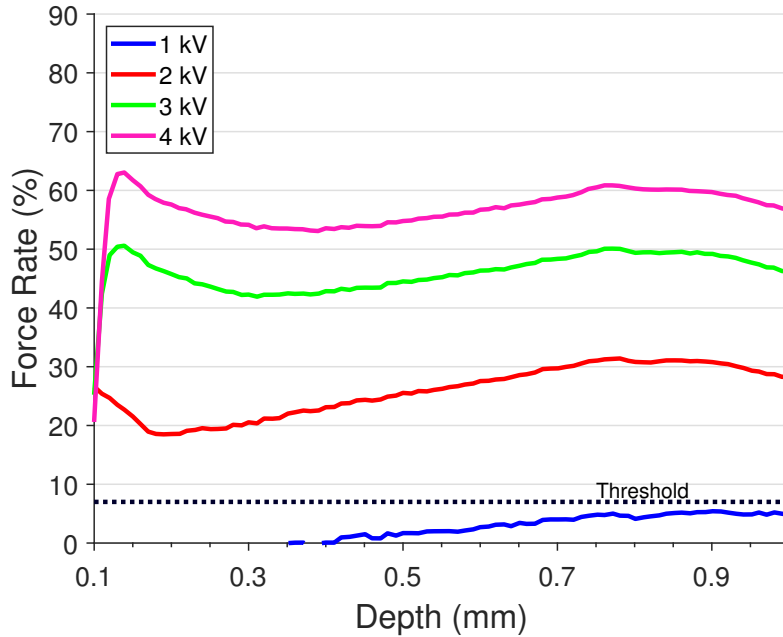


**Figure 4.12.** Experimental mixed mode kinesthetic results: force rate (%) vs. indentation depth (mm).

#### 4.5.4 Tactile Response

To measure the actuator's vibrotactile response, sinusoidal voltage inputs were applied between 0 V and peak amplitudes of 1, 2, 3, and 4 kV. The vibrational response is evaluated using two techniques: (1) the force-depth data from the DMA is analyzed for low frequency responses and (2) the accelerometer data is processed for high frequency responses.

##### Low Frequency

To measure the actuator's low frequency vibrotactile response, sinusoidal waveforms at frequencies of 1, 3, 5, and 10 Hz are supplied. Figure 4.13 presents the resultant force profiles for each set of frequencies and voltages. As seen in the figure, the force feedback responds harmonically when subjected to sinusoidal voltages. As the magnitude of the applied voltage increases, the amplitude of vibration increases as well. These results show that the actuator can convey controllable resistive forces over a range of low frequencies. Therefore, the actuator is capable of communicating low-frequency vibrotactile feedback.

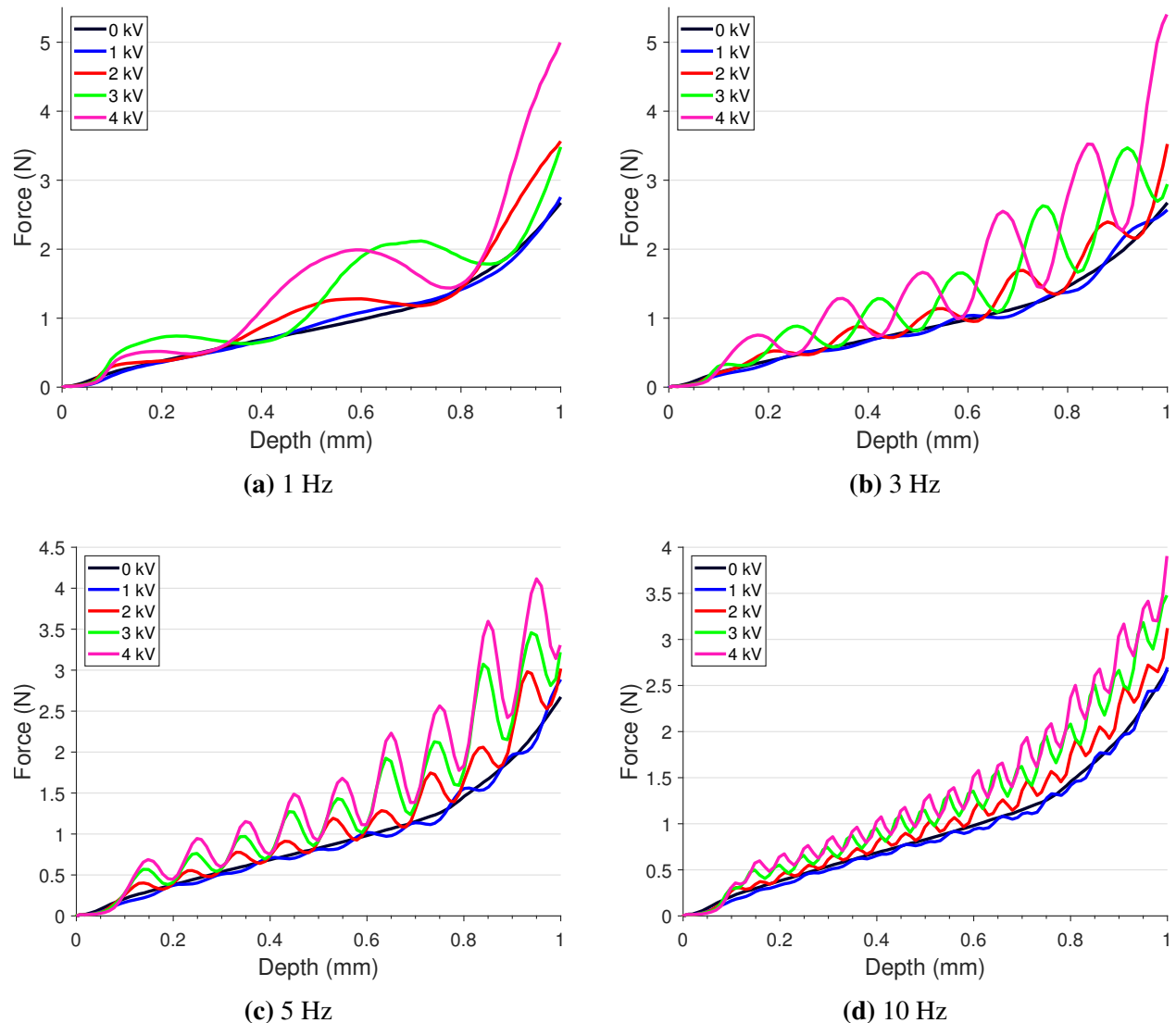


**Figure 4.13.** Experimental tactile results: force rate vs. indentation depth (mm).

## **High Frequency**

As discussed in Chapter 2, humans are capable of sensing tactile signals at much higher frequencies than just the set tested in the previous subsubsection. For a complete evaluation of the device's tactile performance, this subsection examines performance at high frequencies up to 300 Hz, corresponding to the sensitivity of the Pacinian corpuscle. To measure the actuator's high frequency vibrotactile response, 4 kV square waveforms at frequencies of 50, 100, 200, and 300 Hz are supplied and data is collected from the accelerometer (2 kHz sampling rate). Data analysis is performed in both the time and frequency domains via Fast Fourier Transform (FFT). Figure 4.14 was produced by a 50 Hz square wave and shows the typical time domain response for the system. As shown, prior to pressing, the magnitude of acceleration is close to 0 g. During the 1 mm press, the magnitude of acceleration increases. At 1 mm depth, the indenter reverses its direction and fluid flow pauses, indicated in the plot by a moment of 0 g acceleration. When the indenter releases its indentation, fluid flow resumes and the amplitude of vibration increases until the indenter stops at its initial position.

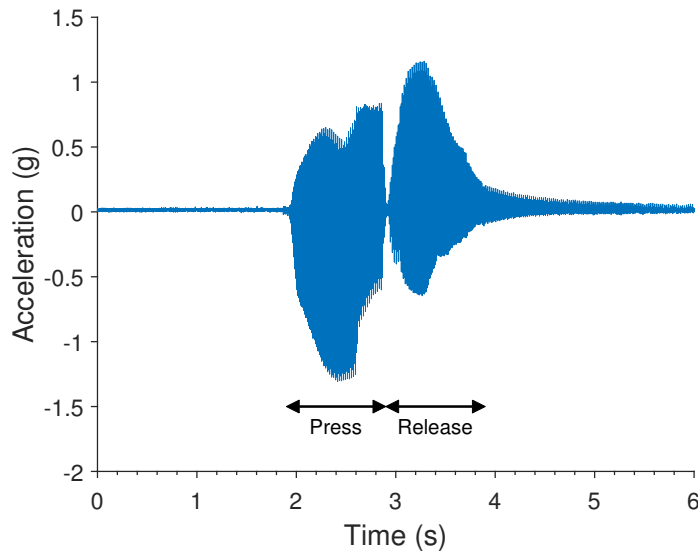


**Figure 4.14.** Acceleration (g) vs. Time (s) for 50 Hz square wave input.

Figures 4.15-4.18 present the measured acceleration response for the frequencies tested (50, 100, 200, and 300 Hz). As shown in the time domain plot for 50 Hz, the maximum vibration intensity generated by the actuator is 1.3 g. As the applied frequency increases, the maximum intensity decreases. At 300 Hz, the maximum intensity is found to be 0.7 g. Psychophysical studies reveal that the human acceleration detection threshold is  $0.01 \text{ g}$  ( $0.1 \text{ ms}^{-2}$ ) for frequencies between 0 and 500 Hz [85]. As evidenced by the acceleration-time plots, the device is capable of generating vibration intensities significantly greater than the 0.01 g threshold. Therefore, the actuator can convey distinct tactile sensations at high frequencies.

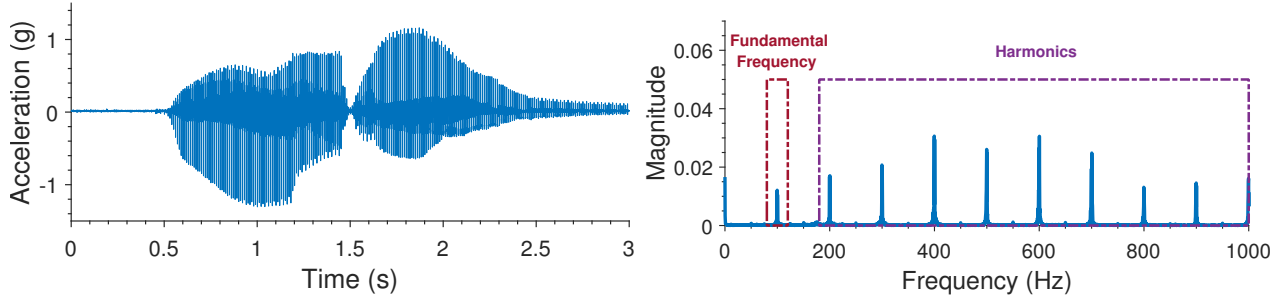


**Figure 4.15.** Measured acceleration signals and FFT spectrum under 50 Hz square wave input.

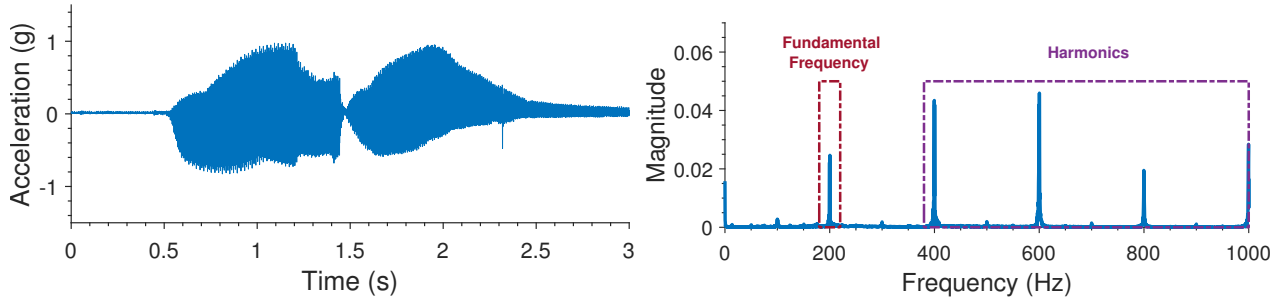


**Figure 4.16.** Measured acceleration signals and FFT spectrum under 100 Hz square wave input.

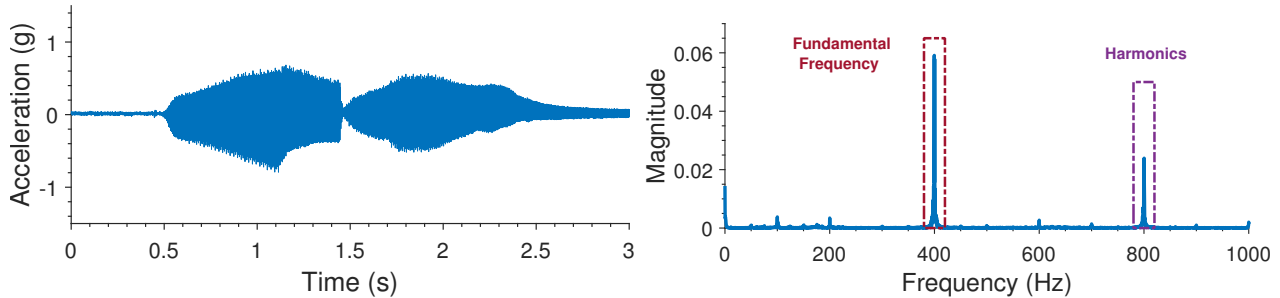


**Figure 4.17.** Measured acceleration signals and FFT spectrum under 200 Hz square wave input.

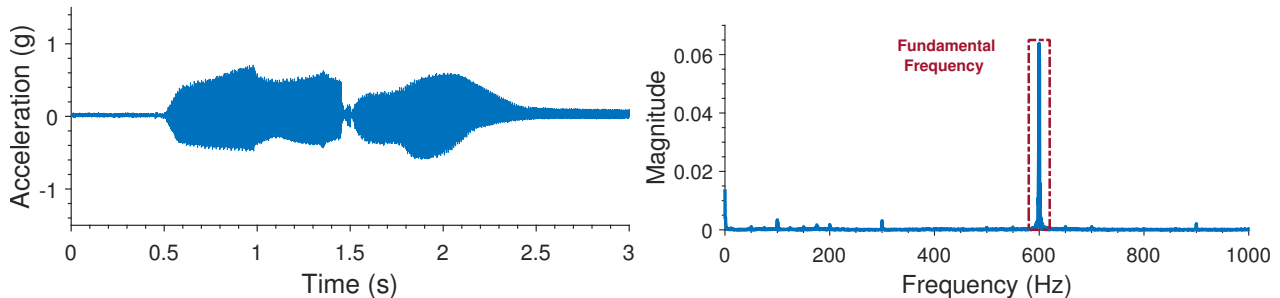


**Figure 4.18.** Measured acceleration signals and FFT spectrum under 300 Hz square wave input.

Figures 4.15-4.18 also present the single-sided amplitude spectrum  $|P_1(f)|$  produced by FFT of the corresponding time domain data. It should be noted that the fundamental frequency found by the FFT analysis is twice that of the applied square wave frequency. As shown, for 50 Hz

square wave input, the fundamental frequency is 100 Hz. This trend holds for the trials at other frequencies. Harmonics, integer multiples of the fundamental frequency, are seen in the FFT spectrums, as well. The FFT results validate that the actuator can accurately return vibrotactile feedbacks at the assigned frequency of the voltage input.

To summarize the high frequency analysis, the measured results demonstrate that the ERF haptic actuator can trigger the Pacinian corpuscle. The actuator is capable of conveying vibrotactile sensations to users in a wide frequency range, taking advantage of the full spectrum of human tactile sensing.

## 4.6 Numerical vs. Experimental Performance

The results predicted by the simulation (transparent, dashed lines) are compared to the results obtained experimentally (solid, opaque lines) in Figure 4.19. As shown, the two methods agree to an acceptable extent. The model predicts non-zero starting force, which is not physically realizable in experiments; however, the experimental results do rise close to the modeled forces at about 0.1 mm. After 0.1 mm, the curves are closely aligned with little variance. In the case of 4 kV applied, the model slightly overestimates the force output.

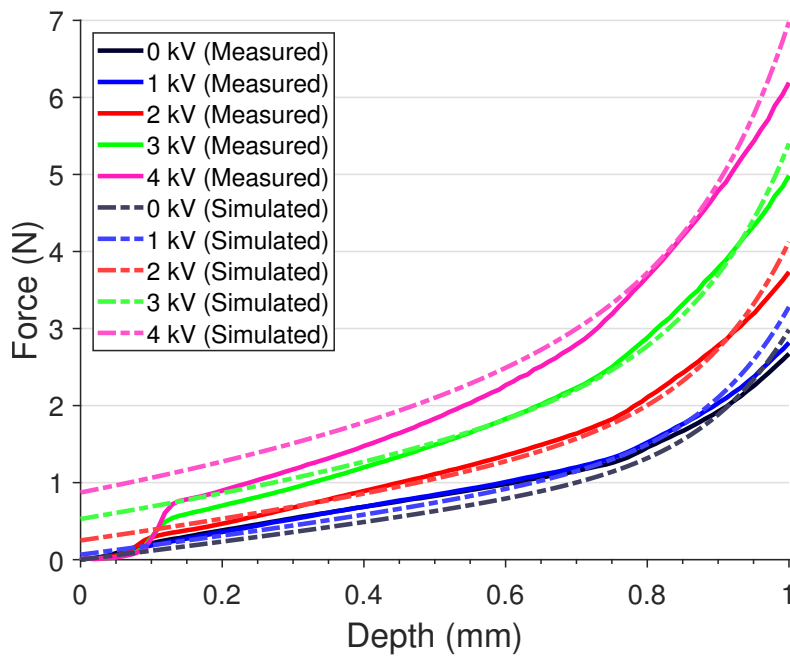


**Figure 4.19.** Comparison of kinesthetic feedback between the measured and simulated force for mixed mode.

Similarly, the modeled vibrotactile response may be compared to the experimental vibrotactile results. Figure 4.20 shows the measured and simulated results under application of a 3 Hz sine

wave. As shown, the curves show reasonable correspondence for 1, 2, 3 and 4 kV.

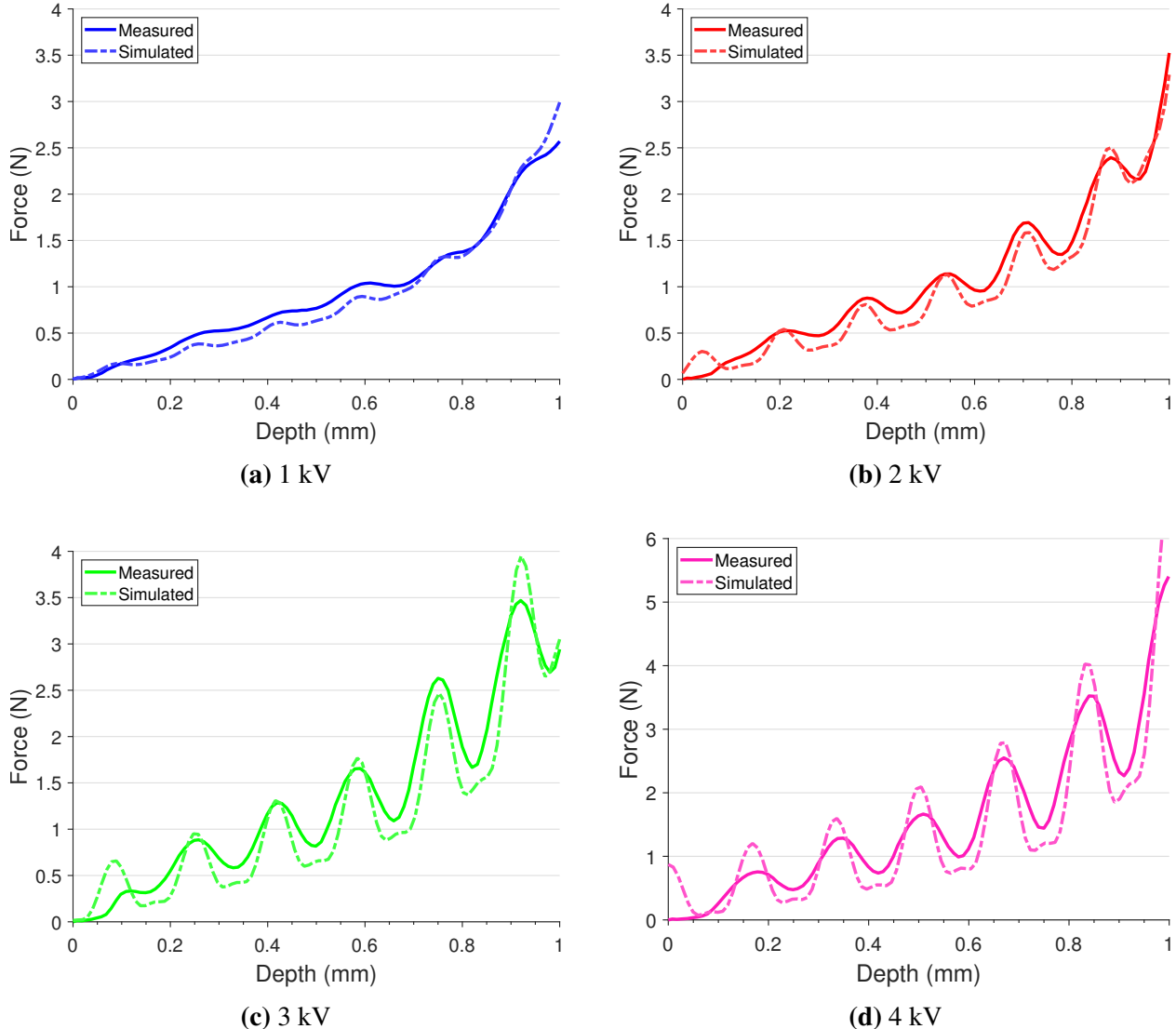


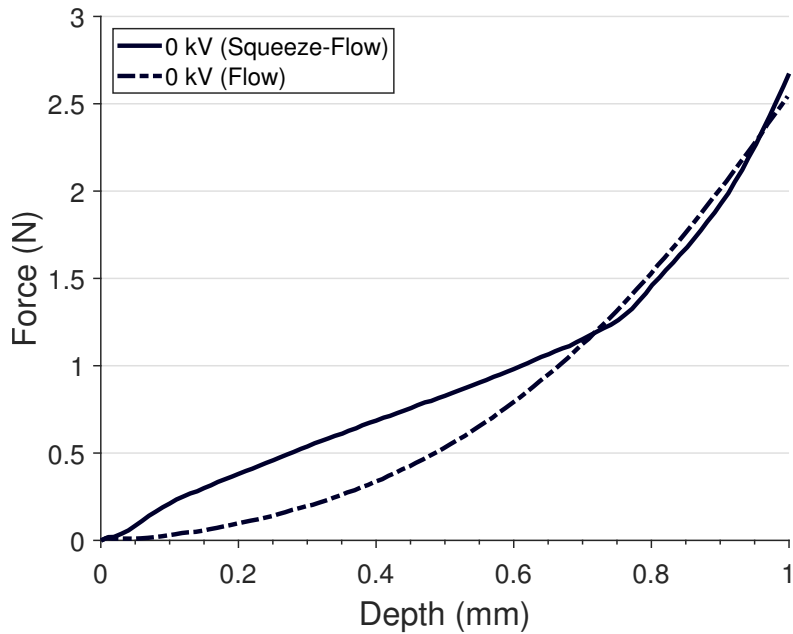
**Figure 4.20.** Comparison of vibrotactile feedback between the measured and simulated force for mixed mode.

## 4.7 Performance Comparison: Squeeze-Flow vs. Pure Flow

This chapter introduced a design modification to implement squeeze mode into the flow mode actuator introduced in Chapter 3. This design change was motivated by a potential widening of the actuator's force bandwidth. This section compares the results between the pure flow mode and mixed squeeze-flow actuators.

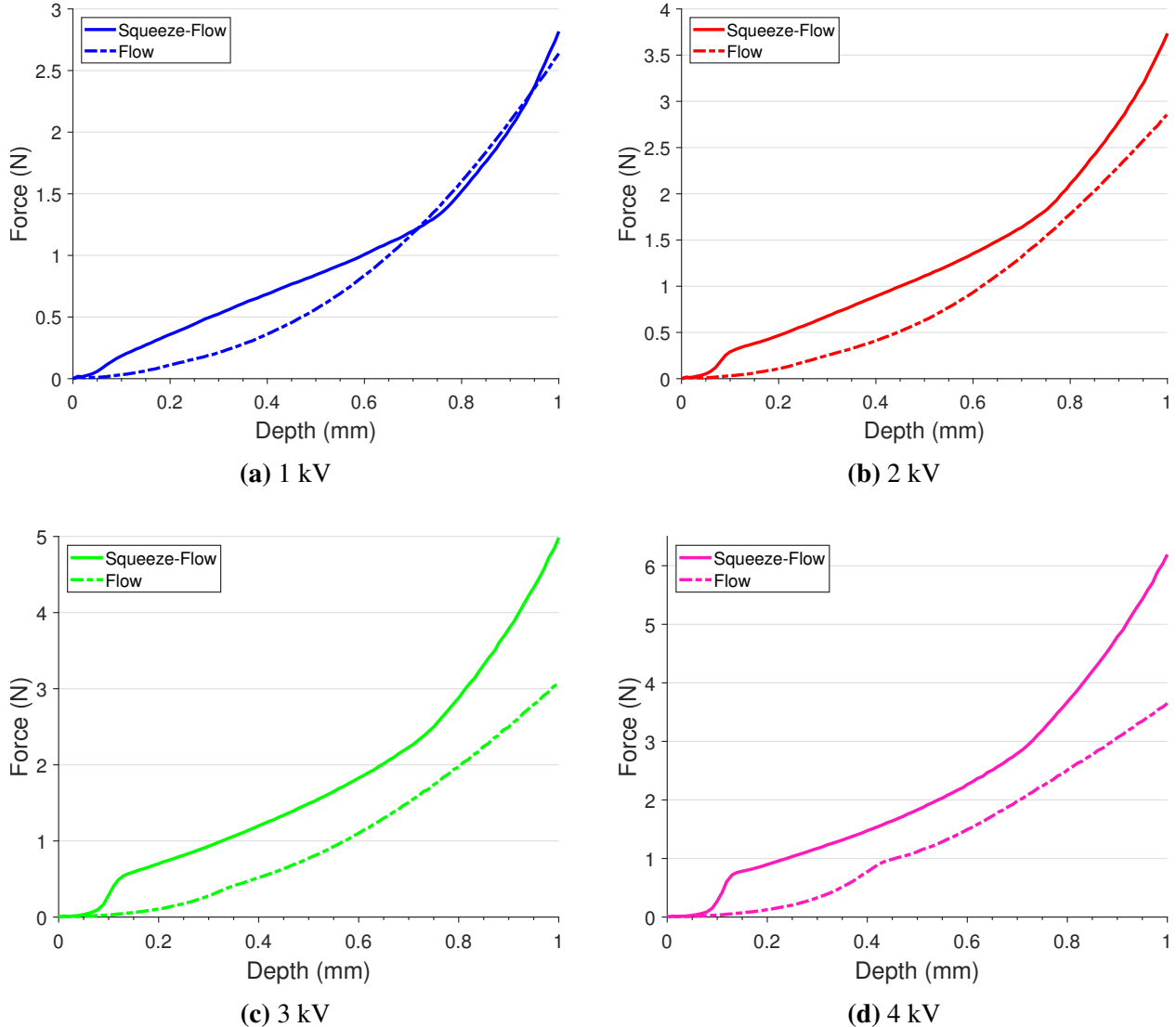
### 4.7.1 Kinesthetic Comparisons

Figure 4.21 compares the off-state results between the flow and squeeze-flow actuators. As shown, the two actuators perform similarly, allowing for some general comparisons to be drawn. The squeeze mode actuator produces greater forces early in the stroke ( $< 0.2$  mm) due to the added spring force.



**Figure 4.21.** Comparison of the off-state response for the squeeze flow and pure flow mode actuator.

Figure 4.22 compares the kinesthetic performance of the two devices. Additionally, the squeeze-flow force profiles become more distinct with respect to voltage earlier in the stroke than the flow mode profiles. This equates to better kinesthetic resolution throughout the entire stroke. The squeeze-flow design produces a wider force range ( $2.7 \rightarrow 6.2$  N) compared to the pure flow mode actuator ( $2.5 \rightarrow 3.6$  N). Ultimately, introducing a squeeze mode to the design leads to improved kinesthetic resolution and output.



**Figure 4.22.** Comparison of kinesthetic feedback among squeeze-flow and pure flow actuators under applied voltages.

### 4.7.2 Tactile Comparisons

Figure 4.23 compares the devices' response under a 5 Hz sine waveform for 1, 2, 3 and 4 kV. For all applied voltages, the amplitude of vibration is greatest for the squeeze-flow design. Therefore, the squeeze-flow device is capable of providing a wider range of magnitudes of vibration, making it more than the pure flow design.

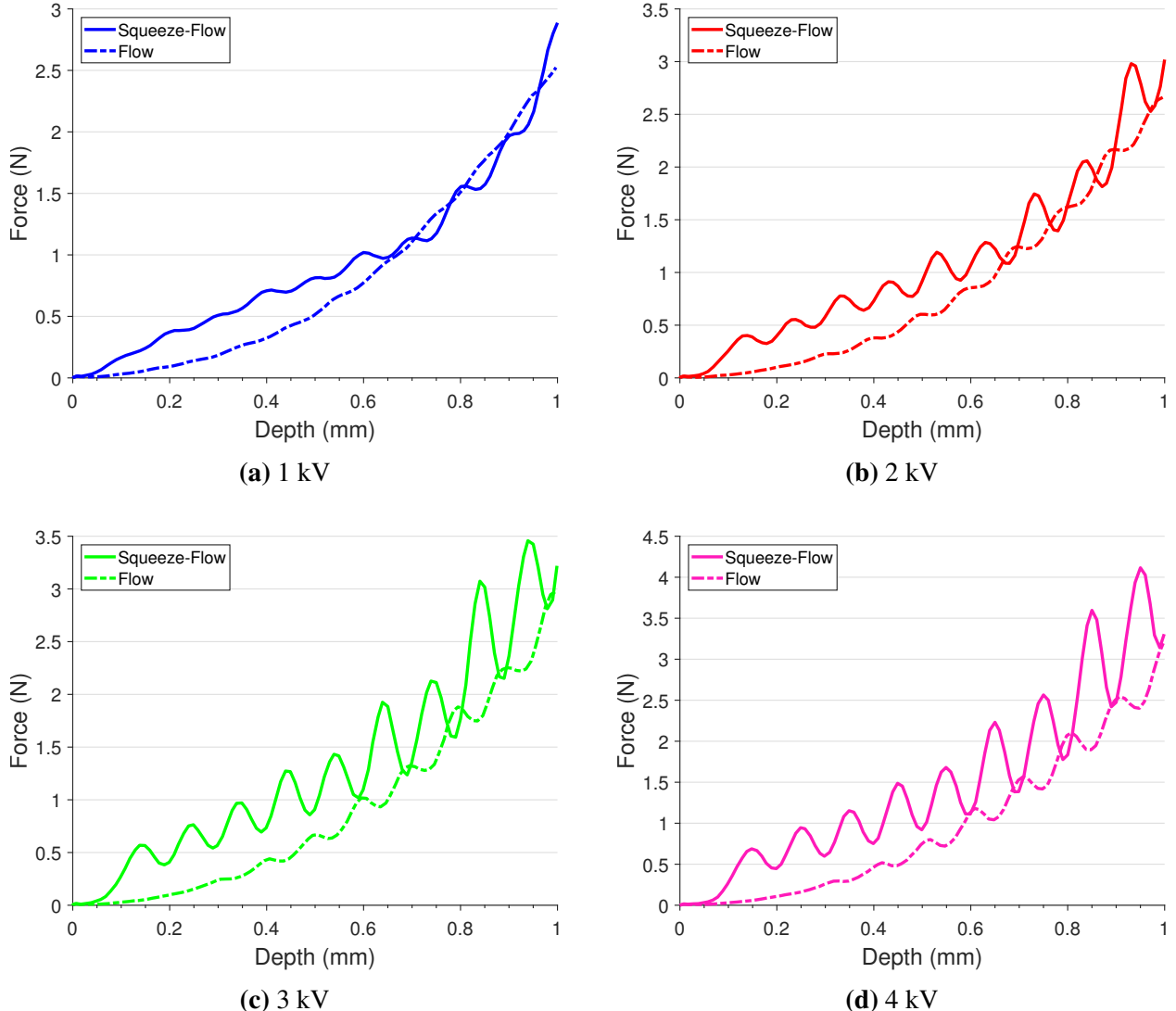


**Figure 4.23.** Comparison of vibrotactile feedback among squeeze-flow and pure flow actuators under applied voltages.

## 4.8 Parametric Study

As previously discussed, examining the critical design parameters of the actuator through parametric study can yield valuable insights toward future designs. Having validated the squeeze-flow model experimentally, this section performs a parametric sweep on the area of squeeze mode to determine its influence on force output. Baseline parameters, shown in Table 4.2, are held constant while the radius of the spring electrode is varied. As demonstrated in Equation 4.2, the spring electrode's radius has a cubic relationship with the force due to ER fluid in squeeze mode. Therefore, it is expected that increasing the spring electrode radius will greatly increase the force output. The spring electrode radius  $R$  was varied from 2, 4, 6 and 8 mm for both the off-state and active

response. Figure 4.24 shows the resultant force-depth curves.

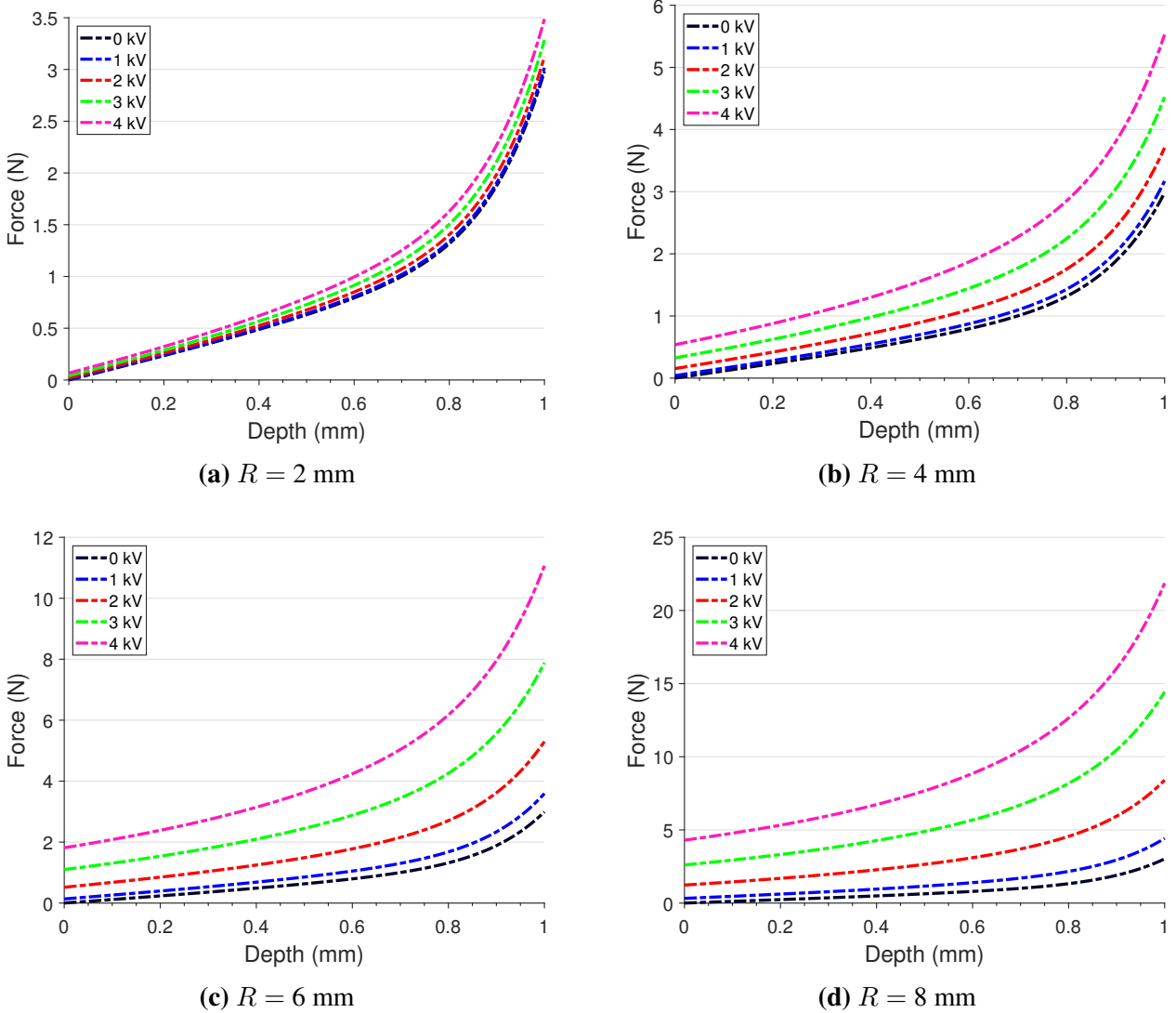


**Figure 4.24.** Effect of spring electrode radius  $R$  on actuator response.

As predicted, increasing the radius of the spring electrode resulted in much greater forces. With a radius of 8 mm, the model predicts nearly 22 N produced at maximum indentation depth. Future designs should look to increase the area of the spring electrode, while maintaining a small form factor for engaging the fingertips.

## 4.9 Conclusions and Discussion

This chapter has presented the design, modeling and testing of a compact and compliant electrorheological actuator for haptic feedback. The device was based on previous work outlined

in the previous chapter with modifications to incorporate a region of squeeze mode operation. Modifications entailed retrofitting a deformable electrode spring, resulting in compression of fluid between electrodes. Implementing squeeze mode came at little cost to the device's mechanical complexity and form factor. A mathematical model for the actuator's force output was described and developed into a computational model. An electrode spring was fabricated and assembled within a prototype squeeze-flow actuator. Experimental testing was performed using a dynamic mechanical analyzer fitted with an accelerometer and data acquisition system for high frequency analysis. The resistive force produced by the device along its stroke was measured for both kinesthetic (DC) and vibrotactile (AC sine waveform) input voltage signals. The experimental results validated those produced by the model. The results demonstrated that the squeeze-flow actuator is capable of providing a wide range of forces and magnitudes of vibration. The squeeze-flow device generates more sensations at finer resolution than the previous pure flow mode design. In fact, squeeze mode was found to be the dominant mode of producing force. Future design may center around a spring-electrode, squeeze mode design and eliminate the nonlinear membrane mechanics altogether. Instead, contact may be made directly with the spring if it is coated in a highly resistive material, such as polytetrafluoroethylene (PTFE). Removal of flow mode regions may also reduce the device's circumference, leading to better miniaturization. Further attention should be given to the geometry of the squeeze mode elements for further miniaturization (see [86]).

The results presented in this chapter affirm that future work could be built around the actuator. For instance, embedding a thin pressure sensor and feedback control to act as a haptic interface by rendering realistic sensations between a user and virtual environment may be realized. These concepts are elaborated upon in the following chapter.

# 5 | Combined Sensor and ER Fluid-based Actuator

This chapter examines applications of the prototyped ERF actuator. First, methods of displacement sensing are proposed and evaluated. The actuator and sensor are incorporated into a digital system where information can be exchanged between a user and computer. Applications are developed for this infrastructure and future conceptual designs are described.

## 5.1 Proposed Sensor Designs

Multiple displacement sensing techniques were designed, fabricated and experimentally tested. In this section, three design iterations are discussed and recommendations are made toward future sensing techniques.

### 5.1.1 Triple Point Pressure (TPP) Sensor

The first sensor tested featured a pressure sensitive resistive material and custom PCB that could be retrofitted to the existing actuators described in Chapters 3 and 4. The following subsections detail its design and experimental performance.

#### Design

Figure 5.1 shows the fabricated triple point pressure (TPP) sensing PCB. The PCB features three electrode regions corresponding to the volume compensation radial slots on the actuator. A pressure-sensitive resistive (PSR) film, with properties shown in Figure 5.2, is adhered to the sensing PCB, forming the triple point pressure sensor. The TPP sensor can be fitted into the flow and squeeze-flow actuators by placing it above the cover during the assembly process. When the contact surface is pressed, the fluid flows through the activation regions and into the volume compensation regions. The pressure in the volume compensation region is experienced by the pressure-sensitive film. By measuring the change in voltage across the sensing PCB, the finger's displacement may be monitored in real-time.

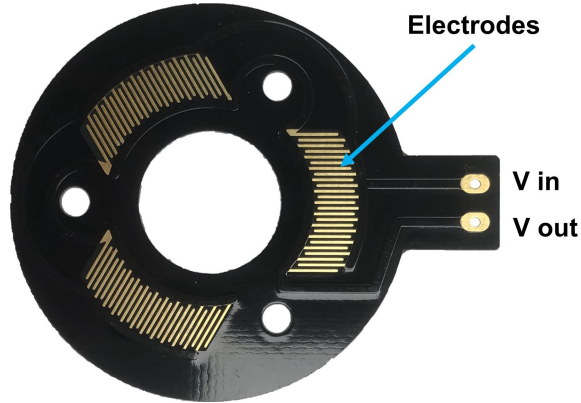


**Figure 5.1.** Fabricated triple point pressure sensor.

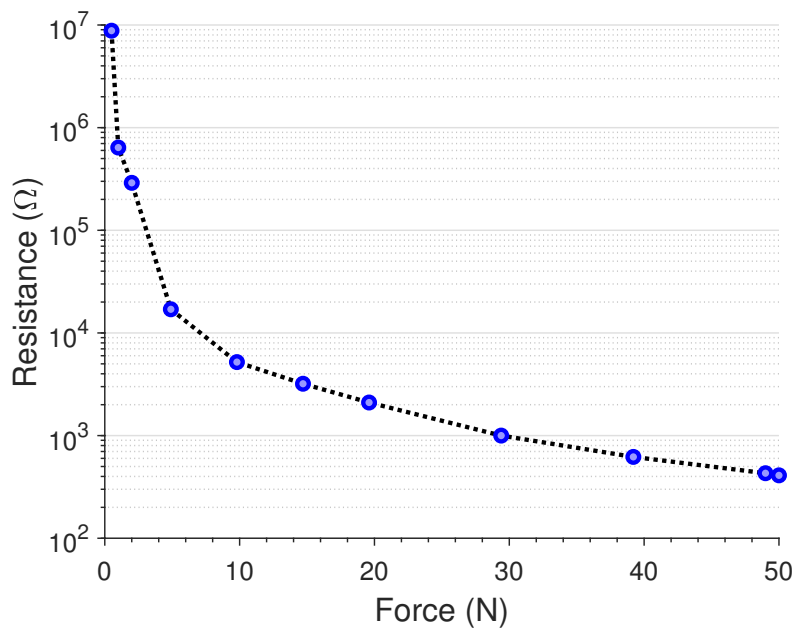


**Figure 5.2.** Resistance-Force coupling curve for pressure-sensitive resistive material.

## Performance Evaluation

A flow mode actuator fitted with the TPP sensor was tested using a DMA as described in Figure 3.12. The contact surface was deformed 2 mm at 1 mm/s. A pull-down resistor circuit, Arduino Uno and Processing were used to record the voltage across the TPP sensor during indentation.

The actuator and sensor response are shown together in Figure 5.3 for no voltage supplied to the actuator. The left axis shows the force (N) produced by the actuator, while the right axis shows the analog readings across the TPP sensor. The x-axis shows time (s) and both loading and unloading are presented. As shown, the sensor did not respond until about 0.8 s into the stroke; hence, a 2 mm depth was used to better capture the sensor's response. Between 1 and 3 s, the sensor reading

increased with the indentation and decreased with force removal. The maximum force produced by the actuator with the TPP sensor equipped was 14 N at 2 mm depth. This large increase may be attributed to both the increased depth compared to previous trials, as well as restricting the volume compensation chambers with the TPP sensor installed.

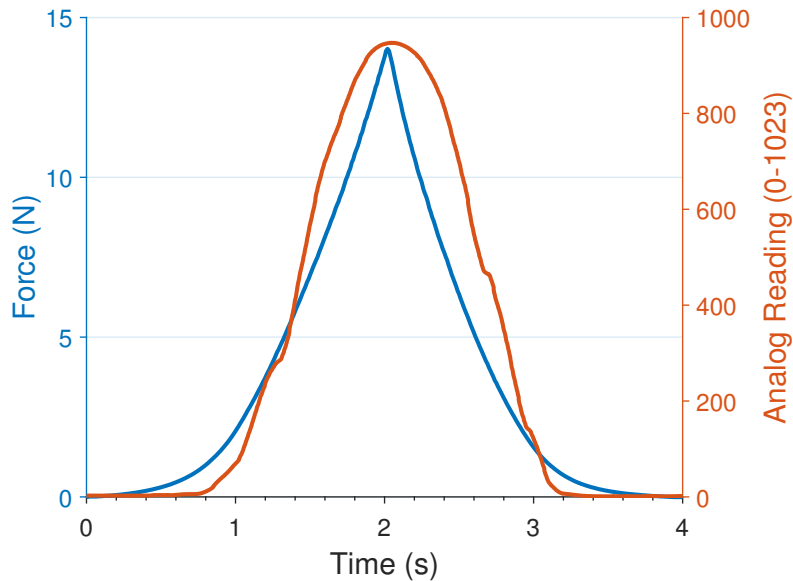


**Figure 5.3.** Off-state plot for the actuator and TPP sensor response under indentation.

The actuator's response under the standard applied voltage set and 50 Hz square waves is shown in Figure 5.4. As shown, the applied voltage has little effect on the actuator's resistive force. Therefore, introducing the TPP sensor to the flow mode actuator caused a saturation in the force output due to restricting the expansion of the volume compensation chambers.

## **Discussion**

Evidenced by Figure 5.3, the TPP sensor design was not able to capture small ( $< 0.8$  mm) deformations. Additionally, the TPP sensor saturated the force produced by the actuator. Therefore, the TPP sensor is ineffective for the application. To counter this, the sensor may be pre-stressed and allow for some unrestricted expansion of the volume compensation regions. These methods are carried into the following subsection.

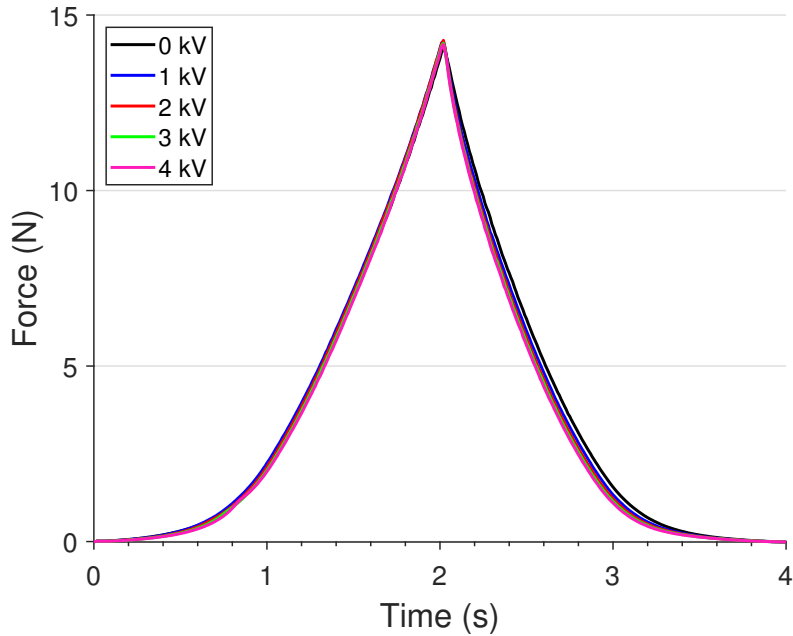


**Figure 5.4.** Force profiles with the TPP sensor installed.

### 5.1.2 Single Point Pressure (SPP) Sensor

The second sensor tested also utilized PSR film and a custom PCB with simple retrofitting. To mitigate saturation of the output force, two of the three volume compensation chambers were left free to deform. The following subsections detail the sensor's design and experimental performance.

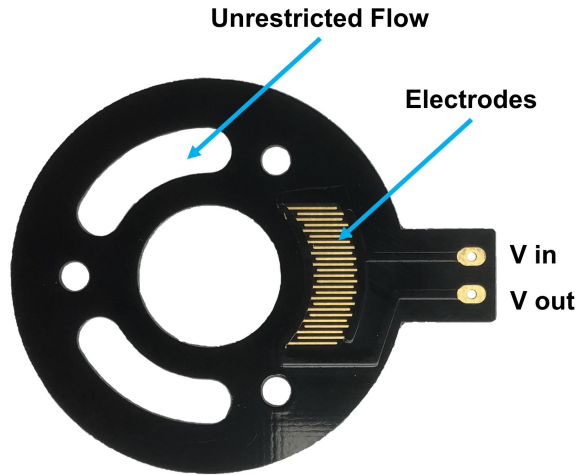
#### Design

The single point pressure (SPP) sensing PCB is shown in Figure 5.5. To improve upon the TPP sensor design, only one volume compensation chamber was used for pressure sensing, leaving the remaining two free to expand under pressure. Additionally, during assembly, a small plastic element was placed between the membrane and PSR film to pre-stress the film against the electrode with a goal of increasing sensitivity to small deformations.

#### Performance Evaluation

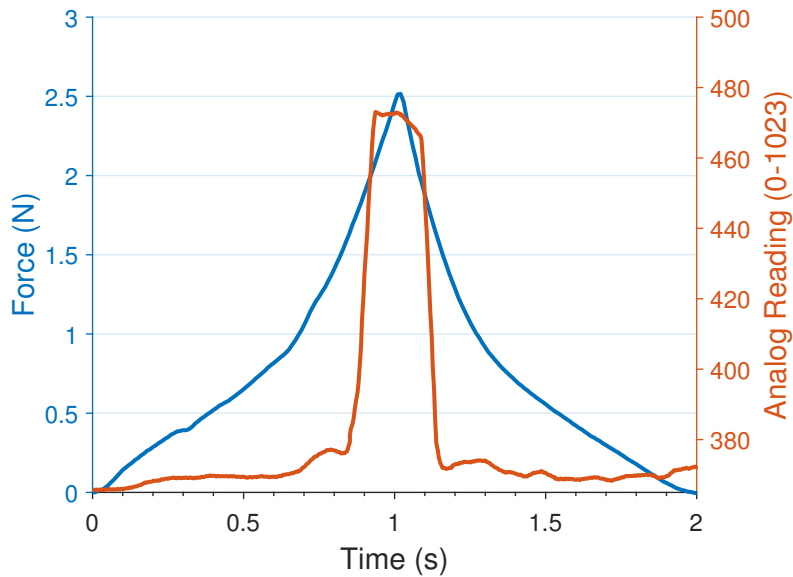
A squeeze-flow actuator was assembled with the SPP sensor and tested using a DMA. The contact surface was deformed 1 mm at 1 mm/s. The same data collection system described in the TPP sensor Performance Evaluation was used.

Figure 5.6 shows the combined response of the actuator and SPP sensor in the off-state. As shown, the sensor did not respond until about 0.7 s into the stroke, where its reading then increased with indentation up to 1 s and decreased back to the initial reading by 1.2 s. The actuator's force



**Figure 5.5.** Fabricated single point pressure sensor.

output was not saturated by the addition of the SPP sensor.



**Figure 5.6.** Off-state plot for the actuator and SPP sensor response under indentation.

## Discussion

Introducing the SPP sensor to the squeeze-flow actuator had mixed, but unsatisfactory results. The SPP design was successful in terms of not inhibiting the effect of voltage on actuator force output. However, it was incapable of sensing most of the indentation stroke. Ultimately, designing around monitoring the pressure at the volume compensation chambers proved too indirect. Though this sensing approach left the contact surface unobstructed, it may be necessary to use a more direct, fingertip level method of measuring displacement to achieve accuracy.

### 5.1.3 Bending Sensor

The third sensor tested was based on the bending of a strain sensitive resistive material placed over the device's contact membrane for direct measurement. The following subsections detail the sensor's design and experimental performance.

#### Design

The bending sensor design, shown in Figure 5.7, takes a more direct approach to measurement. The bending sensor consists of a similar material to the PSR film and has resistance sensitive to bending. The sensor is placed atop a squeeze-flow actuator and adhered to the cover using double-sided tape. The bending sensor reaches halfway across the membrane contact surface. The user directly presses on the bending sensor and membrane when interacting with the device. By measuring the change in voltage across the sensor, the indentation depth may be approximated in real time.

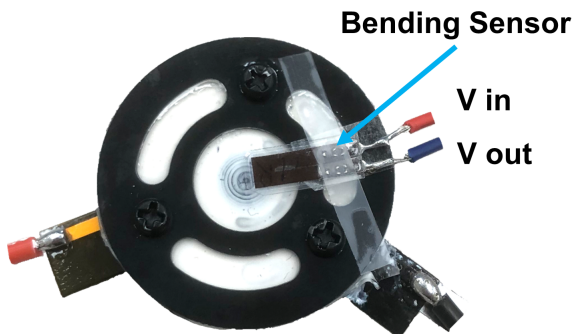


**Figure 5.7.** Assembled actuator with embedded bending sensor.

#### Performance Evaluation

A squeeze-flow actuator was assembled with the bending sensor, as shown in Figure 5.7, and tested using a DMA. The contact surface was deformed 1 mm at 1 mm/s for two cycles of loading/unloading to test for repeatability. The same data acquisition system described in the past two subsections was used.

The combined actuator and bending sensor response in the off-state is shown in Figure 5.8. As shown, the sensor successfully tracks the actuator's displacement. Initially ( $0 \rightarrow 0.1$  s), there is a transient effect observed in the sensor reading, but follows the actuator's displacement for the remainder of the trial. Introducing the bending sensor increases the force required to indent the contact surface due to its own stiffness.

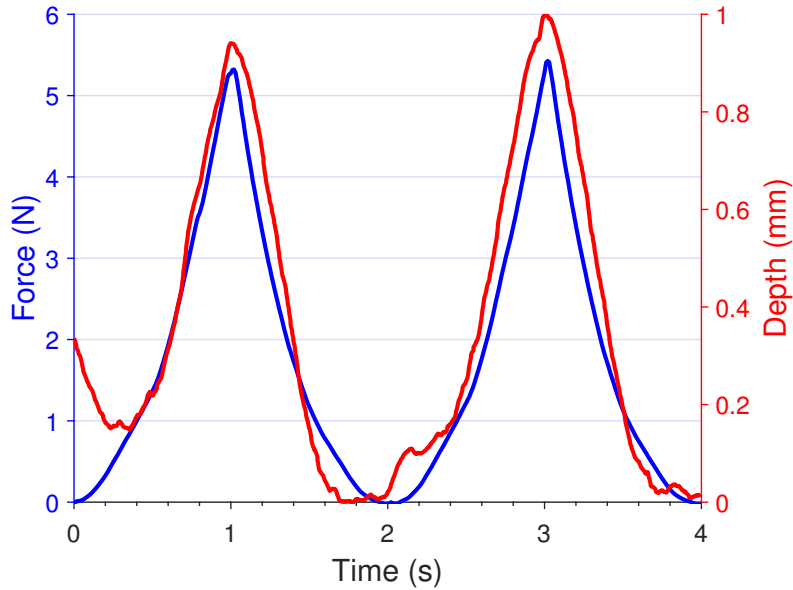


**Figure 5.8.** Off-state plot for the actuator and sensor response under indentation.

To determine the bending sensor's effectiveness when the actuator is active, a high-frequency, 4 kV square wave is supplied to the actuator during DMA testing. Figure 5.9 shows the combined actuator and sensor response. Under the applied electric field, the actuator's force output increases. The bending sensor tracks the indentation with more error than in the off-state trial, but is still effective.

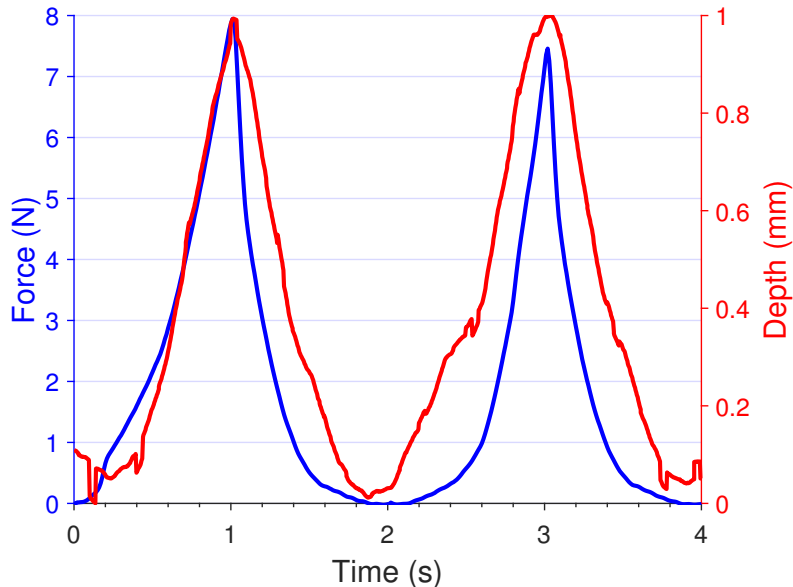


**Figure 5.9.** Actuator and bending sensor response under 4 kV 100 Hz square waves.

Similarly, the bending sensor's effectiveness was tested for when the actuator is subjected to lower, high amplitude frequencies. Figure 5.10 shows the combined actuator and sensor response

when 4 kV 3 Hz sine waves are supplied to the actuator. As shown, the actuator's force profile contains small oscillations. Because the experiment is strain-controlled (as opposed to stress-controlled), these oscillations are not present in the bending sensor reading profile. The bending sensor sufficiently tracks displacement under these voltage conditions.

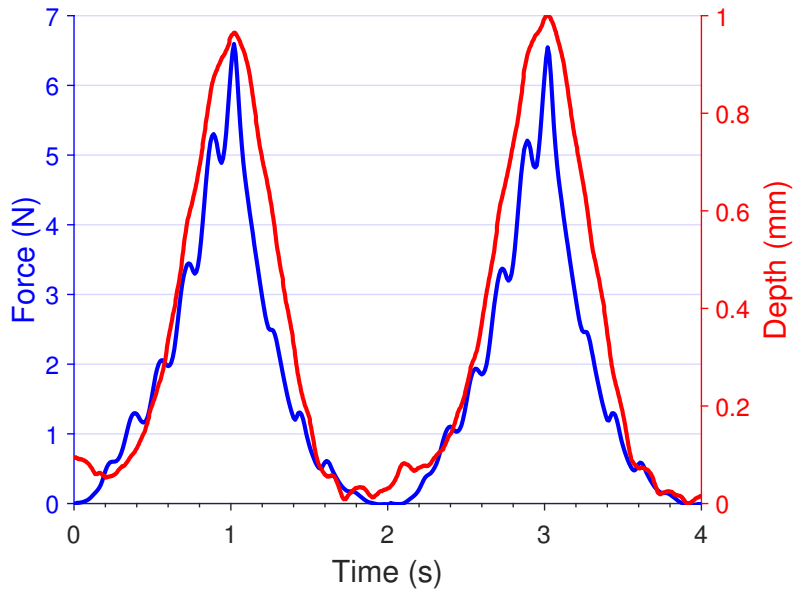


**Figure 5.10.** Actuator and bending sensor response under 4 kV 3 Hz sine waves.

## **Discussion**

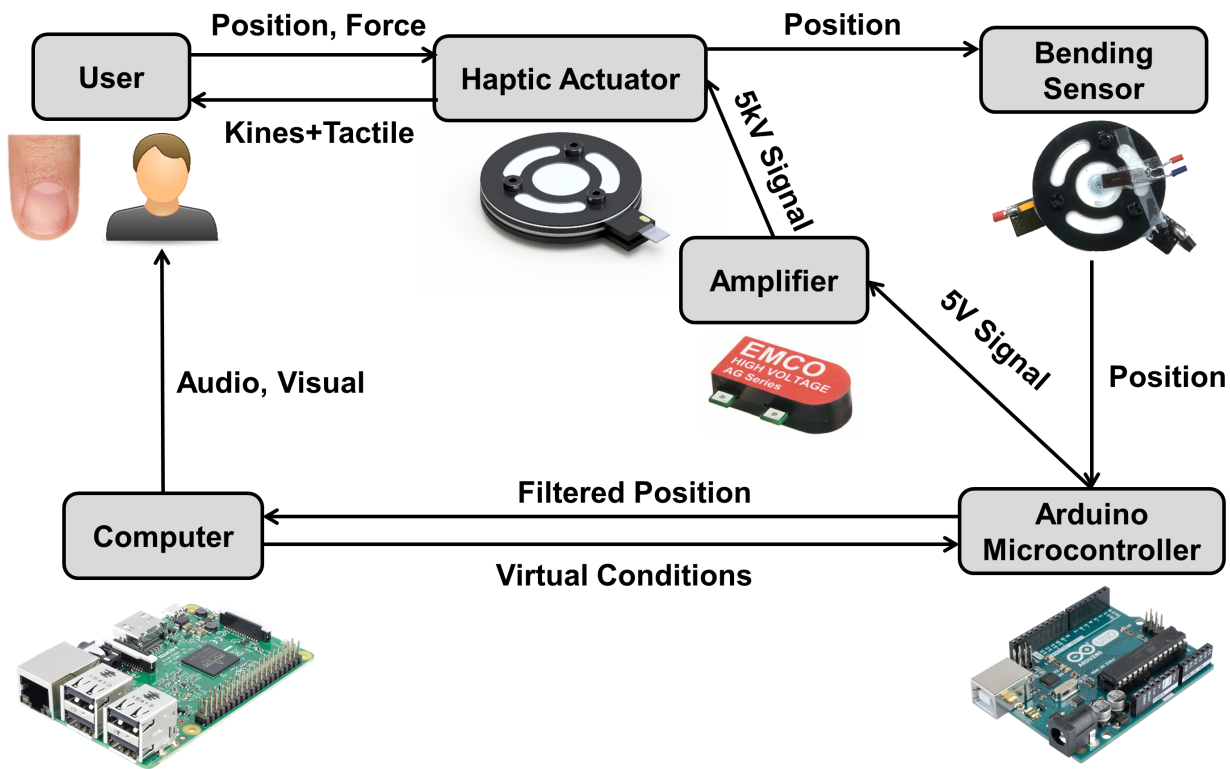
The bending sensor proved sufficient at tracking a finger's displacement when interacting with the actuator. It should be noted that adding the sensor to the contact membrane increases the force required to deform the membrane due to the sensor's stiffness. While the sensor is effective, it is not yet elegant. To best integrate the sensor into the actuator, a flexible PCB should be design and manufactured or the sensor may be directly fabricated within the contact membrane.

## **5.2 Control and Applications**

To demonstrate the haptic applications of the ERF-based haptic actuator, an infrastructure for coupling communication between the actuator and computer software should be developed. The following subsections detail the communication methods and software applications developed around the ERF-based haptic actuator.

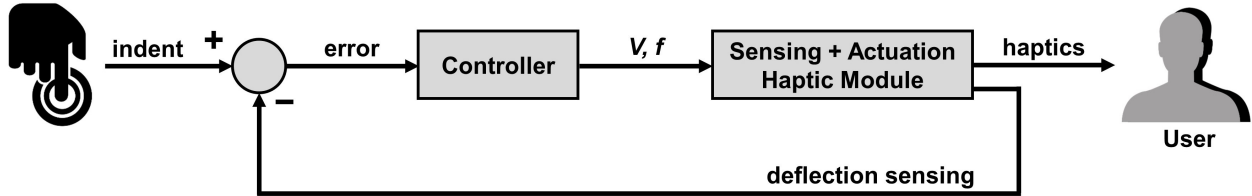
### 5.2.1 Information Loop and Hardware

Figure 5.11 shows the proposed sensorimotor loop. When a user presses upon the haptic actuator, the bending sensor conveys its position to an Arduino Uno microcontroller. The Arduino performs quick calculations, such as filtering the position data to remove any noise. The filtered position is fed into a computer (in this case, a Raspberry Pi for its compact form). The computer applies the position data to a virtual object model and calculates the appropriate actuator sensations to be supplied to the user. Signals corresponding to the desired forces are sent to the Arduino, which translates these signals into applied voltage and frequency. The Arduino's output is supplied to an amplifier module, discussed below in full, which steps the voltage up by a factor of 1000. The high voltage is then fed into the actuator's electrodes. The actuator translates the high voltage to kinesthetic and tactile sensations felt by the user and perceived as interaction with virtual objects. Additionally, the computer provides visual and audio feedback to the user.



**Figure 5.11.** Proposed flow of haptic interaction between user and computer.

The sensorimotor loop may be better visualized as a feedback control block diagram, shown in Figure 5.12. In this form, the actuator module serves as the plant, the computer and microcontroller collaborate as the controller and the bending sensor aids in calibrating feedback with respect to depth.



**Figure 5.12.** Proposed block diagram for haptic control.

For the actuator to be more portable and widely applicable, its laboratory electrical control (function generator and voltage amplifier) must be miniaturized and simplified. Figure 5.13 shows the circuit that was fabricated to replace the voltage amplifier. The circuit is centered around a proportional DC to HV DC converter (EMCO AG50). A 5 VDC signal is supplied to the converter, which transforms it up to 5000 V at the output. This HV output is delivered directly to the actuator's HV electrode. Two optocouplers (opto-isolators) are used to protect the other electrical components from the high voltages. The circuit is powered by 3-5 VDC.

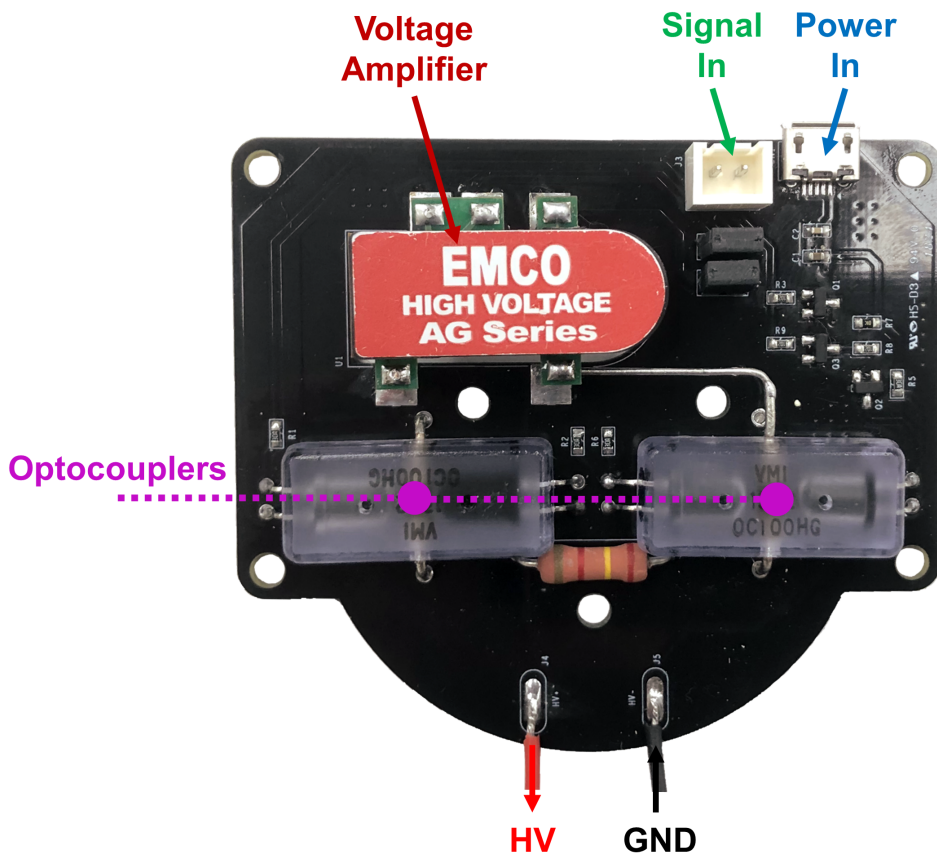


**Figure 5.13.** Fabricated circuit for controlling high voltage at compact scale.

The amplifier module features a very low profile compared to the benchtop amplifier. Additionally, the amplifier is easily controllable by an Arduino by dictating the signal input, eliminating

the need for a traditional function generator. However, it must be noted that the amplifier module is limited to producing 5 kV DC outputs, so the on-off frequency is the only variable available for differentiating sensations.

### 5.2.2 Design of Applications

To test the actuator's ability to convey digital information, prototype computer interfaces were developed to communicate with the actuator and sensor via the loop described in Figure 5.11. All visual development was done using Processing, an open-source graphical library that uses Java language. All embedded development was done in C++.

First, an interface was developed to emulate a function generator, as shown in Figure 5.14. The button (left) controls whether high voltage is supplied to the actuator. The slider (right) controls the frequency at which the HV DC signal is switched on and off in real-time. Additionally, the sensor's analog reading over time may be plotted within the same interface. This small program provided the infrastructure for two-way serial communication between the Arduino and computer, where the Arduino sends sensor readings to the computer and the computer sends on-off frequencies to the Arduino.

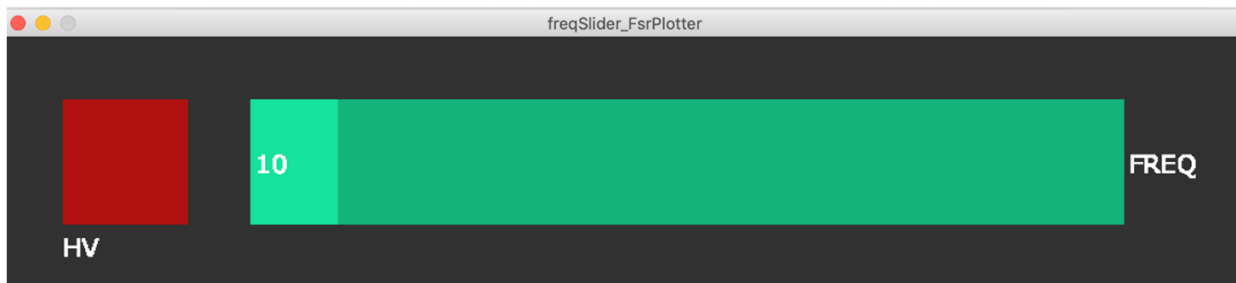


**Figure 5.14.** Function Generator App: Controls the frequency of 5 kV square waves in real-time.

Building upon the code developed in the Function Generator App, a second application was made to demonstrate the haptic interface's potential. As shown in Figure 5.15, the Frequency Mapping App consists of two visual components. On the right, an avatar of the ERF haptic button and a virtual finger can be seen. When the user indents the physical haptic button, the virtual finger moves downward in proportion with the sensor's reading. On the left, a plot of frequency with respect to the sensor reading is shown. The microcontroller firmware contains a set of pre-defined frequency-sensor reading maps. For instance, frequency may be mapped to the sensor reading in a proportional, inverse or piecewise relation. When the user presses upon the physical haptic button, the selected frequency profile with respect to sensor reading, or depth, is felt by the user and plotted in the app in real-time.

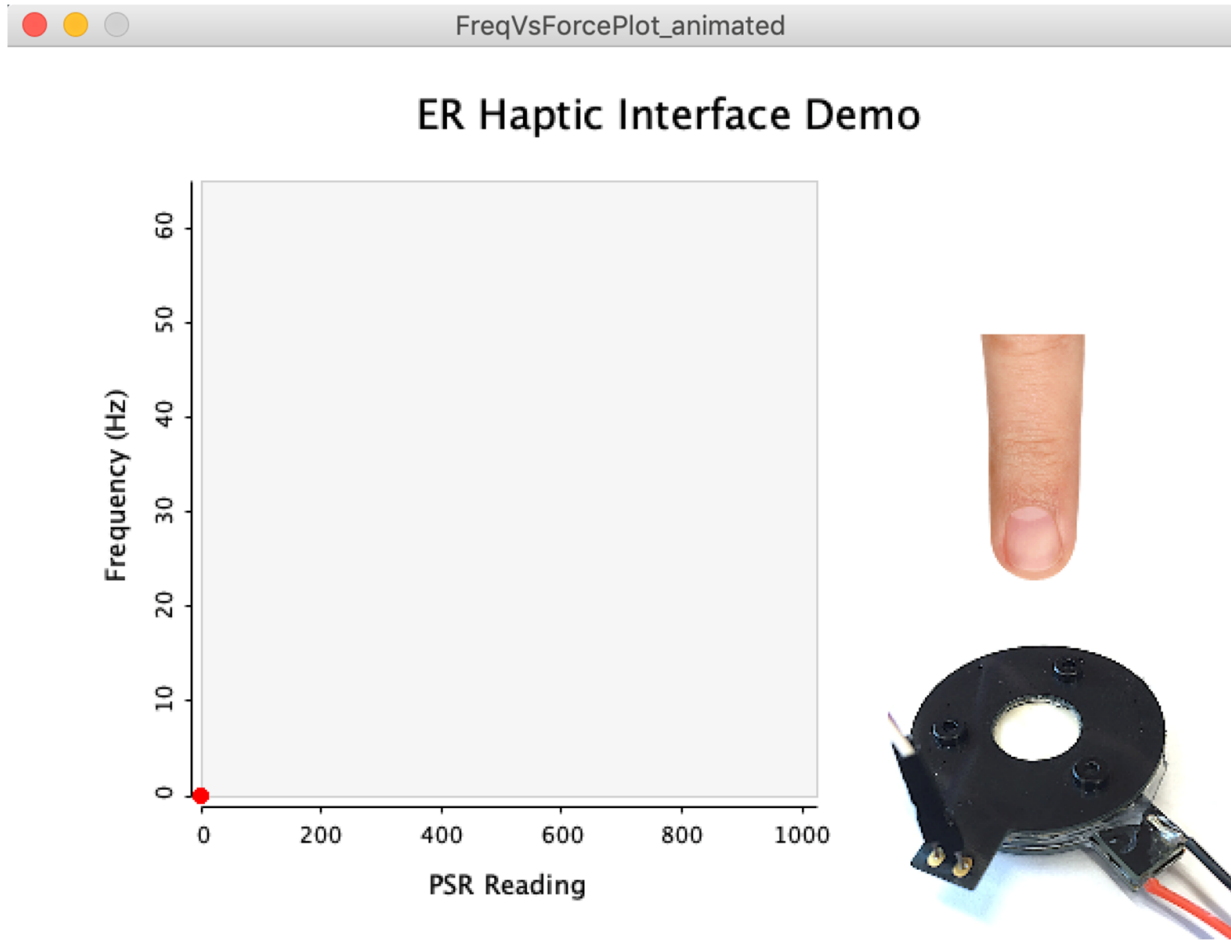


**Figure 5.15.** Frequency Mapping App: Plots displacement in real-time and maps the supplied frequency to the displacement.

## 5.3 Conceptual Designs

Having developed a robust haptic device based on ER fluids, as well as methods for two-way communication between the human operator, haptic device and computer, there exist a few promising natural extensions of the current work. First, methods are discussed for rendering compliant materials through the ER actuator's dynamic behavior. Then, suggestions are made toward a new, haptic array based on ERF for rendering over a continuous surface.

### 5.3.1 Haptic Rendering

To convey realistic information through touch, haptics researchers look to implement *haptic rendering* into their interfaces. *Rendering* refers to the practice of imposing specific sensations on the user to convey information about a virtual object. This information represents the virtual ob-

ject's physical properties, such as texture, elasticity, shape, mass, et cetera [87]. In this subsection, a brief literature survey on haptic rendering research is presented, followed by a description of implementing rendering into the prototype ERF haptic device.

## **A Brief Review of Haptic Rendering Techniques**

---

To understand the underlying algorithms behind haptic rendering, a typical haptic loop sequence is described [87]:

1. Position sensor readings are sampled and to approximate the position of the device-body interface.
2. A collision-detection algorithm reads in the approximated position and determines collisions between objects and avatars and outputs the resulting degree of penetration/indentation.
3. A force-response algorithm computes the interaction forces between avatars and virtual object found by collision-detection.
4. The force-response algorithm forwards the interaction forces to a control algorithm, which is responsible for imposing interaction forces on the operator in a stable manner.

Information on forces from the haptic loop is carried into the simulation loop, which then presents information to the graphics engine for visual feedback. This cycle is generally performed at about a 1 kHz rate for reasonably complex objects.

These basic principles have been applied to a wide range of haptic rendering systems for different purposes. Rendering of friction and texture across surfaces has been the subject of much study given the loss of feedback in smooth touch screen devices [88–93]. Other systems have been developed for rendering force and material feedbacks, though less focus has been devoted to this area [94].

## **Enabling Rendering of Compliant Objects**

---

Generally, haptic rendering may be subdivided into two categories: (1) model-driven haptic rendering and (2) data-driven haptic rendering. When applying model-driven haptic rendering, a model is used to process sensor inputs and compute actuator outputs based on the the model's physics. When implementing data-driven haptic rendering, physical data from real objects is recorded and used as the basis for determining the system's outputs from inputs. For instance, Kuchenbecker et al. collected one hundred different materials (wood, cloth, rubber, etc.) and used a tool to record position, orientation, force and high-frequency acceleration when dragged across the materials'

surfaces [89]. These texture samples were then post-processed into transfer functions for modeling texture. In recent years, data-driven haptic rendering has grown increasingly popular for its ability to accurately reproduce realistic sensations [90].

While most of the work in data-driven haptic rendering has focused on rendering of textures and friction, the rendering of data-driven force feedback (and combined kinesthetic and tactile feedback) has been less explored. This gap may be filled by the squeeze-flow haptic actuator for its wide range of stiffnesses and frequencies, as well as ease of controllability. In particular, the actuator may be used to render the click and release of a button, as demonstrated by Park et al. [95]. In this study, acceleration data was recorded during the press of a physical button. The data was processed through a fast Fourier transform to extract the principal frequencies associated with the button's press and release. These frequencies were then forwarded into a controlled actuator to emulate the sensation associated with the button's click. From this study, a generalizable process can be derived and applied to the squeeze-flow actuator:

1. Collect compliant objects with stiffnesses similar to the range produced by the squeeze-flow actuator (sponge, snow, foam, organs, etc.).
2. Use the DMA and accelerometer setup described in subsection 4.5.1 to record the force and acceleration data associated with indenting the object 1 mm.
3. Process the recorded data to find associated voltages and frequencies necessary to reproduce the profiles using the squeeze-flow ER haptic actuator.
4. Implement control to send the displacement-dependent voltage and frequency to the actuator in response to indentation.
5. Store the processed data as transfer functions in a lookup table for rendering a wide range of compliant materials based on virtual conditions.

### 5.3.2 ERF Haptic Display

Having produced a single degree of freedom proof of ER fluid as a basis for a miniature haptic button, it is logical to look to extend this concept into a larger, surface-type haptic display. While previous works have focused on ER fluid-based displays, most were developed long ago and many advances in ER fluid production have been made in the meantime, such as giant ER fluid and optically transparent ER fluid [62, 96]. Because of this, most early ERF displays focus strictly on low-force tactile applications [43, 45, 57, 97]. Similarly, advances in PCB manufacturing would allow for simpler and more compact design, as evidenced by this thesis. Perhaps the most compelling reason for revisiting ER fluid for touch displays lies in the advancements made in haptic

rendering and human-machine interfaces since the early 2000s. Jansen's MudPad established the building blocks for a more robust haptic display based on smart fluids and offers great value in the form of a research device for studying localized active haptic feedback for touch screens [34]. As flexible smart phone displays begin to enter the commercial market, ER fluid may pose a potential solution to introducing haptics through variable stiffness.

## 5.4 Conclusion and Discussion

This chapter has presented the design and implementation of applications for the ER fluid-based haptic actuator. First, sensors were designed and tested for their ability to accurately track the contact membrane's displacement. It was found that the bending sensor offered the best performance. Then, a sensorimotor loop was proposed for two-way communication between the user and a virtual environment through the actuator. A PCB was designed and fabricated to reduce the size of the lab's voltage amplifier. Two basic applications were developed to demonstrate this communication in action. Having established the framework for using the actuator as a haptic interface, future applications of haptic rendering and surface displays were described. In summary, the actuator may be used to convey meaningful stiffnesses and tactile sensations between a user and virtual environment.

# 6 | Conclusions and Future Work

In this final chapter, the work presented thus far is summarized and the principal contributions are highlighted. This thesis closes with remarks on the outlook for the field, with attention given to technical challenges and open questions.

## 6.1 Summary

This thesis has presented a novel miniature haptic actuator that utilizes electrorheological fluids to generate both kinesthetic and vibrotactile sensations. First, a pure flow mode actuator was designed and fabricated from printed circuit boards, resulting in a compact form factor (6 mm thickness). Despite its small overall size, the actuator's stroke is sufficiently large (1 mm) to represent multiple steps of haptic feedback during interaction. An accompanying analytical model for the actuator's behavior was derived and implemented into a computational model. The fabricated actuator was tested for its ability to convey kinesthetic and vibrotactile sensations using a dynamic mechanical analyzer. The experimental results indicate that the actuator's force output increases with the applied voltage. In the off-state, the actuator produced 2.5 N at maximum depth, whereas with 4 kV applied, the maximum force was found to be 3.6 N. As discussed, the just-noticeable-difference for the force that a human can reliably discriminate is about 7~10% for forces ranging from 0.5~200 N. JND analysis was performed on the experimental results and indicated that the flow mode actuator could produce distinct kinesthetic sensations for 2, 3 and 4 kV load. Additionally, introducing a frequency to the applied voltage produced distinct tactile sensations, validating that the flow mode design produces comprehensive haptic feedback. Furthermore, the computational model showed agreement with the experimental results and was used for performing parametric studies (Chapter 3).

Following the successful demonstration of the flow mode ER haptic actuator, a squeeze mode was implemented into the design by fabricating a deformable electrode, resulting in a combined squeeze-flow ER haptic actuator. Despite adding another ER fluid mode, the device measured only 6.5 mm thick and promised to produce a wider range of forces. Again, a corresponding mathematical model was developed based on combined squeeze-flow behavior. The fabricated actuator was again tested using DMA. At maximum depth, the actuator generated 2.7 N in its off-state and 6.2 N under 4 kV load, a 130% increase. Furthermore, the JND results supported the device's ability to convey distinct kinesthetic feedback at high voltages. Vibrotactile testing was performed for both low and high frequencies, where the low frequency testing examined the harmonic force output and the high frequency testing evaluated the device's acceleration generation. Both indicated

that the actuator produced specific and controllable vibrotactile responses. Compared to the pure flow mode design, the squeeze-flow mode actuator offered a wider range of output forces, greater stability and larger amplitudes of vibration. Finally, the computational model supported the results produced experimentally (Chapter 4).

Having established the basis for slim haptic actuators based on ER fluids, applications for these actuators was explored. First, sensing techniques were designed, tested and iterated upon. It was experimentally determined that the sensor must be placed within the contact region of the membrane to best sense displacement. A bending sensor was used as a working prototype with recommendations made toward the development of a flexible sensing PCB. The actuator and sensor were incorporated into a human-machine sensorimotor loop for two-way communication between a user and virtual environment. To this end, a miniature voltage amplifier was designed to be easily controlled by an Arduino microcontroller, eliminating the need for a large function generator. Using this infrastructure, two applications were developed. First, a virtual function generator was produced to control the actuator's behavior through the newly-fabricated amplifier. The second application built upon the first's codebase and provided an interface for visualizing the signals produced by the actuator, as well as the sensor's real-time position. Finally, recommendations were made toward the design of future applications, such as haptic rendering of compliant materials and an ER fluid-based haptic display (Chapter 5).

In summary, this research demonstrates the potential for miniature actuators for conveying both kinesthetic and tactile feedback.

## 6.2 Contributions

The contributions of this research are summarized as follows:

- **Chapter 3:** A new type of miniature actuator based on ER fluid in flow mode for combined kinesthetic and vibrotactile feedback at mobile scale was proposed and fabricated. Mechanical testing indicated that the device could produce a range of kinesthetic and tactile feedbacks. Mathematical modeling of the flow mode actuator was performed in parallel with the design and validated through experiments. This model can be applied to design optimization for miniaturization and force output.
- **Chapter 4:** A novel squeeze-flow ER haptic actuator was developed to increase the produced force range. The design modification yielded a greater electrode area while maintaining a compact form factor. In mechanical testing, the squeeze-flow device was found capable of generating a wider range of output forces, great stability and large amplitudes of vibration.
- **Chapter 5:** A framework for incorporating the actuator into a meaningful haptic interface

was developed. Sensor performances were characterized and iterated upon. A codebase and example applications were developed for the control and demonstration of the system.

## **6.3 Future Outlooks**

The ideas and results presented in this thesis lay the groundwork for methods of producing small haptic actuators based on ER fluids. This section discusses a few directions that may be addressed moving forward.

### **6.3.1 Miniaturization, Simplification and Optimization**

In its current state, the actuator's design features certain weaknesses that should be mitigated for future study. While the membrane design offers a satisfying compliant surface, it does suffer from the transient viscoelastic effects of creep and stress relaxation over extended use. For a more durable design, one may use the membrane only as volume compensation. Having found squeeze mode to be especially effective, it may be possible to design a piston mechanism using the electrode spring as a contact surface. Similarly, the device's circumference may be reduced by removing the flow mode region, at little cost to the squeeze-dominant output force. To design around the squeeze-mode basis, mathematical modeling may be used for performance optimization. This would open up the design to a greater range of miniature applications.

### **6.3.2 Haptic Rendering**

The actuator's ability to generate a wide range of stiffnesses and frequencies with little delay makes it a great candidate for the rendering of compliant objects. Future work may use the data-driven technique described in Subsection 5.3.1 to implement the actuator into a meaningful haptic interface.

### **6.3.3 Haptic Display**

This thesis developed a single degree of freedom actuator based on ER fluids. To offer a more robust interface, a surface with localized haptic feedback may be designed around the working principles presented here by implementing an array of electrodes. The display would be especially thin due to its ERF basis while providing both tactile and kinesthetic sensations.

# References

- [1] Srinivasan, M. A., and Basdogan, C., 1997. “Haptics in virtual environments: Taxonomy, research status, and challenges”. *Computers & Graphics*, **21**(4), pp. 393–404.
- [2] Adams, R. J., Moreyra, M. R., and Hannaford, B., 1998. “Stability and Performance of Haptic Displays : Theory and Experiments”. In Proceedings ASME International Mechanical Engineering Congress and Exhibition, pp. 227–234.
- [3] An, J., and Kwon, D. S., 2006. “Stability and performance of haptic interfaces with active/pассив actuators - Theory and experiments”. *International Journal of Robotics Research*, **25**(11), pp. 1121–1136.
- [4] Bianchi, M., Scilingo, E. P., Serio, A., and Bicchi, A., 2009. “A new softness display based on bi-elastic fabric”. In Proc. Eurohaptics’09, pp. 382–383.
- [5] Fujita, K., and Ohmori, H., 2000. “A new softness display interface by dynamic fingertip contact area control”. *Proceedings of the 5th World Multiconference on Systemics, Cybernetics and Informatics*, pp. 78–82.
- [6] Song, A., Morris, D., and Colgate, J. E., 2005. “Haptic telemanipulation of soft environment without direct force feedback”. In IEEE International Conference on Information Acquisition, pp. 21–25.
- [7] Raptis, D., Tselios, N., Kjeldskov, J., and Skov, M. B., 2013. “Does size matter? Investigating the impact of mobile phone screen size on users’ perceived, effectiveness and efficiency”. In Proc. MobileHCI ’13, pp. 127–136.
- [8] Coles, T. R., Meglan, D., and John, N. W., 2011. “The role of haptics in medical training simulators: A survey of the state of the art”. *IEEE Transactions on Haptics*, **4**(1), pp. 51–66.
- [9] Laycock, S. D., & Day, A. M., 2003. “Recent developments and applications of haptic devices.”. In *Computer Graphics Forum*, **22, No 2**(2), pp. 117–132.
- [10] Park, J., and Khatib, O., 2006. “A haptic teleoperation approach based on contact force control”. *International Journal of Robotics Research*, **25**(5-6), pp. 575–591.
- [11] Mazursky, A. J., Koo, J.-H., and Yang, T.-H., 2018. “Experimental evaluation of a miniature haptic actuator based on electrorheological fluids”. In SPIE Smart Structures and Nondestructive Evaluation, Vol. 12, SPIE.

## REFERENCES

---

- [12] Lederman, S., and Klaztky, R., 2009. “Haptic perception: A tutorial”. *Attention, Perception, & Psychophysics*, **71**(7), pp. 1439–1459.
- [13] Culbertson, H., Schorr, S. B., and Okamura, A. M., 2018. “Haptics: The Present and Future of Artificial Touch Sensations”. *Annual Review of Control, Robotics, and Autonomous Systems*, **1**, pp. 385–409.
- [14] Blausen.com, 2014. “Medical gallery of Blausen Medical 2014”. *WikiJournal of Medicine*, **1**(2), p. 49.
- [15] Chouvardas, V. G., Miliou, A. N., and Hatalis, M. K., 2008. “Tactile displays: Overview and recent advances”. *Displays*, **29**(3), pp. 185–194.
- [16] Johansson, R. S., and Flanagan, J. R., 2009. “Coding and use of tactile signals from the fingertips in object manipulation tasks”. *Nature Reviews Neuroscience*, **10**(5), pp. 345–359.
- [17] Johnson, K. O., 2001. “The roles and functions of cutaneous mechanoreceptors”. *Current Opinion in Neurobiology*, **11**(4), pp. 455–461.
- [18] Geldard, F. A., 1960. “Some neglected possibilities of communication”. *Science*, **131**(3413), pp. 1583–1588.
- [19] Bolanowski, S. J., Gescheider, G. A., and Verrillo, R. T., 1994. “Hairy Skin: Psychophysical Channels and Their Physiological Substrates”. *Somatosensory and Motor Research*, **11**(3), pp. 279–290.
- [20] Bell, J., Bolanowski, S. J., and Holmes, M. H., 1994. “The structure and function of pacinian corpuscles: a review”. *Progress in Neurobiology*, **42**, pp. 79–128.
- [21] Hulliger, M., 1984. *The mammalian muscle spindle and its central control*. Springer Berlin Heidelberg, Berlin, Heidelberg, pp. 1–110.
- [22] Moore, J. C., 1984. “The Golgi Tendon Organ: A Review and Update”. *The American Journal of Occupational Therapy*, **38**(4), pp. 227–236.
- [23] Pang, X. D., Tan, H. Z., and Durlach, N. I., 1991. “Manual discrimination of force using active finger motion”. *Perception & Psychophysics*, **49**(6), pp. 531–540.
- [24] Hoggan, E., Brewster, S. A., and Johnston, J., 2008. “Investigating the Effectiveness of Tactile Feedback for Mobile Touchscreens”. In Proc. CHI’08, pp. 1573–1582.
- [25] Poupyrev, I., Maruyama, S., and Rekimoto, J., 2002. “Ambient touch: designing tactile interfaces for handheld devices”. In Proc. UIST’02, Vol. 4, pp. 51–60.

## REFERENCES

---

- [26] Gupta, S., and Campbell, T., 2010. “Squeezeblock: Using virtual springs in mobile devices for eyes-free interaction”. In Proc. UIST’10, pp. 101–104.
- [27] Fukumoto, M., and Sugimura, T., 2001. “Active click: tactile feedback for touch panels”. In Proc. CHI’01, p. 121.
- [28] Poupyrev, I., and Maruyama, S., 2003. “Tactile Interfaces for Small Touch Screens”. In Proc. UIST’03, Vol. 5, pp. 217–220.
- [29] Rekimoto, J., and Schweißig, C., 2006. “PreSenseII: Bi-directional Touch and Pressure Sensing Interactions with Tactile Feedback”. In Proc. CHI’06, pp. 1253–1258.
- [30] Nakagawa, Y., Kamimura, A., and Kawaguchi, Y., 2012. “MimicTile: A Variable Stiffness Deformable User Interface for Mobile Devices”. In Proc. CHI’12, p. 745.
- [31] White, T., 1998. “Introducing Liquid Haptics in High Bandwidth Human Computer Interfaces”. PhD thesis, Massachusetts Institute of Technology.
- [32] Jansen, Y., Karrer, T., and Borchers, J., 2010. “MudPad: localized tactile feedback on touch surfaces”. In Proc. UIST’10, pp. 385–386.
- [33] Jansen, Y., Karrer, T., and Borchers, J., 2010. “MudPad: Tactile Feedback and Haptic Texture Overlay for Touch Surfaces”. In Proc. of ACM Int. Conf. on ITS, pp. 11–14.
- [34] Jansen, Y., 2011. “MudPad: Localized Tactile Feedback on Multi Touch Surfaces”. PhD thesis, RWTH Aachen University.
- [35] Han, Y.-M., Oh, J.-S., Kim, J.-K., and Choi, S.-B., 2014. “Design and experimental evaluation of a tactile display featuring magnetorheological fluids”. *Smart Materials and Structures*, **23**(7), pp. 1–11.
- [36] Yang, T. H., Kwon, H. J., Lee, S. S., An, J., Koo, J. H., Kim, S. Y., and Kwon, D. S., 2010. “Development of a miniature tunable stiffness display using MR fluids for haptic application”. *Sensors and Actuators A: Physical*, **163**(1), pp. 180–190.
- [37] Yang, T. H., Koo, J. H., Kim, S. Y., and Kwon, D. S., 2017. “Modeling and test of a kinaesthetic actuator based on MR fluid for haptic applications”. *Review of Scientific Instruments*, **88**(3).
- [38] Whittle, M., and Bullough, W. A., 1992. “The structure of smart fluids”. *Nature*, **358**, p. 373.
- [39] Whittle, M., Atkin, R., and Bullough, W. A., 1996. “Dynamics of an Electrorheological Valve”. *International Journal of Modern Physics B*, **10**(23, 24), pp. 2933–2950.

## REFERENCES

---

- [40] Bullough, W. A., Johnson, A., Hosseini-Sianaki, A., Makin, J., and Firoozian, R., 1993. “The electro-rheological clutch: design, performance characteristics and operation”. *Proceedings of the Institution of Mechanical Engineers, Part I: Journal of Systems and Control Engineering*, **207**(2), pp. 87–95.
- [41] Han, S. S., Choi, S. B., and Cheong, C. C., 2000. “Position control of X-Y table mechanism using electro-rheological clutches”. *Mechanism and Machine Theory*, **35**(11), pp. 1563–1577.
- [42] Fricke, J., 1993. Tactile Graphic Computer Screen and Input Tablet For Blind Persons Using an Electrorheological Fluid.
- [43] Monkman, G., 1992. “An Electrorheological Tactile Display”. *Presence: Teleoperators and Virtual Environments*, **1**(2), pp. 219–228.
- [44] Pfeiffer, C., Mavroidis, C., Bar-Cohen, Y., and Dolgin, B., 1999. “Electrorheological Fluid Based Force Feedback Device”. In Proceedings of the 1999 SPIE Telemanipulator and Telepresence Technologies VI, Vol. 3840, pp. 88–99.
- [45] Taylor, P. M., Hosseini-Sianaki, A., and Varley, C. J., 1996. “An electrorheological fluid-based tactile array for virtual environments”. In Proceedings of 1996 IEEE International Conference on Robotics and Automation, Vol. 1, pp. 18–23.
- [46] Goto, M., and Takemura, K., 2013. “Tactile bump display using electro-rheological fluid”. In IEEE International Conference on Intelligent Robots and Systems, pp. 4478–4483.
- [47] Tsujita, T., Kobayashi, M., and Nakano, M., 2010. “Design and development of a braille display using micro actuators driven by ER suspension”. *International Journal of Applied Electromagnetics and Mechanics*, **33**(3-4), pp. 1661–1669.
- [48] Mazursky, A., Koo, J.-H., and Yang, T.-H., 2018. “Application of Electro-Rheological Fluids for Conveying Realistic Haptic Feedback”. In Int. Conference on Adaptive Structures and Technologies, pp. 2–13.
- [49] Winslow, W., 1949. “Induced Fibrillation of Suspensions”. *Journal of Applied Physics*, **20**.
- [50] Block, H., and Kelly, J., 1988. “Electro-rheology”. *J. Phys. D: Appl. Phys.*, **21**, p. 1661.
- [51] Gast, A. P., and Zukoski, C. F., 1989. “Electrorheological Fluids as Colloidal Suspensions”. *Advances in Colloid and Interface Science*, **30**, pp. 153–202.

## REFERENCES

---

- [52] Bose, H., and Trendles, A., 2003. “Smart Fluids – Properties and Benefit for New Electromechanical Devices”. In AMAS Workshop on Smart Materials and Structures SMART’03, pp. 329–336.
- [53] Stanway, R., Sproston, J., and El-Wahed, A. K., 1996. “Application of electrorheological fluids in vibration control”. *Smart Materials and Structures*, **5**(4), pp. 464–482.
- [54] Kamelreiter, M., Kemmetmüller, W., and Kugi, A., 2012. “Digitally controlled electrorheological valves and their application in vehicle dampers”. *Mechatronics*, **22**(5), pp. 629–638.
- [55] Nakamura, T., Saga, N., and Nakazawa, M., 2004. “Variable viscous control of a homogeneous ER fluid device considering its dynamic characteristics”. *Mechatronics*, **14**(1), pp. 55–68.
- [56] Han, Y. M., and Choi, S. B., 2006. “Force-feedback control of a spherical haptic device featuring an electrorheological fluid”. *Smart Materials and Structures*, **15**(5), pp. 1438–1446.
- [57] Böse, H., Baumann, M., Monkman, G., Egersdörfer, S., Tunayar, A., Freimuth, H., Ermert, H., and Khaled, W., 2005. “A New ER Fluid Based Haptic Actuator System For Virtual Reality”. *International Journal of Modern Physics B*, **19**(7, 8, 9), pp. 1628–1634.
- [58] Hong, S. R., Choi, S. B., Jung, W. J., and Jeong, W. B., 2002. “Vibration isolation of structural systems using squeeze mode ER mounts”. *Journal of Intelligent Material Systems and Structures*, **13**(7-8), pp. 421–424.
- [59] Williams, E. W., Rigby, S. G., Sproston, J. L., and Stanway, R., 1993. “Electrorheological fluids applied to an automotive engine mount”. *Journal of Non-Newtonian Fluid Mechanics*, **47**, pp. 221–238.
- [60] Choi, S.-B., and Hong, S.-R., 2004. “Dynamic Modeling and Vibration Control of Electrorheological Mounts”. *Journal of Vibration and Acoustics*, **126**(4), p. 537.
- [61] Carlson, J. D., and Jolly, M., 2000. “MR Fluid, foam and elastomer devices”. *Mechatronics*, **10**(4-5), pp. 555–569.
- [62] Wen, W., Huang, X., Yang, S., Lu, K., and Sheng, P., 2003. “The giant electrorheological effect in suspensions of nanoparticles”. *Nature Materials*, **2**(11), nov, pp. 727–730.
- [63] Ma, H., Wen, W., Tam, W. Y., and Sheng, P., 1996. “Frequency Dependent Electrorheological Properties: Origin and Bounds”. *Physical Review Letters*, **77**(12), pp. 2499–2502.

## REFERENCES

---

- [64] Ma, H., Wen, W., Tam, W. Y., and Sheng, P., 2003. “Dielectric electrorheological fluids: Theory and experiment”. *Advances in Physics*, **52**(4), pp. 343–383.
- [65] Goldasz, J., and Sapinski, B., 2012. “Nondimensional characterization of flow-mode magnetorheological/ electrorheological fluid dampers”. *Journal of Intelligent Material Systems and Structures*, **23**(14), pp. 1545–1562.
- [66] Phillips, R., 1969. “Engineering applications of fluids with a variable yield stress”. PhD thesis, University of California, Berkeley.
- [67] Dimock, G. A., Yoo, J. H., and Wereley, N. M., 2002. “Quasi-steady Bingham biplastic analysis of electrorheological and magnetorheological dampers”. *Journal of Intelligent Material Systems and Structures*, **13**(9), pp. 549–559.
- [68] Wang, X., and Gordaninejad, F., 1999. “Flow Analysis of Field-Controllable, Electro- and Magneto-Rheological Fluids Using Herschel-Bulkley Model”. *Journal of Intelligent Material Systems and Structures*, **10**, pp. 601–608.
- [69] Wereley, N., 2003. “Nondimensional analysis of electrorheological and magnetorheological dampers using a Herschel-Bulkley constitutive model”. In Proceedings of the ASME/JSME Joint Fluids Engineering Conference, pp. 1587–1594.
- [70] Hong, S. R., John, S., Wereley, N. M., Choi, Y. T., and Choi, S. B., 2008. “A unifying perspective on the quasi-steady analysis of magnetorheological dampers”. *Journal of Intelligent Material Systems and Structures*, **19**(8), pp. 959–976.
- [71] Chang, C.-C., and Roschke, P., 1998. “Neural Network Modeling of a Magnetorheological Damper”. *Journal of Intelligent Material Systems and Structures*, **9**, pp. 755–764.
- [72] Wang, D. H., and Liao, W. H., 2005. “Modeling and control of magnetorheological fluid dampers using neural networks”. *Smart Materials and Structures*, **14**(1), pp. 111–126.
- [73] Choi, H. J., Kim, J. W., Cho, M. S., Kim, C. A., and Jhon, M. S., 2001. “Characteristics of a Yield Stress Scaling Function for Electrorheological Fluids”. *Applied Physics Letters*, **78**(24), pp. 3806–3808.
- [74] Vemuri, S. H., Jhon, M. S., Zhang, K., and Choi, H. J., 2012. “New analysis of yield stress on giant electrorheological fluids”. *Colloid and Polymer Science*, **290**(2), pp. 189–192.
- [75] Zhang, K., Liu, Y. D., Jhon, M. S., and Choi, H. J., 2013. “Generalized yield stress equation for electrorheological fluids”. *Journal of Colloid and Interface Science*, **409**, pp. 259–263.

## REFERENCES

---

- [76] Mazursky, A., Koo, J.-H., and Yang, T.-H., 2019. “Design, modeling, and evaluation of a slim haptic actuator based on electrorheological fluid”. *Journal of Intelligent Material Systems and Structures*, pp. 1–13.
- [77] Ryu, S., Yang, T. H., Kim, S. Y., Koo, J. H., Kyung, K. U., Kwon, D. S., and Structure, A. O., 2012. “Design of a New Miniature Haptic Button Based on Magneto-Rheological Fluids”. In IEEE International Conference on Automation Science and Engineering, pp. 1–4.
- [78] Xu, L., Li, Y., Han, L., Shen, R., and Lu, K., 2018. “A test of giant electrorheological valve in DC and square wave AC fields with different frequencies”. *Journal of Intelligent Material Systems and Structures*, **29**(2), pp. 250–254.
- [79] Wereley, N. M., and Pang, L., 1998. “Nondimensional analysis of semi-active electrorheological and magnetorheological dampers using approximate parallel plate models”. *Smart Materials and Structures*, **7**, pp. 732–743.
- [80] Vlassak, J., and Nix, W., 1992. “A new bulge test technique for the determination of young’s modulus and poission’s ratio of thin films”. *Journal of Materials Research*, **7**(12), pp. 3249–3342.
- [81] Komaragiri, U., Begley, M. R., and Simmonds, J. G., 2005. “The Mechanical Response of Freestanding Circular Elastic Films Under Point and Pressure Loads”. *Journal of Applied Mechanics*, **72**(2), pp. 203–212.
- [82] Kamath, G. M., Hurt, M. K., and Wereley, N. M., 1996. “Analysis and testing of Bingham plastic behavior in semi-active electrorheological fluid dampers”. *Smart Materials and Structures*, **5**(5), pp. 576–590.
- [83] Farjoud, A., Cavey, R., Ahmadian, M., and Craft, M., 2009. “Magneto-rheological fluid behavior in squeeze mode”. *Smart Materials and Structures*, **18**(9), pp. 1–7.
- [84] Jolly, M., and Carlson, J., 1996. “Controllable squeeze film damping using magnetorheological fluid”. In Proceedings of the 5th international conference on new actuators, pp. 333–336.
- [85] Ryu, J., Jung, J., Park, G., and Choi, S., 2010. “Psychophysical model for vibrotactile rendering in mobile devices”. *Presence: Teleoperators and Virtual Environments*, **19**(4), pp. 364–387.
- [86] Ryu, S., Koo, J. H., Yang, T. H., Pyo, D., Kyung, K. U., and Kwon, D. S., 2015. “Design, simulation, and testing of a magnetorheological fluid-based haptic actuator for mobile applications”. *Journal of Intelligent Material Systems and Structures*, **26**(13), pp. 1670–1678.

## REFERENCES

---

- [87] Salisbury, K., Conti, F., and Barbagli, F., 2004. “Haptic rendering: Introductory concepts”. *IEEE Computer Graphics and Applications*, **24**(2), pp. 24–32.
- [88] Pyo, D., Ryu, S., Kim, S.-C., and Kwon, D.-S., 2014. “A new surface display for 3d haptic rendering”. In Haptics: Neuroscience, Devices, Modeling, and Applications, M. Auvray and C. Duriez, eds., Springer Berlin Heidelberg, pp. 487–495.
- [89] Culbertson, H., López Delgado, J. J., and Kuchenbecker, K. J., 2014. “One hundred data-driven haptic texture models and open-source methods for rendering on 3D objects”. In IEEE Haptics Symposium, pp. 319–325.
- [90] Romano, J. M., and Kuchenbecker, K. J., 2012. “Creating realistic virtual textures from contact acceleration data”. *IEEE Transactions on Haptics*, **5**(2), pp. 109–119.
- [91] Mullenbach, J., Shultz, C., Piper, A. M., Peshkin, M., and Colgate, J. E., 2013. “Surface haptic interactions with a TPad tablet”. In Proc. UIST’13, pp. 7–8.
- [92] Bau, O., Poupyrev, I., Israr, A., and Harrison, C., 2010. “TeslaTouch: Electrovibration for Touch Surfaces”. In Proc. UIST’10, pp. 1–10.
- [93] Ochiai, Y., Hoshi, T., Rekimoto, J., and Takasaki, M., 2014. “Diminished haptics: Towards digital transformation of real world textures”. In Haptics: Neuroscience, Devices, Modeling, and Applications, M. Auvray and C. Duriez, eds., Springer Berlin Heidelberg, pp. 409–417.
- [94] Nakagaki, K., Vink, L., Counts, J., Windham, D., Leithinger, D., Follmer, S., and Ishii, H., 2016. “Materiable: Rendering Dynamic Material Properties in Response to Direct Physical Touch with Shape Changing Interfaces”. In Proc. CHI’16, pp. 2764–2772.
- [95] Park, G., Choi, S., Hwang, K., Kim, S., Sa, J., and Joung, M., 2011. “Tactile effect design and evaluation for virtual buttons on a mobile device touchscreen”. In Proc. MobileHCI ’11, p. 11.
- [96] Liu, Y. D., Lee, B. M., Park, T.-S., Kim, J. E., Choi, H. J., and Booh, S. W., 2013. “Optically transparent electrorheological fluid with urea-modified silica nanoparticles and its haptic display application”. *Journal of Colloid and Interface Science*, **404**, pp. 56 – 61.
- [97] Taylor, P., Pollet, D., Hosseini-Sianaki, A., and Varley, C., 1998. “Advances in an electrorheological fluid based tactile array”. *Displays*, **18**(3), pp. 135–141.